Aus dem Max-Planck-Institut für Hirnforschung

in Frankfurt am Main

Gamma synchronization and spike timing

Vom Fachbereich Biologie der

Technischen Universität Darmstadt

zur Erlangung des akademischen Grades

eines Doctor rerum naturalium

genehmigte Dissertation von

M. Sc. Weijia Feng

aus Yangquan, China

1. Referent: Prof. Dr. Ralf A. W. Galuske

2. Referent: Prof. Dr. Bodo Laube

Tag der Einreichung: 08.03.2013

Tag der mündlichen Prüfung: 24.04. 2013

Darmstadt 2013

D 17

Zusammenfassung

Neuronale Synchronizität ist ein äußerst interessantes Phänomen des Gehirns und wird nun bereits seit Jahrzehnten untersucht. Mit dieser Arbeit habe ich weiter zur Untersuchung der Funktion von neuronaler Synchronizität beigetragen, wobei zwei Ansätze verwendet wurden: Die Analyse von Abfolgen von Spikes, die im primären visuellen Kortex von Katzen aufgezeichnet wurden sowie die theoretische Analyse von simulierten Spikesequenzen.

In der ersten Untersuchung habe ich Autokorrelationen der Spikesequenzen untersucht, die als Antwort auf die Applikation von bewegten Gitterreizen (moving gratings) entstanden. Autokorrelationen können als Statistik zweiter Ordnung von Spikezeiten gesehen werden. Die Mehrheit der beobachteten Autokorrelationen waren oszillatorischer Natur. Die mittleren Frequenzen bewegten sich im Beta und Gammabandbereich (ca. 25 Hz). Interessanterweise wurde die Frequenz der Oszillationen durch die Bewegungsrichtung der Gitterreize moduliert. Der Modulationseffekt fluktuierte in einem Bereich von 3 Hz. Dies deutet auf die potenzielle Rolle hin, die oszillatorische Frequenzen beim Kodieren von Reizmerkmalen spielen.

In der zweiten Untersuchung habe ich an der Entwicklung von skalierten Korrelationsanalysen (scaled-correlation analysis) gearbeitet. Dies ist eine Methode, die die gesonderte Analyse von Auto- und Karenzkorrelationen von schnellen Signalkomponenten ermöglicht. Ich habe den analytischen Beweis erbracht, dass ‚scaled correlation' auf implizite Weise niedrig-frequente Komponenten des Signals dämpft und dabei ähnlich funktioniert wie ein Hochpassfilter.

In der dritten Untersuchung habe ich die Beziehung zwischen der Statistik von Spike Zeiten und den Regeln für Spikezeit abhängige Plastizität (Spike timing dependent plasticity) untersucht. Es ist bekannt, dass die STDP durch ein Zeitfenster von 100ms charakterisiert ist,

innerhalb dessen die plastische Modulation von Synapsen erfolgen kann. Ergebnisse aus früheren Arbeiten unserer Gruppe (Schneider et al., 2006; Havenith et al., 2011) sowie Ergebnisse von König et al (1995) zeigten, dass sich relative Spikezeiten mit den Stimuluseigenschaften ändern und in der Statistik erster Ordnung widerspiegeln. Diese relativen Spike-Zeiten überschreiten nicht die Dauer von 15 ms. und fallen damit in den Bereich der STDP.

Unter Verwendung eines ‚random walk' Modells der STDP und unter Annahme von Poisson verteilten Spikesequenzen, habe ich die ersten beiden Momente der stochastischen Entwicklung der synaptischen Gewichtung über die Zeit beobachtet. Dabei wurde deutlich, dass die mittlere synaptische Gewichtung im Gleichgewichtszustand stark von zwei Faktoren abhängt: Der Grad der Synchronizität von prä- und postsynaptischen Spikes und den relativen Spikezeiten. Diese Bedingungen gelten sowohl für das additive wie für das multiplikative STDP Modell. Zusätzlich zu dieser theoretischen Arbeit habe ich abgeschätzt, ob in-vivo aufgezeichnete Spikes in der Lage sind, hypothetische synaptische Verbindungen zwischen den aufgezeichneten Neuronen zu modifizieren. Die Spikes wurden dazu in ein simuliertes STDP Modell, das ‚Supression Modell' (Froemke und Dan, 2002) eingespeist. Die Ergebnisse waren mit denen vergleichbar, die von der theoretischen Analyse vorausgesagt wurden. Dies gilt sowohl für die unterschiedlichen STDP Modelle (Suppressionsmodell vs. Additives Modell) als auch für die unterschiedlichen Spikesequenzen (Gamma Band moduliert vs. Poisson verteilt). Ich konnte zeigen, dass sich die Vorhersagen des ‚Supressions-Modells' denen des ‚Additiven Modells' annähern, wenn die Spike Rate sehr niedrig wird.

Zusammenfassend ergibt sich, dass die Frequenz von oszillatorischen Prozessen in einer Abfolge von Spikes als potenzieller Mechanismus zur Kodierung von Stimulus-relevanter Information gesehen werden kann und dass diese Phänomene auch dann mit skalierten Korrelationsanalysen effizient untersucht werden können, wenn die Spikesequenzen mit

niedrig-frequenten Signalkomponenten angereichert sind. Zeitliche Verschiebungen in der Synchronizität der Spike Abfolgen kann die Konnektivität zwischen den zugrundeliegenden Netzwerken durch STDP signifikant beeinflussen.

Summary

Neural synchrony is a curious phenomenon of the brain and has been studied now for decades. In this thesis, I made further steps in investigating the functions of neural synchrony using two approaches: analysis of the spike trains recorded from cat primary visual cortex, and theoretical analysis of simulated spike trains.

In the first study, I investigated autocorrelations of the spike trains in response to moving gratings. Essentially, the autocorrelation is a second order statistic of spike times. The majority of the observed autocorrelations were oscillatory with an average period in the range of beta/gamma band (~ 25 Hz). Interestingly, the oscillation frequencies were modulated by the direction of the moving gratings. This modulation effects fluctuated in the range of ~ 3 Hz. Those revealed the potential coding capabilities of oscillation frequencies in the spike trains.

In the second study, I contributed to the development of scaled-correlation analysis. Scaled correlation analysis is a method that enables the isolation of autocorrelation and cross-correlation histograms of fast signals components. I produced an analytical proof that scaled correlation implicitly attenuates the slow-frequency components in a similar way as a high-pass filter.

In the third study, I investigated the relation between statistics of spike times on one side and the rules for obtaining spike time dependent plasticity (STDP) on the other side.

It is well established that STDP is characterized by a time range of ~100 ms within which the spike time dynamics can lead to plastic modification of synapses. Results of previous studies in our group (Schneider et al. 2006, Havenith et al., 2011) and those of König et al (1995) showed that the difference of the first order statistic of spike times, i.e. the relative spike times

change with the stimulus property. These relative spike times do not exceed ~ 15 ms. Therefore, the range of relative spikes time falls into the range of STDP.

Using a random walk model of the STDP and assuming Poisson spike trains, I derived the first two moments of the synaptic weights evolving stochastically over time. It became clear that the average synaptic weight at the equilibrium depends most heavily on two factors, the level of the synchrony between input and output spikes, and the relative spike times. We obtained the same results for an additive and a multiplicative STDP model. In addition to the theoretical work, I estimated the degree to which spikes recorded in vivo were able to modify the putative synapses which may exist between the recorded neurons. The spikes were fed to an experimentally established and computer-simulated STDP model, known as the suppression model (Froemke and Dan, 2002). Results for suppression model were comparable to those obtained from the theoretical analysis, despite the marked difference between the STDP models used in the two analysis (suppression model vs. additive model) and between the spike trains (patterned in the gamma-band vs. Poisson distributed). I could show that this is due to the fact that the prediction of the suppression model converges to the additive models of STDP when the rate of spikes is sufficiently low.

In conclusion, the present work shows that the frequency of oscillatory patterns in spike trains can be used potentially to code stimulus-related information, these phenomena can be studied efficiently using scaled-correlation even if spike trains are polluted with slow-frequency components, and the time-delays in the resulting synchrony between spike trains can significantly affect the connectivity of the underlying network via STDP.

Table Of Contents

Chapter 1 - General Introduction

1.1 A short review of visual coding

The primary sensory pathway for processing visual information consists of three stages. The first stage is the retina, where the visual stimuli are converted to neural activity of the ganglion cells. Ganglion cells then project to the lateral geniculate nucleus (LGN), which serves as a relay hub and a pre-processing filter, forming the second stage. The third stage is the primary visual cortex, which receives the input from and project back to LGN (Orban, 1984; Waxman, 2010).

When the neurons respond to the visual stimulus, the temporal precision of the spiking is often high (Tiesinga et al., 2008; Bair and Koch 1996; Carandini et al., 1996; Schroeder et al., 1998). This can be easily seen by computing raster plots or the peri-stimulus time histogram (PSTH) of the spikes recorded from multiple trials (Dayan and Abbott, 2001). In a raster plot, an aligned trace of spikes in response to the stimulus indicates high response precision. In the PSTH, a precise response is represented by a narrow peak produced by a transient increase of firing rate. Along the stages of the visual pathway, although the precision of the spiking response can be consistently high (Tiesinga et al., 2008), the reliability of spiking can reduce (Kara et al., 2000). For example, the spikes recorded in response to grating stimuli in visual cortex are less reliable than in LGN (Kumbhani et al., 2007). It has also been reported that the spike count variability measured by the Fano factor is larger and the firing rate is lower in visual cortex than in LGN and retina in anaesthetized cat (Kara et al., 2000). Base on these findings, one can postulate that the firing thresholds of the visual cortex neurons are possibly higher than the LGN and ganglion cells (Carandini, 2004). Besides the effects of higher firing thresholds, the recurrent IPSPs induced by the EPSPs may also be responsible for the precise but less reliable responses of neurons in visual cortex as compared to LGN (Blair, 1999).

The precision of spiking is possibly modulated by both the inputs and feedbacks. It has been shown that the precision of the responses of LGN cells co-varies with the frequency content of the visual stimulation, such that the variance of responses to the natural scene is bigger than of responses to the uniform noise (Butts et al., 2007). Similarly, the precision of spikes for the monkey MT cells is high only when the visual stimuli are in-coherent (Blair and Koch, 1996). As a form of feedback modulation, McAlonan et al. (2008) reported that attention modulates the responses of thalamus to visual stimulus in behaving monkeys. Given that this regulation effect occurs via a balance of local inhibition and excitation, which may be crucial for the modulation of firing thresholds, it is highly likely that such top-down modulation also plays a role in regulating the precision of spike times in the visual system.

Precise spike timing is one of the factors for visual coding. Besides the precise spike timing, other factors may play a role in coding the visual information. These include firing rates, firing patterns, the relationship between the spikes and the ongoing reverberant field potential, and the timing relationship between the spikes of neurons.

Firing rates of the visual neurons are determined by synaptic inputs driven by the visual stimuli. Those synaptic inputs and the feedbacks are wired such that the properties of the visual stimulus can be represented by the efferent firing rates. For example, firing rate can be modulated by the moving direction, size and contrasts of the visual stimulus. Typically, a transient change of firing rate occurs at the stimulus onset for the visual neurons. This effect is larger when the feature of the stimulus matches the preferences of the neurons. In response to the constant stimulation, the firing rate of the V1 neurons tends to stabilize after the initial onset transient and change abruptly again at the offset of the stimulus. As a simple formulation of coding mechanism, the firing rate can be described as a linear function of certain features for the visual input, time and noise (Gerstner, 2001). It follows that the

characteristic of the neuron can be described by a reverse correlation method (Dayan and Abbott, 2001). An example of this approach is the mapping of the receptive field. The spikes responding to visually presented Gaussian noise are evaluated to find the kernel of modulation. Usually the receptive fields of the visual cortex neurons thus quantified resemble 2-D Gabor patches (Jones and Palmer, 1987; Ringach et al., 2002). More elaborate firing rate models take into account not only the stimulus-driven factors, but also the capacitance properties of the cellular membrane and the frequency response of the firing rates as in the "sandwich model" proposed by Carandini et al (1996).

Compared with the firing rate, the relationship between firing patterns and the visual stimuli is less overt. It has been shown in model neurons that the firing patterns emerge when the distribution of membrane potentials has separated peaks (Tiesinga and Toups, 2005). Using clustering techniques, the same study identified the firing patterns of spike trains in response to artificial stimulations. For the data recorded in visual cortex, direct observation usually does not reveal much regularity of spike times. At least this is the case when the visual stimulation is continuous (e.g., a light-bar passing over a receptive field) rather than transient (e.g., flashed stimuli). For the continuous stimulation, spiking activities tend to be more random during the persistent stimulation than during the onsets or offsets of the stimulation.

Besides the method proposed by Tiesinga et al., second-order statistics can be employed to quantify the imbedded regularity of the spikes recorded in vivo (Shinomoto et al., 2009). However, the firing patterns thus detected are less pronounced compared to in vitro or simulated data. In addition, firing patterns can be also effectively detected by characterizing the spike-count based PSTHs (Walker et al., 2008).

Firing pattern does have the capability of coding the information of the stimuli. This can be examined by quantifying the general probability of observing a certain pattern and the conditional probability of observing that pattern given a stimulus. According to analyses for data recorded from the auditory cortex of the rhesus monkey, the coding capability of the firing patterns is comparable or even higher to that of firing rates (Kayser et al., 2009). Firing rate can reflect the firing patterns in some cases as well. For example, consider an efferent neuron that surveys the inputs from a number of afferent neurons and fires in response to those inputs in a Poisson manner. In such setup, the strength of synapses can be made to evolve according to phenomenological spike-time-dependent plasticity (STDP) models. It was shown that the firing rate of such an efferent neuron reflects the firing patterns of the input neurons when those firing patterns are repeatedly implemented (Gilson et al., 2011).

The timing of the spike in relation to the phase of ongoing oscillation of the field potential is another plausible mechanism for visual coding. Although the spikes and local field potentials (LFP) all reflect the neuronal activities, their roles differ. Spikes are generated by the individual neurons and reflect the supra-threshold activities of the neurons. In contrast, the LFPs are produced by aggregated neuronal activities, reflecting not only the supra-threshold but also the sub-threshold potentials. Thus if one assumes that spikes reflect the output of the neuronal circuits, then at least to some extent, the LFP represents the inputs (Mazzoni et al., 2012).

It has been shown that the phases of the spikes relative to ongoing LFP are not randomly distributed (Montemurro et al., 2008; Vinck et al. 2010; Denker et al., 2011; Havenith et al., 2011). Rather, the distribution of the spike phase is stimulus-dependent. A classical example is the relationship between the spike phase of the place cell and the LFP recorded in the rat hippocampus. The spike phase of the cells moves across the theta oscillation cycle

contingently with the physical position of the animal (O'Keefe and Dostrovsky, 1971; O'Keefe and Recce, 1993).

The coding mechanism by firing phase is closely related to the phenomenon of neuronal synchrony. The analysis of the data recorded from monkey brain showed that, the coherence between the multiunit activities (MUA) is maximal around the gamma band (~60 Hz). This implies that the gamma band oscillation is closely related to the neuronal synchrony. The same study showed that the correlation between MUA is highest when those MUAs are locked to a certain LFP phase, which were found to be the mean spike phase of the MUAs (Womelsdorf et al., 2007). Along this line, the results of the simulated neuronal networks support the putative link between the gamma oscillation and the neuronal synchrony. Using the transfer entropy method, Buehlmann et. al. reported that the predictive information between the MUA groups increases when the gamma oscillations are enhanced (Buehlmann, 2010).

Judging from the distribution, the firing phase alone does not have sufficient signal to noise ratio (SNR) for coding information. However, results showed that there is generally a boost of information when the phase coding is incorporated into the firing rate or firing patterns (Kayser et al., 2009; see also Montemurro et al., 2008).

There is evidence beyond theoretical considerations for the role of firing phase in coding. For example, Fries et al. (2001) showed that the gamma band power of the spike triggered average (STA) of the LFP is modulated by attention. For spikes recorded in the monkey V4, it has been found that spikes evoked by preferred stimuli exhibit stronger locking to the 'good' theta phase, than those evoked by the non-preferred stimuli. This was observed during a task that involves working memory (Lee et al., 2005).

Phase locking of spikes also has putative functions in affecting synaptic plasticity. Lengyel et al. (2005) showed that if memory is stored in a Hebbian manner by the STDP and the neurons optimize the retrieval of the memory traces stored by the STDP, an interesting phase response curve should emerge. This phase response curve is characterized by the firing phase of post-synaptic neuron as a function of the firing phase of the pre-synaptic neuron. In this case, the synaptic plasticity that is related to the memory trace is reflected by the firing phase.

The relationship for spike timings between the neurons is related to the hypothesis of the coding by firing phase. If the neurons close to each other share the same ongoing field potential, their spike time relations essentially translate to their firing-phase relationships. A study in our group reported that for the single-unit activities recorded from electrodes ~200 microns apart, the offset of the cross-correlation (CC) for the spike time preserves an additive relationship throughout all pair-wise comparisons between neurons when the underlying beta/gamma oscillation is pronounced (Nikolić, 2007). This result is interesting in the light of the fact that the spike times of recorded neurons in this study are not independent, but correlated. Therefore, the offset of a CC essentially is a result of correlation in spike times rather than a putative difference of average spike times recorded from neurons firing independently. It can be postulated that the neurons fire in reference to the underlying gamma oscillation cycle (Fries et al., 2007). In addition, the strong gamma oscillation boosts the firing reliability of the neurons, thus giving rise to the additive relationship described above.

Closely related to the hypothesized phase coding, studies in our group (Nikolić 2007, Havenith et al., 2011) and by Vinck et al. (2010) found that the expected activation time of cat visual cortex neurons changes with stimuli. As described above, the relative spike time of neurons can be assessed by the offset of the CC. This offset was found to be changing with the moving direction of the presented gratings (Havenith et al., 2011). A comparable result

was reported by Vinck et al., showing that the phase of the spikes changes as a function of moving direction of the gratings. Further, they showed that the coding capacity of the activation time was compared to that of the firing rate. Not surprisingly, the mutual information to the stimulus of the former is less than that of the latter. As discussed in the case of phase coding, activation time or its equivalent spike phase could be incorporated with the firing rate in order to achieve always a superior coding strategy.

The other important issue, which is more general than the coding of spike timing, is whether the correlation of activities between the neurons or among the neuronal groups would optimize coding. This is an important question besides the issue of different coding mechanisms that are most likely to be concurrent in the brain.

Different approaches have been applied to isolate the effect of correlation on neural coding. For example, a comparison can be made between the information of the data and that of the surrogate data, which is produced by permuting the trial labels. It was found that there is always a reduction of correlation between the neuronal activities for the surrogate data compared to the raw data (Louis et al., 2010). The amount of information for surrogate data therefore can serve as a reference of the information associated with correlations. From the theoretical point of view, the contribution of correlation in decoding is not always positive or negative. As a comparison between the information of the data and that of the surrogates, Averbeck et al. (2006) showed that the difficulty of decoding in shuffled data is decreased compared to the data, in which signal and noise correlations (Cohen and Kohn, 2011) of neuronal responses are both positive (Figure 1). In contrast, this difficulty of decoding can be either increased or unchanged when the signal and noise correlations are not both positive. One should also note that the difficulty of decoding corresponds to the changes of mutual information. An increase in difficulty of decoding corresponds to a decrease of mutual

information. The experimental results also generally showed that this difference is small (Petersen et al., 2001; Nirenberg et al., 2001). As a result, the net outcome depends on the exact pattern of correlation between the neuronal activities.

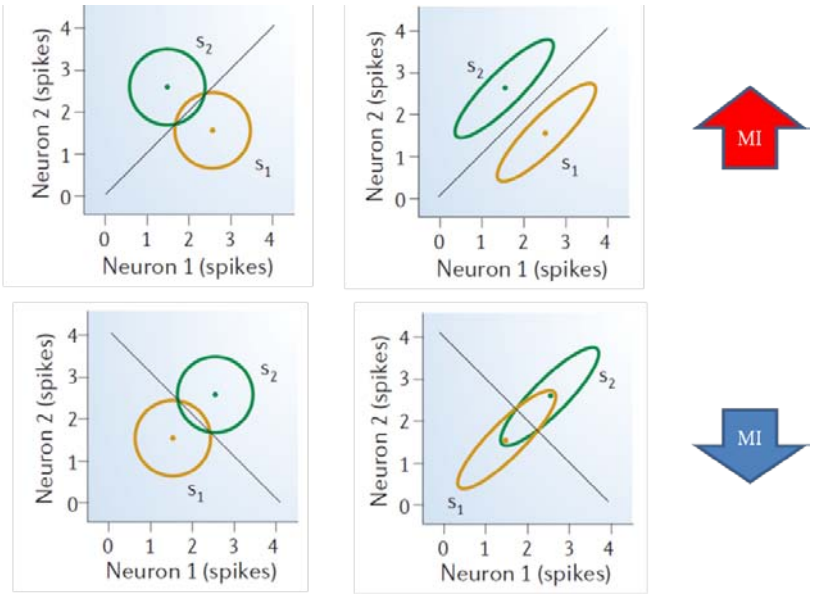

Figure 1: Effect of correlations on information encoding. Joint neuronal activities are plotted for stimuli s_1 and s_2. MI: mutual information. Linear correlation of neuronal activities can lead to either an increase or a decrease in mutual information. Adapted from Averbeck et al., 2006.

In another, purely statistical approach, one can assume that there is a cost of ignoring the correlations when making inferences about the stimulus based on the knowledge of the neuronal responses. Under the assumption of optimal decision-making, this cost can be quantified by substituting the posterior, which is the probability of observing the stimulus given a certain response, by another posterior assuming that all responses are independent. The cost evaluated as such is generally nonnegative. However, this result alone does not suffice to draw any conclusions, since the other confounding factors are not eliminated. Those factors are, for example, a consideration of whether the correlation is stimulus-dependent and whether the correlation actually exists or not (Nirenberg and Latham, 2003). By and large, it is difficult to conclude generally whether the correlations between the neuronal responses are

good or bad for decoding, but it is certain that a combination of different coding mechanism will generally be beneficial.

Besides pair-wise correlations, correlations involving more than two neurons have also been extensively studied. These correlations are commonly referred to as non-pairwise correlations or high-order correlations (Roudi et al., 2009). In the primary visual cortex, the neurons that have similar directional preferences are connected via the horizontal connections (Hirsch and Gilbert, 1991). This implies that the non-pairwise correlation exists at least as signal correlations. To observe the neuronal responses for pair-wise and non-pair wise correlations, one needs to quantify the firing pattern as joint activities. The firing patterns can be defined as the binary vectors that represent binned spiking activity for a number of neurons. Note that this firing pattern reflects the instantaneous activities for multiple neurons, rather than the pattern of spiking response for one particular neuron.

To isolate the information related to pair-wise correlations relative to all other correlations, the information related to correlations should be quantified first. This effect can be shown by the difference between the entropy of the observed joint responses and the sum of entropies for the individual neuronal responses. Since the latter represents the entropy when the responses between the neurons are independent, this difference represents the effect of correlation. One can further identify the effect of the pair-wise correlation by taking the Kullback-Leiber (KL) divergence between the observed jointed-response and the responses assuming only pair-wise correlations. The KL divergence between the true observed jointed-response and the independent responses are similarly defined. The ratio between those two KL divergences quantifies the effect of the pair-wise correlation relative to any form of correlations. This ratio ranges between zero and one (Roudi et al., 2009). Note that as a general condition, the entropies of the response for pair-wise correlations are always

maximized. The maximization is made to be consistent with the marginal distributions for responses of individual neurons, and with the constraint of the measured firing rate and the covariance of neurons.

In another study using the maximum entropy model, it has been shown that if one relates the entropy to the order of correlation that is allowed to exist, there is always a reduction of entropy as the order increases. One can thus define a sum of series representing the contribution of the entropy for the *k*-th order correlations. For the activity of ganglion cells in response to the natural scenes, the ratio of the information of pair-wise correlation to that of any correlation reaches 90 percent (Schneidman et al., 2006). This means that for the group size of ten neurons, which were randomly selected from the pool of recorded ganglion cells, pair-wise correlations capture the overall correlation structure effectively.

A recent study investigated the effect of high-order correlations with a similar approach. Instead of using the maximal entropy models, the dichotomized Gaussians (DG) was used. The DG is a model that has been applied for generating the correlated spikes (Macke etc, 2009). The data generated by the DG model successfully reproduced the neuronal avalanches, which is one of the prominent characteristics of the neuronal activities. The entropy maximization model reproduced avalanches less well than did the DG model. Given that the DG model itself introduces high-order correlations, one can infer that non-pair-wise correlations are required to account for the complex coding of neuronal networks (Yu et al., 2011).

By and large, the high-order correlations can indeed be quantified. However, it is still not clear whether they play an important role in neural coding.

1.2 Neuronal Synchronization

In the primary visual cortex, a simple cell receives monosynaptic inputs from as many as 30 afferent LGN cells (Payne and Peters, 2002). The question that follows naturally is how those inputs drive the efferent simple cells. It is obvious that an efferent cell is more likely to fire if the afferent spikes times are close to each other. In fact, LGN cells do fire in a correlated manner because the ganglion cells usually send collateral inputs to LGN cells. As many as 40 percent of spikes from correlated LGN cells can occur within a window of 1 ms (Bair,1999 ; Payne and Peters, 2002). This result can be quantitatively assessed by drawing cross-correlation histograms (CCH) for the activities of LGN neurons. In such CCHs, higher synchronicity leads to a larger main peak, usually around zero lag in time.

In the above example, the synchronized LGN afferent inputs represent one case of the neuronal synchronization. The synchronous firing of afferent neurons also exhibits a synergic effect for driving the efferent neurons. As mentioned above, the level of the neuronal synchrony can be reflected by the CCH. Typically, a flat CCH indicates weak correlation and synchronicity. Synchronous firing of two neurons produces a CCH that has a prominent central peak close to the zero lag (König, 1994; König et al., 1995). Different organizations of the stimulus can lead to either asynchronous or synchronous CCHs (Kreiter and Singer 1996).

Neural synchrony is stimulus-related. In one study by Gray et al. (1989), the visual stimuli were designed either as two short bars drifting in the same direction or opposite directions, or as a single drifting bar twice as long as the short bars. Neuronal responses to such stimuli were recorded in area 17 of anaesthetized cats. Gray et al. found that the CCH was most synchronous during the presentation of single long-bars (Figure 2). The neuronal responses to two shorter bars drifting in the same direction also produced synchronous CCHs, which was

not as strong as those for the single-bar stimulus. In comparison, the CCH was asynchronous to the stimulus of two bars drifting in opposite directions. Similar results were also reported for stimuli of crossing bars instead of aligned bars (Kreiter and Singer 1996). Based on this line of discoveries, it was hypothesized that the neuronal synchrony serves as a way of binding the parts of an object, such that the object can be perceived as a single entity. This hypothesis is known as "binding by synchrony" (von der Malsburg, 1981; Gary, 1999; Singer 1999).

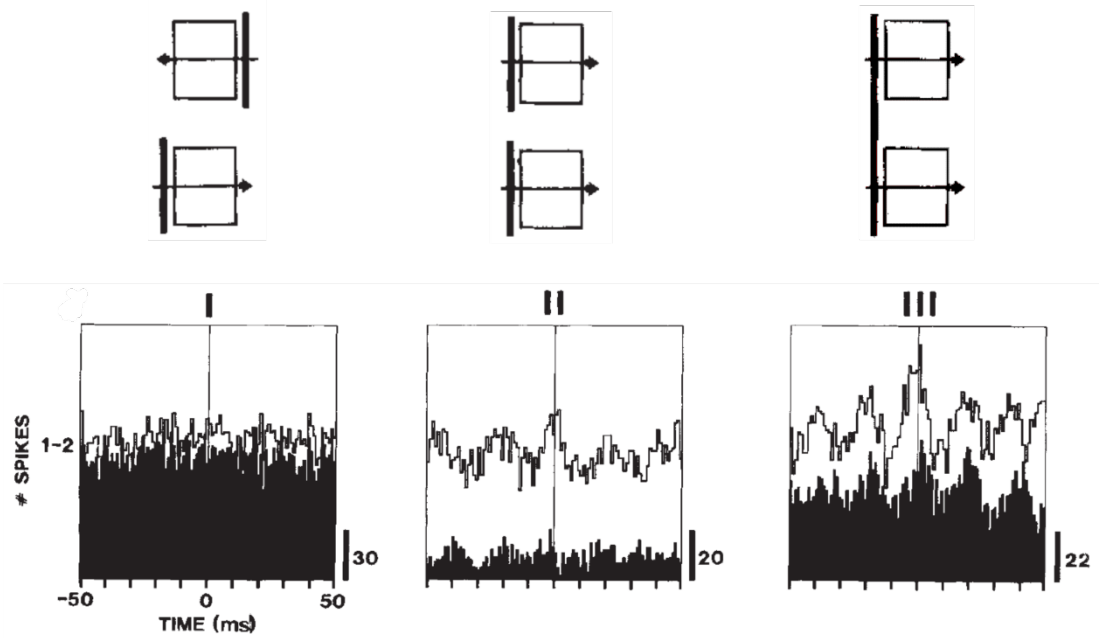

Figure 2: Cross-correlation reflects global stimulus properties. The schematic diagrams of neuronal receptive fields and stimuli are plotted at the top. Cross-correlations plotted below show that the single long-bar stimulus elicited strongest neural synchrony. Adapted from Gray et al., 1989.

However, careful inspections reveal that the detection of synchronicity from the CCH may not be sufficient by itself. The reason is that the cross-correlation is heavily affected by the firing rates. Imagine that there exist two sequences of spike impulses. The probability of finding a spike in the first sequence two, one or zero millisecond away from a spike in the second sequence becomes larger as the firing rates increases. Therefore, in principle a confidence

interval of CCH should always be constructed for testing the synchronicity. Comparing the observed CCH to the shift predictors by direct observations would not suffice (Grün and Rotter, 2010).

Apart from the interval estimation, another common concern for the CCH of the spike time is that in such CCHs effects of fine temporal-dynamics are inevitably blended with those of the slowly varying firing rates. Although various methods have existed for removing the slow trends in signals, such as filtering and de-trending, an efficient method is still needed especially for calculating a CCH of the binary data such as spike times. To this end, I worked on a new concept of correlation, the scaled correlation analysis, which is discussed in Chapter Three.

Synchronization can also be described by coupled oscillators in physics. Generally, the spiking activities can be approximated as limit cycle oscillators. The membrane potential during firings oscillates in a regular manner resembling the limit cycle. For example, a simplified neuronal model originated from the model of integrate-and-fire neurons is the Terman-Wang oscillators (Terman and Wang, 1995). For those oscillators, in an enabled state, the membrane potential has the dynamics that resemble those of Van der Pol oscillators, which are limit-cycle oscillators (Wilson and Cowan, 1972; Gros, 2008).

In this context, synchronization essentially happens when the oscillators are locked to a common oscillation frequency. Coupling is the force that drives the oscillators having different natural frequencies to lock with each other. For example, a function of the phase difference of oscillators can establish coupling. In particular, if this function is a sinusoidal, it is called the Kuramoto Model (1975).

One feature of the Kuramoto Model is that when the coupling strength is higher than a critical value, the phases of oscillators tend to converge to a common ensemble phase. In a steady state, the distribution of the phase of the oscillators will therefore be concentrated around this mean phase. However, if the coupling is low, oscillators will not synchronize their phases and the phase of individual oscillator will tend to evolve independently. For the neurons in general, and in particular for the afferent neurons of the LGN, common collateral input will guarantee a strong coupling. In this case the synchronous neural activities are comparable to harmonic oscillators driven by the external oscillating force. In other cases, for example in the case of strong theta or gamma field potentials, the common oscillatory activities of neuronal membrane potentials may provide a form of coupling strong enough to synchronize neuronal spiking.

The hypothesis of "binding by synchrony" mentioned earlier can be investigated theoretically with a network of synchronized oscillators (Figure 3). One can assume that a local excitation effect should exist as feed-forward input to neurons. Meanwhile, globally neurons are inhibited if at least one of them is active (Wang and Terman, 1997). In this model, feed-forward inputs can drive the neurons so that they are capable of representing a feature of the object when their activities are synchronized. As a counterbalancing force, a global inhibition suppresses the oscillators that do not receive such feed-forward inputs.

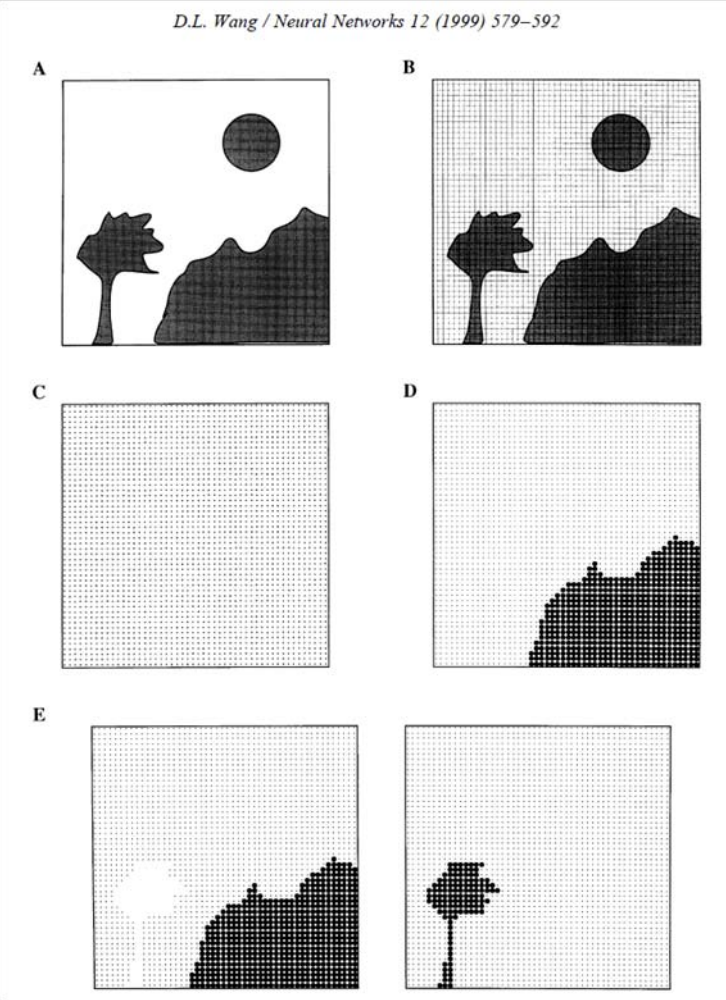

Figure 3: Segregation of different figure patterns by a 2-D selection network. Reprint from Wang, 1999.

It turns out that such a network can indeed identify the components of an object (Wang and Terman, 1997). For example in a 2D layout, neurons that represent one part of the object fires synchronously in one cycle while the rest of neurons are silent. As time evolves, neurons representing the other parts of the object fire in synchrony consecutively. Therefore, different parts of the object can be segregated by the consecutive synchronization of the neuronal activities. However, one can argue that this network is highly non-biological. For example, no parallel computation is in any way facilitated by the synchronization. Besides, the global inhibition employed in this model is a rough method, which definitely does not take into account the complex role of inhibition for the neuronal circuits. Nevertheless, such a network is functional. Yet, it reveals the complexity for testing the hypothesis of binding by synchrony.

As already discussed in the section of visual coding, the correlation of neuronal activities does not always make the decoding easier. According to the hypothesis of “binding by synchrony”, one should infer that once the neuronal activities representing a certain feature are synchronized, the change of the information (ΔI), representing the difference between information of synchronized responses and that of the shuffled responses, should be large and positive.

Indeed, this difference of information was found positive (Golledge, 2003). In the same study the mutual information between the stimuli and the responses was categorized into three sources. The first source was information carried by the firing rate of the channels, of which the responses are independent. The second and the third represented the information of the responses that were correlated. The second source (I_{cor_dep}) assumed that the correlation is dependent on the stimuli. In contrast, the third assumed that the correlation is independent of the stimuli. Therefore, I_{cor_dep} is comparable to ΔI defined earlier. The result showed that I_{cor_dep} was not correlated with the stimulus conditions, which were either a long single bar or two opposing bars moving in a certain direction. Secondly, I_{cor_dep} was not correlated with the optimality of the stimuli.

Clearly, those findings contradict the hypothesis of “binding by synchrony”. It is important to note that the responses were defined as the number of spikes in the study mentioned above. However, in order to precisely assess the coding of the responses, one should not restrict the spiking activities to a counting process and thus overlook other factors. Among those other factors is for example, the precise spike timing. A similar approach with the analysis of spike patterns should be adopted, rather than just investigating the firing rates.

1.3 Spike timing dependent plasticity

The efficiency of the synapses can be directly modified in experiments. For the excitatory synapses, a common indicator of the efficiency is the amplitude of the excitatory post-synaptic potentials (EPSPs). For a certain afferent input, the increase of the synaptic efficiency is reflected by an increase of the EPSP amplitude. A decrease in synaptic efficiency results in a reduction of the EPSP amplitude. It has been found that when the excitatory synapses are repeatedly stimulated by the external electrical pulses of about 100 Hz, the amplitude of the EPSP increases. However, if the same synapses were stimulated with repeated stimulation of slow frequency, the amplitude of the EPSP decreases (Sjöström et al., 2001).

The change of the synaptic efficiency is closely related to the glutamate receptors. There are at least two types of glutamate receptors involved: the AMPA receptors (α-amino-3-hydroxy-5-methyl-4-isoxazolepropionic acid) and the NMDA receptors (N-Methyl-D-aspartate). The AMPA receptor is permissible for mono-valent cations, like sodium and potassium. The activation of the AMPA receptor by the glutamate will allow the influx of sodium cations. Thus the post-synaptic membrane potential is depolarized when the AMPA receptors are activated. In contrast, the NMDA receptors are permissive to the calcium and normally under the blockade of magnesium. The magnesium blockade is modulated by the post-synaptic membrane potential. It is commonly believed that the NMDA receptor plays an important role in various forms of synaptic plasticity (Caporale and Dan, 2008).

Besides the induction of the plastic change by adjusting stimulation frequency, the spike timing can also modulate the synaptic efficiency. In a typical setup, the pre- and post-synaptic neurons are repeatedly stimulated. The stimulation is such that the firings of the two neurons

are paired, i.e. the post-synaptic neuron fires only after (or before) the pre-synaptic neuron. Such paired activity is made to repeat for ca. 60 times with a frequency of about 30 Hz (Dan and Poo, 2006). The result of this is either a boost or a decrease of the EPSP amplitude, depending on the relative firing time of the pre- and post-synaptic neurons (Figure 4). Typically, the change of the EPSP amplitude could be as large as 50 percent, being positive or negative. This form of the synaptic plasticity is referred as the STDP (spike-timing-dependent plasticity). Examples of STDP are shown in Chapter four. In Chapter Four, I focus on the putative relationship between the STDP and the neuronal synchrony discussed in the previous section.

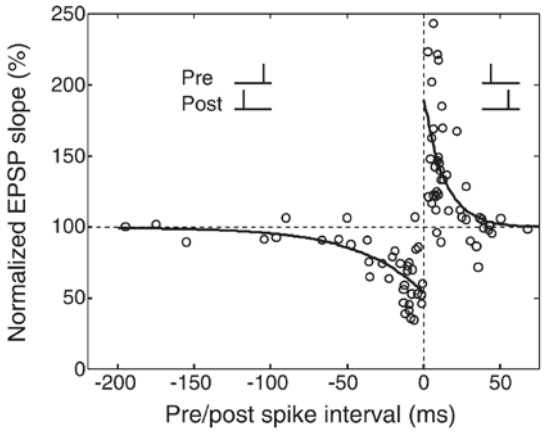

Figure 4: Synaptic modification induced by repetitively pairing of pre- and postsynaptic spikes in layer 2/3 of visual cortical slices from the rat. Positive values of time intervals indicate that the presynaptic neuron fires before the postsynaptic. Values of EPSP larger than 100 indicated potentiation and below 100 depression. Reprint from Dan and Poo, 2006.

The NMDA receptor also plays an important role in the STDP. As mention above, the LTP can be induced by pairing the pre- and post-synaptic spikes with positive intervals. This effect is probably mediated by the NMDA receptor (Dan and Poo, 2006). The important factor here is the back propagating action potential (BAP). When the post-synaptic cell fires after the pre-synaptic cell, the BAP unblocks the magnesium blockade of the NMDA receptor. Thus, once the NMDA is activated, the calcium influx mediated by the NMDA receptors gets stronger,

leading to an increase of the EPSP amplitude. When the pre-synaptic neuron fires after the post-synaptic neuron, the after-polarization of the BAP instead impedes the activation of the NMDA receptors, allowing only a moderate influx of the calcium. This may produce a decrease of the synaptic efficiency observed in the STDP. Essentially in these cases, the NMDA receptors serve as a form of coincidence detectors for the pre- and post- synaptic spikes. Alternatively, during the induction of LTD in the STDP, the BAP may activate the voltage-dependent calcium channels (VDCCs), which allow the calcium to flow into the cell. This influx of calcium deactivates the NMDA receptors, which subsequently only make the calcium influx a moderate one, leading to the LTD (Caporale and Dan, 2008; Citri and Malenka, 2008).

As a phenomenological model, the evolution of the synaptic weight can be described as a causal process involving dynamics of local variables (Morrison et al., 2008; Williams et al., 2003). In this model, the pre- and post- synaptic spikes produce the traces that decay exponentially. The amplitude of the post-synaptic trace at the time of pre-synaptic spikes determines the amount of potentiation. Similarly, the depression is determined by the amplitude of the pre-synaptic trace at the time of post-synaptic spikes. Besides, a window function is defined to rescale the change of the synaptic weight, such that the change of weight is suppressed when the weight is higher. Essentially, an adoption of the window function precludes the excessive change of the synaptic weight, which is non-biological. Thus, dynamics of the synaptic weight can be described by considering the depression, the potentiation, as well as the window function.

The windows functions that substantially affect the learning dynamics of the STDP models can be categorized as being either additive, multiplicative, or intermediate. The evolution of additive STDP does not dependent on the synaptic weight, whereas the update of

multiplicative STDP always depends on synaptic weight. The fixed-point analysis of the update rule revealed that an additive window function does not lead to the stabilization of the synaptic weight. In contrast, multiplicative STDP models always result in stable fixed-points of the synaptic weight. For the scheme of a post synaptic neuron receiving multiple pre-synaptic inputs, the weight distribution for multiple synapses should be uni-modal rather than bi-modal when the multiplicative update rules are adopted. This prediction is in line with the biological results (Robin et al., 2001; Gültig et al., 2003).

Chapter 2 - Frequencies of gamma/beta oscillations are stably tuned to stimulus properties.

Frequencies of gamma/beta oscillations are stably tuned to stimulus properties

Weijia Feng[a,b], Martha N. Havenith[c], Peng Wang[a,b], Wolf Singer[a,b] and Danko Nikolić[a,b]

Stimulus-induced changes in oscillation frequencies may affect information flow in the brain. We investigated whether the oscillation frequency of spiking activity in cat area 17 changes as a function of the drifting direction of sinusoidal gratings. Oscillation frequencies were tuned to specific drifting directions, such that some directions induced higher oscillation frequencies than others. When activity from the same neurons was recorded at a later time point, the average oscillation frequency with which the neurons responded had also often changed. However, the direction tuning of the neurons' oscillation frequencies remained constant. Thus, while the overall oscillation frequency, across all drift directions, was state-dependent, the relative change in oscillation frequencies induced by stimulus properties was not, the tuning remaining stable. *NeuroReport* **21:680–684 © 2010 Wolters Kluwer Health | Lippincott Williams & Wilkins.**

NeuroReport 2010, **21**:680–684

Keywords: area 17, beta/gamma oscillations, drifting gratings, oscillation frequency, visual cortex

[a]Max Planck Institute for Brain Research, Deutschordenstraße, [b]Frankfurt Institute for Advanced Studies, Johann Wolfgang Goethe University, Frankfurt am Main, Germany and [c]Wolfson Institute for Biomedical Research, University College London, London, UK

Correspondence to Dr Danko Nikolić, PhD, Department of Neurophysiology, Max-Planck Institute for Brain Research, Deutschordenstr. 46, D-60528 Frankfurt am Main, Germany
Tel: +49 69 96769 736; fax: +49 69 96769 327;
e-mail: danko.nikolic@gmail.com

Received 19 March 2010 **accepted** 13 April 2010

Introduction

Oscillatory neuronal responses, as measured by electrophysiological methods, cover a broad range of frequencies and vary in a context-dependent way even within a given frequency band [1–6]. In the visual system, the strength of oscillations in the γ/β range (20–70 Hz) has been linked to various aspects of cortical processing [7–9]. In contrast, little is known about how the frequencies of γ/β oscillations change as a function of stimulus properties and how stable the frequency is over time.

Oscillation frequencies have rarely been studied. It has been reported that the oscillation frequency of multi-unit activity in adult cat striate cortex is positively correlated with the speed of a moving bar presented in front of cats' eyes [6], and that the oscillation frequency of local field potentials in adult macaque monkeys was inversely correlated with the size of a moving grating (i.e. a pattern made of multiple bars) [10]. In contrast, intracellular recordings in the visual cortex of kittens suggested no correlation between the oscillation frequency of the membrane potential and spike trains on the one hand, and the contrast, the stimulus direction (only the optimal and orthogonal to optimal directions were investigated), or the position of the moving bar, on the other hand [11]. No data are available on the effect of stimulus direction on oscillation frequencies in adult cats. In this study we address this question and analyze in detail the relations between the stimulus direction and oscillation frequency. The amplitude and frequency of neuronal oscillations exhibit a marked state dependence [3,12]. As our analysis revealed systematic relations between stimulus direction and oscillation frequency, we also analyzed whether these relations remained constant despite state dependent changes in oscillation frequency.

Materials and methods

Anaesthesia and surgical procedures

We recorded neuronal responses from four cats (three male, one female). Anaesthesia, multisite recordings with Michigan probes, and spike sorting were made with the methods reported in earlier studies [13]. All procedures were conducted in accordance with the guidelines of the Society for Neuroscience and the German laws of animal protection, approved by the ethical committee of the local government and supervised by a veterinarian.

Stimulation and recording

The visual stimuli consisted of high contrast ($C = 0.94$) sinusoidal gratings presented by ActiveSTIM (*www.actives tim.com*). The gratings moved orthogonal to their orientations in 12 different directions, equally dividing a 360°circle in 30° steps (0°, 30°, 60°, 90°… 330°). The spatial frequency, size and moving speed of the gratings were 2.4°/cycle, 12° and 2°/s, respectively. The receptive fields of the simultaneously recorded units always overlapped, producing clusters spanning up to approximately 10° of visual angle, over which the stimuli were centered. The gratings were presented for 4 s with an inter-stimulus interval of 1 s with their drift directions changing randomly.

0959-4965 © 2010 Wolters Kluwer Health | Lippincott Williams & Wilkins DOI: 10.1097/WNR.0b013e32833ae9d1

Gratings drifting in the same direction were shown 20 times. Thus, a recording block consisted of 240 stimulus presentations and lasted approximately 20 min. To test the state dependence of oscillation frequencies over a longer period of time, recording blocks were repeated 2–4 times, spanning up to 21.6 h.

In total, 40 single units were isolated. To analyze the oscillatory spiking activity, we calculated auto-correlograms for the time period of 0.3–3.5 s after the stimulus onset, with the lag ranging from -80 to $+80$ ms. The auto-correlograms were then smoothed by a moving average:

$$\hat{y}_t = \frac{y_{t-1} + y_t + y_{t+1}}{3}$$

where y_t are the coincidence counts in the bins of the raw auto-correlogram, and $\hat{y}_t$ are those of the smoothed auto-correlogram. The smoothed auto-correlograms encompassed thus time lags of $-79 \leq t \leq 79$ ms. The estimates of oscillation frequencies were obtained next by fitting the smoothed auto-correlograms with a general Gabor function [14].

Not all auto-correlograms had sufficient counts of coincident events and/or sufficiently strong oscillatory modulation to yield a reliable estimate of the oscillation frequency. The fit of an auto-correlogram was considered sufficiently good to warrant further analysis if $r^2 \geq 0.8$; and the auto-correlogram was regarded as oscillatory if it exhibited an Oscillation score ≥ 5 [15].

Out of the 40 single units initially isolated, the auto-correlograms of 25 fulfilled these requirements in at least two stimulation conditions. Out of these, 19 could be tracked continuously over at least two blocks (up to four; average 2.5). Thus, oscillation frequencies of 19 neurons were investigated across 2–4 blocks separated by 40 min – 21.6 h and in responses to 2–6 stimulation conditions (average: 3.1).

The standard error of the measured oscillation frequency was estimated by a bootstrap method [16]. For each auto-correlogram, the corresponding bootstrap auto-correlograms were produced by independent random resampling of the 20 original trials. On account of the sampling with replacement, in each bootstrap, the same trial can be drawn multiple times whereas other trials may not be included in a resample. For each auto-correlogram, we generated in total 200 bootstraps and the oscillation frequency was estimated for each. In some cases, the frequency could not be estimated because of the noisiness of the bootstrapped auto-correlograms (usually due to low firing rates). Hence, the resample size was sometimes smaller than 200, ranging between 82 and 200 (average: 178.8). The standard deviation of the bootstrap measurements was used as the estimate of the standard error of the oscillation frequency obtained for the auto-correlogram [16].

We needed to develop a significance test to investigate the effects of stimulus direction and state on the oscillation frequency. We estimated the probability that the highest oscillation frequency would coincide with the highest rate responses. The probability that this will occur by chance equals the reciprocal of the number of available stimulation conditions, c. Thus, for a neuron i, in a single recording this probability is $p_i = 1/c_i$. When multiple recordings are made, and if independence between them is assumed, the chance of observing coincidence in all of the recordings is $P_i = p_i^{r_i}$, where r is the number of recordings. Accordingly, the chance that no coincidence will be observed in at least one recording is $1 - P_i$. Finally, the probability that n out of the total of m neurons ($0 \leq n \leq m$) exhibit a coincidence in all of the recordings is given by:

$$P = \sum_{g=1}^{w} \prod_{i=1}^{m} P_i^{x_{ig}} (1 - P_i)^{1 - x_{ig}}, \qquad (1)$$

where w is the number of combinations in which n neurons can be taken out of m neurons (i.e. $w = {}^{n}C_{m}$), $x_{ig} = 1$ if the i-th neuron participates in g-th combination, and $x_{ig} = 0$ otherwise.

We also ranked the stimulation conditions according to the induced frequencies. Consequently, we needed to estimate the chance probability that a given number of neurons would exhibit consistent rankings of stimulation conditions across all recordings. Formula (1) could be used also for this purpose. P_i can be computed as $(1/c_i!)^{r_i - 1}$, where $c_i!$ is the number of ways c_i conditions can be permuted.

Results

Typically, the oscillation frequencies of neurons varied with the direction of the grating. An example for gratings differing by 30° in drift direction is shown in Fig. 1a (3 Hz change in the oscillation frequency). The spike waveforms used to sort this unit are shown in Fig. 1b and the post-stimulus time histograms on the basis of which auto-correlograms were computed in Fig. 1c. Overall, the oscillation frequencies with which neurons responded to different stimuli varied by 2.5 Hz on average, with a maximum of 6.2 Hz. This corresponded respectively to 9.4 and 23% of the gross average frequency of 26.7 Hz (averaged across all 48 recording blocks from 19 neurons). The mean standard error of the estimated oscillation frequencies was 0.8 Hz.

Oscillation frequencies tended to be highest when the neurons were presented with the optimal stimulus, that is the stimulus that produced the highest firing rate. For the neuron shown in Fig. 2a, this relation was consistent across three different recording blocks (solid, dashed and dotted lines in Fig. 2a). Altogether, this precise match between oscillation frequency and preferred direction was observed in seven neurons out of 19 (37%), and consistent across all recording blocks (2–4 recording blocks per neuron); for another two neurons the proportion of recording blocks with a match between oscillation frequency and firing rate was larger than expected by chance (Fig. 2c).

Fig. 1

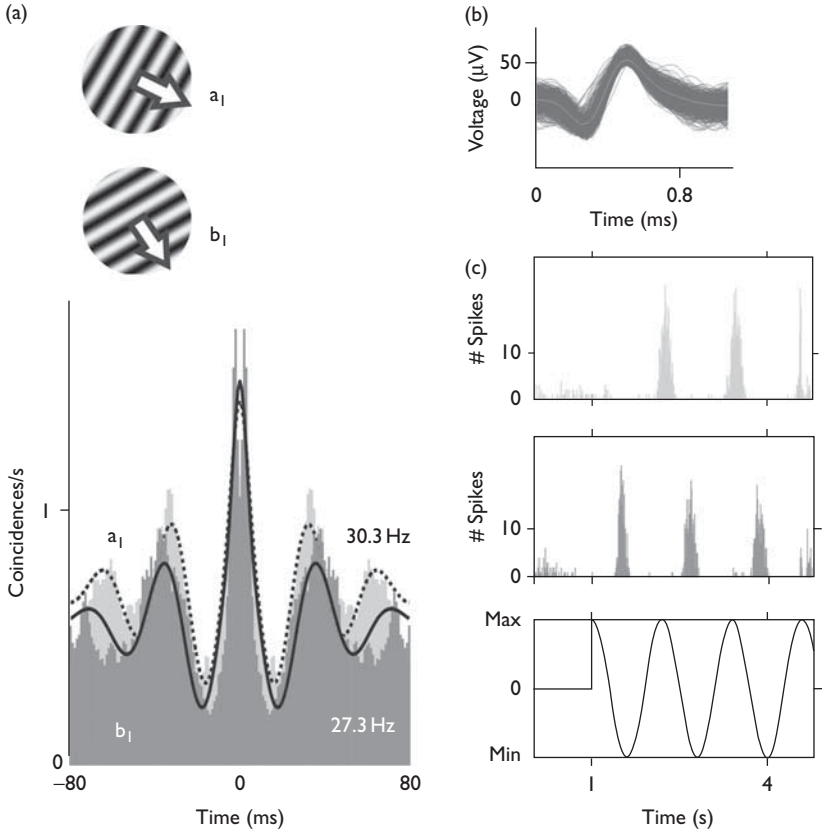

Example change in the oscillation frequency of a neuron as a function of the direction in which a grating stimulus drifts. (a) Auto-correlograms of spike trains obtained in response to two different stimuli (a_1 and b_1). The method for estimating the oscillation frequency is illustrated by the fitted Gabor functions (dashed and solid curves). The resulting estimates of oscillation frequencies are indicated on the right. (b) The waveforms of the extracellularly recorded action potentials (dark gray envelope) and the average (light grey curve) used for the unit in (a). (c) Peri-stimulus time histograms (PSTH) in response to grating a_1 (top) and grating b_1 (middle). Bottom: The stimulus-induced rhythm with which screen pixels change the luminance (*y*-axis) because of the drift of the gratings along a trial (*x*-axis).

The probability of obtaining by chance at least seven neurons with exact match between maximal firing rate and frequency is 0.003 (see Materials and methods section for the calculation procedure).

Oscillation frequency did not stay constant across recording blocks. When responses to the same stimuli were recorded several hours apart, the frequency of the oscillatory patterning in the neuron's spiking activity changed by up to 3.2 Hz. For example, in Fig. 2a, the oscillation frequency changed by 1.9 Hz between the first and the third session. These changes were usually consistent across the entire spectrum of stimuli (see e.g. Fig. 2a). For the example in Fig. 2b oscillation frequency was reduced by approximately 3 Hz in recording block 4 in comparison with blocks 1–3 across all four stimulus directions.

Despite the changes of the mean oscillation frequencies, the relative modulation as a function of the grating's drift direction remained constant. This relative constancy was independent of the overall changes in the oscillation frequency. Hence, in a recording block in which oscillations were predominantly slow, the differences across stimulus conditions were about the same as in a recording session in which the oscillations were overall fast. Examples of 'frequency patterns' representing the changes in the oscillation frequencies for different stimuli are shown for one neuron across three recording blocks in Fig. 2a and for two neurons across four blocks in Fig. 2b.

To quantify the degree to which the frequency patterns stayed stable over time, we first superimposed them by subtracting the overall mean of the pattern from the oscillation frequency obtained in each stimulus condition (Fig. 2a, inset). Next, we compared the variability of the resulting oscillation frequencies across the stimulus conditions to the variability of responses to the same stimulus condition recorded in different blocks (Fig. 3). In the former case, the standard deviation was on average 3.73 times higher than in the latter. This ratio reduced to 1.89 for condition-shuffled data (crosses in Fig. 3; $P = 0.008$, Wilcoxon signed-rank test). This result

Fig. 2

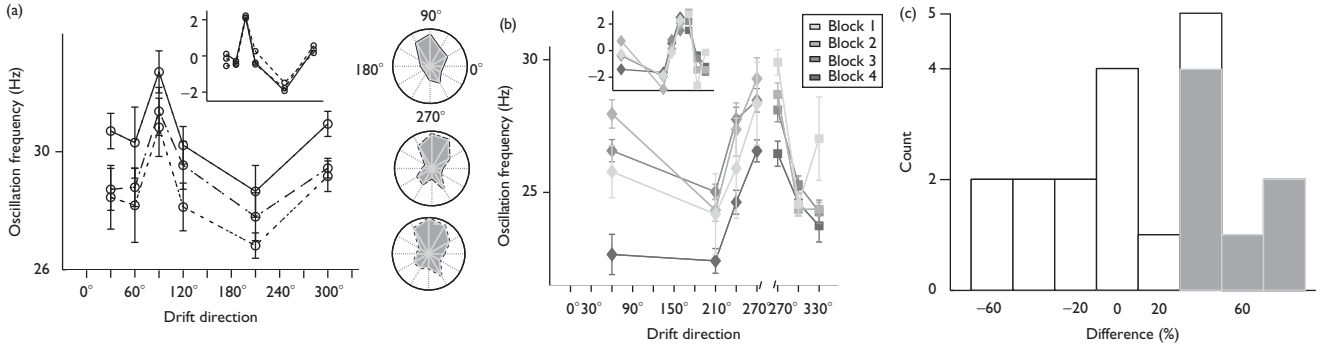

Example changes in oscillation frequencies for three neurons as a function of grating orientation and recording blocks. (a) Oscillation frequencies of one neuron obtained in six stimulation conditions, and in three recording blocks with a total time span of approximately 3 h. Inset: data superimposed by centring the means of the *y*-axis. Axis labels are the same as in the main figure. Right: orientation tuning determined by the firing rates with which the neuron responded to the same set of stimuli, shown separately for all three blocks. (b) Another example of two neurons (diamonds and squares) recorded in the same session, with the total time span across the four recording blocks of 21.6 h. Error bars: standard error of the estimate. Inset: the same as in (a). (c) Chance level vs. observed number of recordings in which maximum rate coincides with maximum oscillation frequency, shown for all 19 neurons. *X*-axis: the difference between the observed percent agreements and that expected by chance. Grey: the seven neurons for which the observed percent agreement was 100%.

Fig. 3

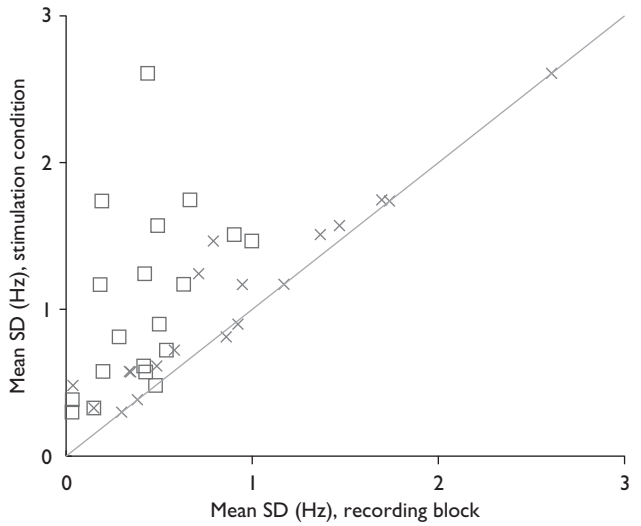

The mean variability of oscillation frequencies across different recording blocks compared to the variability across stimulus conditions, expressed as standard deviation (SD). Squares: original data. Crosses: condition-shuffled control data. Diagonal: identity line.

indicates that, over different recording blocks, the relative relationships within the patterns stayed constant despite the shifts of the mean oscillation frequencies.

Finally, the stability of the patterns was tested also by ranking stimulus directions according to the induced oscillation frequency, and comparing the ranks across recording blocks. For 10 out of 19 neurons (53%), the ranks of stimulus directions stayed identical. The probability of obtaining this result by chance is less than 0.001 (see Materials and methods section). For two neurons, more than 2/3 of the tracked stimulus directions stayed in the same relative rank across all blocks. For one, all stimulus directions stayed in the same relative rank across more than 3/4 of the tracked blocks. These levels of temporal stability were unlikely to be obtained by chance (in all cases, $P < 0.05$; computed from all possible combinations of ranks). Thus, in total, the ranks of 13 neurons (72%) could be considered stable across the recording blocks.

Discussion

In this study we investigated the modulation of oscillation frequency both as a function of stimulus properties and states. To achieve this goal, we had to overcome two difficulties: all investigated neurons had to be clearly identifiable by spike sorting and the neurons had to maintain sufficiently high spike counts across all recordings. We succeeded in collecting a sample of 19 neurons (i.e. single units), which was sufficiently large to obtain statistically significant results.

We found that in many neurons the frequency of induced oscillations increased with increasing discharge rate of light evoked responses. Hence, in some neurons, oscillation frequency reflects, in a similar way as response amplitude, the match between the cells' preferences for stimulus orientation and the direction of motion of the presented stimulus. At present, it is unclear whether this tuning of oscillation frequency is a result of the individual properties of a neuron, example of the resonant properties of its membrane [17,18] and the modulation of resonance by neuromodulators [19], or whether it is a network effect [20,21]. The coherence of the input may play a role too [22]. In any case, our data indicate that oscillation frequencies of individual neurons or groups of neurons with similar response preference must be

adjustable selectively. Considering that a drifting grating activates large volumes of cortical tissue containing both optimally and sub-optimally stimulated neurons, this predicts a dispersion of phases, the optimally stimulated population oscillating at higher frequencies than the less activated populations. As recordings suggest that drifting gratings induce global oscillations that are synchronized on average with zero phase delay across visual cortex [23,24], one expects the discharges of optimally activated cells to exhibit changes in the firing times relative to the global oscillatory rhythm or at least relative for less optimally stimulated cells. This cell-specific adjustment of oscillation frequency on top of a global oscillatory patterning of activity resembles closely, and may be related to the recently discovered mechanism underlying the phenomenon of phase precession in the hippocampus [25]. Whether these time delays are used for the encoding of visual information, as is likely the case for the encoding of spatial information in the hippocampus, is presently unknown. The present results suggest that future investigations should take into account also the oscillations frequencies of individual neurons. Interestingly, the adjustments in the frequency of oscillations may be only a property of mature brains because stimulus-induced changes could be found only in adult cats, as used in our experiment, but not in kittens, as reported elsewhere [11].

The finding that the overall oscillation frequency can change over time, as a state variable, and yet the tuning remains stable, has implications for models of beta/gamma oscillations [12]. Future models should allow for both types of changes – the state-dependent and the stimulus-dependent ones. Hence, our findings emphasize the point that the dynamical changes in the frequencies of oscillatory rhythms are important for the understanding of brain dynamics – a variable that has apparently not received the due attention until now.

Conclusion

The oscillation frequency with which neurons respond to drifting sinusoidal gratings is not constant but changes as a function of stimulus direction. More optimal stimuli have a tendency to induce higher oscillation frequencies, that is, the firing rate tuning of neurons is mirrored by the tuning of their oscillation frequencies. Moreover, under anesthesia, the average oscillation frequency changes over time. These changes in the baseline frequency do not affect the tuning properties of the responses.

Acknowledgements

This study is supported by a DFG grant number NI 708/2-1. In addition, support came from the Hertie Foundation, and the German Federal Ministry of Education and Research (BMBF) within the 'Bernstein Focus: Neurotechnology' through research grant 01GQ0840.

References

1 Gray CM, Singer W. Stimulus-specific neuronal oscillations in orientation columns of cat visual cortex. *Proc Natl Acad Sci U S A* 1989; **86**: 1698–1702.
2 Jagadeesh B, Gray C, Ferster D. Visually evoked oscillations of membrane potential in cells of cat visual cortex. *Science* 1992; **257**:552–554.
3 Herculano-Houzel S, Munk M, Neuenschwander S, Singer W. Precisely synchronized oscillatory firing patterns require electroencephalographic activation. *J Neurosci* 1999; **19**:3992–4010.
4 Chabli A, Guitton D, Fortin S, Molotchnikoff S. Cross-correlated and oscillatory visual responses of superficial-layer and tecto-reticular neurons in cat superior colliculus. *Exp Brain Res* 2000; **131**:44–56.
5 Traub D, Bibbig A, LeBeau F, Buhl E, Whittington M. Cellular mechanisms of neuronal population oscillations in the hippocampus in vitro. *Annu Rev Neurosci* 2004; **27**:247–278.
6 Gray C, Viana Di Prisco G. Stimulus-dependent neuronal oscillations and local synchronization in striate cortex of the alert cat. *J Neurosci* 1997; **17**:3239–3253.
7 Sannita WG. Stimulus-specific oscillatory responses of the brain: a time/frequency-related coding process. *Clin Neurophysiol* 2000; **111**:565–583.
8 Buzsáki G, Draguhn A. Neuronal oscillations in cortical networks. *Science* 2004; **304**:1926–1929.
9 Tallon-Baudry C. The roles of gamma-band oscillatory synchrony in human visual cognition. *Front Biosci* 2009; **14**:321–332.
10 Gieselmann M, Thiele A. Comparison of spatial integration and surround suppression characteristics in spiking activity and the local field potential in macaque V1. *Eur J Neurosci* 2008; **28**:447–459.
11 Bringuier V, Frégnac Y, Baranyi A, Debanne D, Shulz D. Synaptic origin and stimulus dependency of neuronal oscillatory activity in the primary visual cortex of the cat. *J Physiol* 1997; **500**:751–774.
12 Nikolić D. Model this! Seven empirical phenomena missing in the models of cortical oscillatory dynamics. Proceedings of the International Joint Conference on Neural Networks (in press) 2009.
13 Biederlack J, Castelo-Branco M, Neuenschwander S, Wheeler DW, Singer W, Nikolić D. Brightness induction: rate enhancement and neuronal synchronization as complementary codes. *Neuron* 2006; **52**:1073–1083.
14 König P. A method for the quantification of synchrony and oscillatory properties of neuronal activity. *J Neurosci Methods* 1994; **54**:31–37.
15 Muresan RC, Jurjuþ O, Moca V, Singer W, Nikolić D. The oscillation score: an efficient method for estimating oscillation strength in neuronal activity. *J Neurophysiol* 2008; **99**:1333–1353.
16 Efron B, Tibshirani R. Bootstrap methods for standard errors, confidence intervals, and other measures of statistical accuracy. *Statist Sci* 1986; **1**:54–75.
17 Maex R, De Schutter E. Resonant synchronization in heterogeneous networks of inhibitory neurons. *J Neurosci* 2003; **23**:10503–10514.
18 Tohidi V, Nadim F. Membrane resonance in bursting pacemaker neurons of an oscillatory network is correlated with network frequency. *J Neurosci* 2009; **29**:6427–6435.
19 Ito H, Schuman E. Frequency-dependent signal transmission and modulation by neuromodulators. *Front Neurosci* 2008; **2**:138–144.
20 Brunel N, Wang X. What determines the frequency of fast network oscillations with irregular neural discharges? I. Synaptic dynamics and excitation-inhibition balance. *J Neurophysiol* 2003; **90**:415–430.
21 Whittington MA, Traub RD, Kopell N, Ermentrout B, Buhl EH. Inhibition-based rhythms: experimental and mathematical observations on network dynamics. *Int J Psychophysiol* 2000; **38**:315–336.
22 Burwick T. Temporal coding: assembly formation through constructive interference. *Neural Comput* 2008; **20**:1796–1820.
23 Nikolić D. Non-parametric detection of temporal order across pairwise measurements of time delays. *J Comput Neurosci* 2007; **22**:5–19.
24 Schneider G, Havenith M, Nikolić D. Spatio-temporal structure in large neuronal networks detected from cross-correlation. *Neural Comput* 2006; **18**:2387–2413.
25 Harvey C, Collman F, Dombeck D, Tank D. Intracellular dynamics of hippocampal place cells during virtual navigation. *Nature* 2009; **461**:941–946.

Chapter 3 - Scaled correlation analysis, a better way to compute a cross-correlogram.

EJN fens EUROPEAN JOURNAL OF NEUROSCIENCE

European Journal of Neuroscience, pp. 1–21, 2012 doi:10.1111/j.1460-9568.2011.07987.x

Scaled correlation analysis: a better way to compute a cross-correlogram

Danko Nikolić,[1,2] Raul C. Mureşan,[1,3] Weijia Feng[1,2] and Wolf Singer[1,2]
[1]Max Planck Institute for Brain Research, Frankfurt am Main, Germany
[2]Frankfurt Institute for Advanced Studies, Johann Wolfgang Goethe-University, Frankfurt am Main, Germany
[3]Center for Cognitive and Neural Studies, Romanian Institute of Science and Technology, Cluj-Napoca, Romania

Keywords: auto-correlation, cat, cross-correlation, oscillation, rate co-variation, synchrony

Abstract

When computing a cross-correlation histogram, slower signal components can hinder the detection of faster components, which are often in the research focus. For example, precise neuronal synchronization often co-occurs with slow co-variation in neuronal rate responses. Here we present a method – dubbed scaled correlation analysis – that enables the isolation of the cross-correlation histogram of fast signal components. The method computes correlations only on small temporal scales (i.e. on short segments of signals such as 25 ms), resulting in the removal of correlation components slower than those defined by the scale. Scaled correlation analysis has several advantages over traditional filtering approaches based on computations in the frequency domain. Among its other applications, as we show on data from cat visual cortex, the method can assist the studies of precise neuronal synchronization.

Introduction

A common problem with the use of the cross-correlation histogram (CCH) is the presence of correlated signal components that occur with a slower time course than those of interest. For example, when precise neuronal synchrony is investigated, a component with a 25 ms time scale (e.g. 40 Hz gamma oscillation) may be considered interesting, whereas a component with a 100 ms time scale or larger (≤ 10 Hz) – here referred to as rate co-variation – would normally be considered uninteresting. Rate co-variation, also known as noise correlation (Averbeck *et al.*, 2006), can impair the study of precise neuronal synchrony by modulating the size of the center peak in the CCH (Brody, 1999). Center peaks produced by rate co-variation are broader than those produced by neuronal synchrony but, nevertheless, the two processes are often difficult to dissociate. In particular, rate co-variation becomes a problem when it co-exists with synchrony (Staude *et al.*, 2008). For example, if changes in the strength of synchronization (such as those induced by stimulus properties, e.g. Gray *et al.*, 1989; Biederlack *et al.*, 2006) are investigated, in a case of peak superposition, it is difficult to tell whether a change in the size of the peak is due to changes in the strength of synchronization or, alternatively, due to a change in the strength of rate co-variation. Thus, for the analyses based on CCHs, it is an advantage if slow rate co-variation can be separated efficiently from the faster neuronal synchronization.

The most widely used method for this purpose is the so-called shift predictor (SP) (or shuffle predictor) (Gerstein & Perkel, 1972; Gray & Singer, 1989; Munk *et al.*, 1995; Nowak *et al.*, 1999). A SP is a CCH computed between pairs of signals recorded at different times (i.e. from different experimental trials and in response to the same stimulus). The assumption underlying the SP is that the slow temporal dynamics of rate co-variation does not change across repeated trials (i.e. the dynamics is time-locked to the stimulus onset) and, thus, the SP reveals this stimulus-evoked correlation in a center peak. In contrast, precise neuronal synchrony vanishes from a SP, as these correlations are usually generated by internally-timed processes not locked to the stimulus onset. The contribution of neuronal synchrony can then be isolated by simply subtracting from the standard CCH the stimulus-locked component estimated by the SP (Gerstein & Perkel, 1972).

Unfortunately, SPs do not provide a complete account for rate co-variations. Changes in neuronal firing rates are not always stimulus-locked across repeated trials and every deviation from such regularity results in an underestimation of the magnitude of rate co-variation (e.g. Brody, 1999). Example sources of rate co-variations that lack time-locking to the stimulus are changes in firing rates, which can occur due to fluctuations of attention, eye movements, spontaneous changes in the cortical states or non-stimulus-locked oscillatory rhythms slower than those supporting precise neuronal synchronization. Another problem with SPs is that, in some experimental designs, repeated trials do not exist and, thus, it is not even possible to define a SP, as is the case for example in the analyses of spontaneous neuronal activity (Beggs & Plenz, 2003; Ikegaya *et al.*, 2004; Hahn *et al.*, 2010). Therefore, methods better than SPs are needed to separate rate co-variation from precise neuronal synchrony. Such methods already exist for estimating the significance of joint spike events detected across a larger number of neurons (Grün *et al.*, 2002; Pipa *et al.*,

Correspondence: Danko Nikolić, [1]Max Planck Institute for Brain Research, as above.
E-mail: danko.nikolic@gmail.com

Received 4 October 2008, revised 8 October 2011, accepted 5 December 2011

2008). Also, the methods based on coherence can estimate the strength of synchrony between pairs of spike trains for a given frequency range (Fries *et al.*, 1997; Pesaran *et al.*, 2002). However, these methods cannot be used to construct CCHs as they either do not provide a means for removing the contributions of the slow components or, if they do, as we will show, they alter the spike trains such that the original relationships between the signals cannot be reconstructed accurately. The present work proposes a method that is designed for use with CCHs and auto-correlation histograms, dubbed scaled correlation analysis (SCA). The method attenuates the contributions of the slow component of a CCH (e.g. slow rate co-variation) and reveals the cross-correlation for the fast components of the signals (e.g. strength of precise neuronal synchronization).

Materials and methods

The experimental methods and setup were similar to those reported in several other studies (Biederlack *et al.*, 2006; Nikolić, 2007; Schneider & Nikolić, 2006; Schneider *et al.*, 2006; Nikolić *et al.*, 2009). Here, we report the methods in a shorter form.

Preparation and recordings

In two cats, anesthesia was induced with ketamine (0.2 ml/kg, 5% diluted) and, following the tracheotomy, was maintained with a mixture of 70% N_2O and 30% O_2 and with halothane (0.6%). To prevent eye movements, two cats were paralysed with pancuronium bromide applied intravenously (Pancuronium, Organon, 0.15 mg/kg/h). After the completion of the experiment, the animal was killed by a 3 ml dose of Narcoren (pentobarbital) applied intravenously. All of the experiments were conducted according to the guidelines of the Society for Neuroscience and German law for the protection of animals, approved by the local government's ethical committee and overseen by a veterinarian.

On each of the 16 channels, neuronal activity was recorded extracellularly from multiple neurons (multi-unit activity) by using a silicon-based probe (channels organized in a 4×4 spatial matrix) supplied by the Center for Neural Communication Technology at the University of Michigan. The probe had minimal intercontact distances of 200 μm (0.3–0.5 mega Ohm impedance at 1000 Hz). Electroencephalogram signals were recorded with intracranial silver-ball electrodes placed above the visual cortex. Signals were amplified 1000×, filtered between 500 Hz and 3.5 kHz, and digitized with 32 kHz sampling frequency. The probe was inserted into the cortex approximately perpendicular to the surface, which allowed recording simultaneously from neurons at different depths and with different orientation preferences. In one cat we used nine multi-unit activity signals recorded simultaneously that responded well to visual stimuli and had orientation selectivity that was appropriate for eliciting large responses with the presently used stimuli. All of the receptive fields were overlapping and were thus all stimulated simultaneously by a single stimulus.

Visual stimulation

Stimuli were presented on a 21 inch computer monitor (Hitachi CM813ET) with 100 Hz refresh rate. The software for visual stimulation was the stimulation tool, ActiveSTIM (http://www.ActiveSTIM.com). The stimuli were presented binocularly and the eyes were fused by mapping the borders of the respective receptive fields and then aligning the optical axes of the eyes with an adjustable prism placed in front of one eye. The orientation preferences of the multi-units used in the present analysis were determined by sinusoidal gratings drifting in 12 different directions. Responses were analysed to stimuli that consisted of a single moving bar (Figs 7C and H, and 8A), grating stimuli with either sinusoidal (Figs 7A and F, and 8B–E) or rectangular luminance profiles (Fig. 7D and I), or plaid stimuli constructed by overlapping two rectangular gratings (Fig. 7E and J). With the exception of the single-trial analysis in Fig. 8F, the responses for 20 stimulus presentations were averaged, each in a duration of 2–5 s. To create CCHs smoother than those obtained by 20 stimulus presentations, in several plots we averaged responses to several different stimulation conditions (Fig. 7A, B, F and G). The orientation and speed of all presented stimuli were optimal for eliciting large rate responses.

Artificial continuous signals

To generate artificial continuous signals (i.e. in which samples can take any real value), we used combinations of sinusoid modulated components and high-frequency noise. We first generated two perfect sinusoidal signals, one having a low (ω_{SLOW}) and the other a high (ω_{FAST}) frequency, and constructed the reference signal as a sum of these two components, as follows

$$S_{SLOW}(t) = a_{SLOW} \cdot \sin(\omega_{SLOW} \cdot t) \quad (1)$$

$$S_{FAST}(t) = a_{FAST} \cdot \sin(\omega_{FAST} \cdot t) \quad (2)$$

$$A_t = S_{SLOW}(t) + S_{FAST}(t) \quad (3)$$

where t is time, a_{SLOW} and a_{FAST} are the amplitudes of the slow and fast component, respectively, and ω_{SLOW} and ω_{FAST} are the (angular) frequencies of the slow and fast component, respectively.

The target signal was generated by mixing S_{SLOW} and S_{FAST} with noise, such as to obtain correlated versions of slow and fast components, which were then subsequently summed

$$B(t) = r_{SLOW} \cdot S_{SLOW}(t) + \sqrt{1 - r_{SLOW}{}^2} \cdot y(t) + r_{FAST} \cdot S_{FAST}(t) + \sqrt{1 - r_{FAST}{}^2} \cdot z(t) \quad (4)$$

where r_{SLOW} and r_{FAST} are the correlations of the slow and fast components, respectively, and $y(t)$ and $z(t)$ are noise signals drawn from uniform distributions with zero mean and amplitudes equal to $1.25 \times$ the amplitude of their respective sinusoidal components, S_{SLOW} and S_{FAST}. When the amplitudes of the slow and fast components were scaled, the amplitude of the noise functions was also scaled accordingly.

Artificial binary signals

To generate artificial binary signals (i.e. values 1 or 0), we used non-homogeneous Poisson processes, in which the likelihood of firing a spike in a 1 ms bin, M, was given by a scaled sum of sinusoidal probability functions, as follows

$$P(t) = \max[(a_{SLOW} \cdot \sin(\omega_{SLOW} \cdot t) + a_{FAST} \cdot \sin(\omega_{FAST} \cdot t)), 0] \quad (5)$$

$$R = \frac{\text{desired\_rate}}{\int P(t)} \cdot \frac{1}{1000} \quad (6)$$

$$M(t) = R \cdot P(t) \quad (7)$$

where P is the unnormalized probability function, t is time, a_{SLOW} and a_{FAST} are the amplitudes of the slow and fast component probability

functions, respectively, ω_{SLOW} and ω_{FAST} are the (angular) frequencies of the slow and fast component, respectively, R is a scaling factor that sets the desired average firing rate, and M is the actual probability function used to generate spikes.

The probability function $P(t)$ was a rectified sum of sinusoids, i.e. when the sum was negative it was rectified to 0. Desired firing rates were obtained by computing the integral of P and deriving a scaling factor R of the firing probability function M (see Eqns 6 and 7). At each moment in time, t, a spike was produced if an independent draw from a uniform random distribution in the range [0…1] yielded a value $\leq M(t)$. In previous studies (Moca *et al.*, 2008; Schneider & Nikolić, 2008; Havenith *et al.*, 2011) it was demonstrated that non-homogeneous Poisson processes produce artificial CCHs with properties similar to those of real CCHs.

Results

We first introduce the algorithm for the computation of SCA, and then the results of its applications on simulated data with known correlation properties. Next, SCA is applied to real neurophysiological data recorded from the cat visual cortex. Finally, we compare SCA with other techniques designed for the estimations of synchrony and that are based on cross-spectrum and coherence.

Computation of scaled correlation and its principles of operation

Correlations in restricted sampling ranges

The mechanism underlying the removal of slow components in SCA relies on the reduction of the correlations that emerge from the slow components while retaining the correlations of the fast components. This is achieved through restrictions in the sampling range of the original data. One characteristic of correlation measures, such as Pearson's r, is that any reduction in the variability of a sample relative to the variability in the population affects the measured strength of correlation. Depending on the structure of the data set, the estimate may either decrease or increase relative to the one with full variability, including even the possibility that the correlation changes its sign (Alexander *et al.*, 1984; Millsap, 1989; Held & Foley, 1994; Aguinis & Whitehead, 1997; Raju & Brand, 2003). In Fig. 1A we show an example scatter plot in which two restricted samples (created by dividing the scatter into two unequal halves by the vertical dashed line) exhibit much smaller variability than the entire sample. Importantly, the correlations in the sub-samples are reduced relative to that in the entire sample. In Fig. 1B we show an example of two continuous signals (i.e. data sets with temporal structure), which are more relevant for the present purposes. The slow components of these two signals are negatively correlated (when one increases, the other decreases) but, as indicated by the zoom-in, the fast components can, at the same time, be positively correlated (concomitant increases and decreases). Scaled correlation can be used to focus the analysis on this fast component. Correlations between continuous signals can also be shown in a scatter-plot-like diagram, known as a phase diagram. An example for another pair of continuous signals is shown in Fig. 1C. Here the time flows along the line. In this plot, a restriction in the sampling range is made by cutting out segments of data along the time axis, which is illustrated by the alternate blue and red colors. Although the overall plot indicates a negative correlation (it is oriented from top-left to bottom-right), the segments are predominantly correlated positively (oriented bottom-left to top-right). In binary data (i.e. neuronal spiking activity), restriction of the sampling range can also alter correlations, as illustrated in Fig. 1D. Although the entire

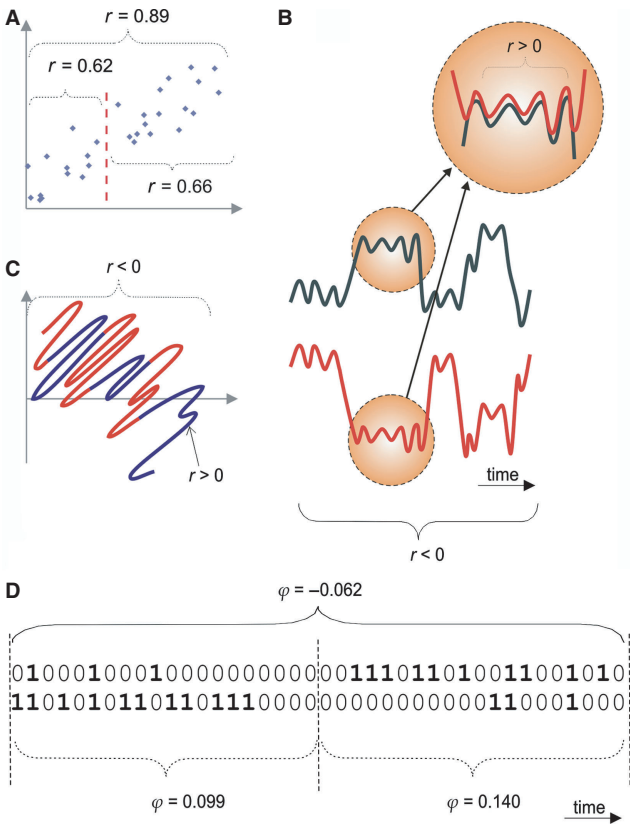

FIG. 1. Effects of restricted sampling on coefficients of correlation. (A) An illustration of how a reduction in sample variance can decrease the measured correlation in a scatter plot. Here, the sample variance is reduced by setting a threshold on the x-axis (red dashed line). (B) An example of restricted sampling by selecting only a sub-segment of continuous signals. The correlation is negative for the entire segment and the correlation is positive for the sub-segment. (C) An example similar to B but shown as a phase plot. In case of LFPs, the two axes would indicate voltage, whereas time flows along the line. The entire data set exhibits a negative correlation, whereas the sub-segments (alternating red and blue colors) have predominantly positive correlations. (D) Segmentation of binary processes (e.g. neural spiking events) works in the same way. It can also reduce variability and hence produce changes in correlation strength. For interpretation of color references in figure legend, please refer to the Web version of this article.

segment exhibits a negative correlation, both sub-segments exhibit positive correlations. Similar segmentation processes are the basis for the computation of SCA, as explained next.

The algorithm for computing scaled correlation analysis

To remove slow components, scaled correlation does not apply filtering of signals prior to the computation of correlation. Rather, scaled correlation can be understood as an algorithm that filters correlations directly by the means of restricted sampling, allowing only the correlations that occur at a given time scale or smaller to enter the calculation. Usually, restricted sampling is considered undesirable and has been studied in the context of estimating a correction that recovers the original correlation of the non-restricted sample (e.g. Alexander *et al.*, 1984; Millsap, 1989; Held & Foley, 1994; Aguinis & Whitehead, 1997; Raju & Brand, 2003). Scaled correlation, in contrast, takes advantage of restricted sampling, creating it intentionally in a controlled manner in order to estimate the correlations only for a sub-set of time scales.

To compute scaled correlation for the central bin in the CCH (i.e. without phase offset between the signals), the signals are cut into a

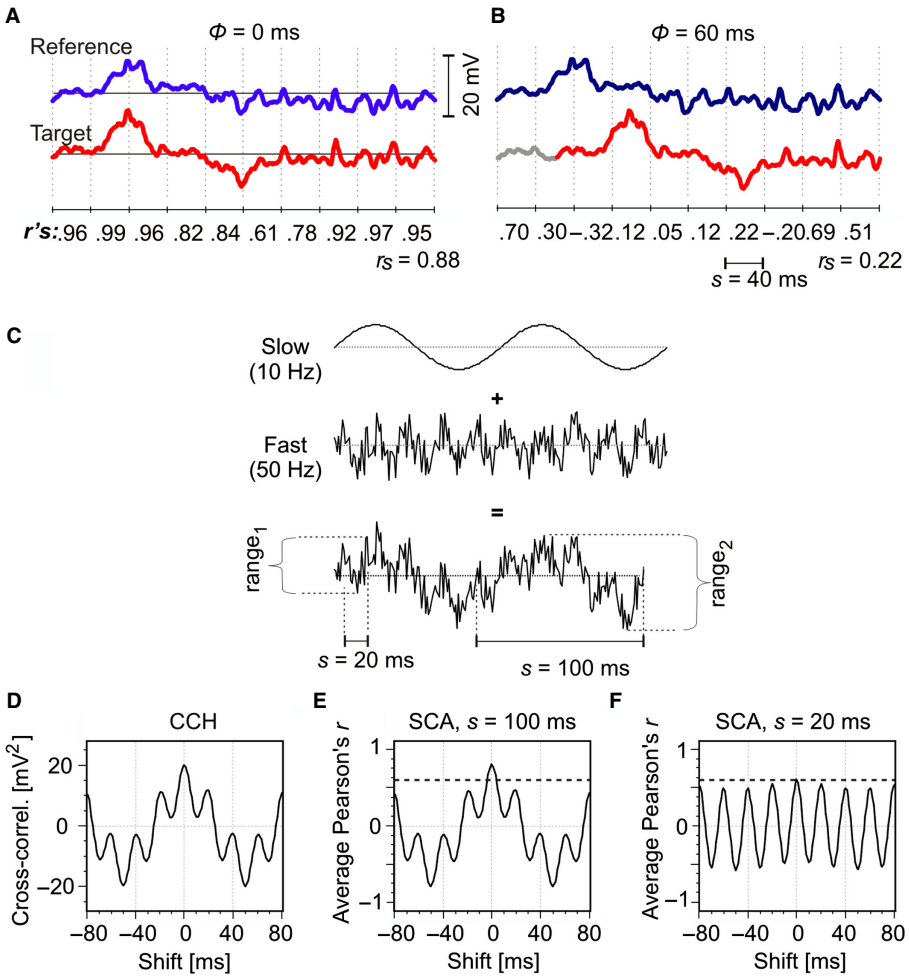

FIG. 2. Computation of SCA. (A) An illustration made on LFP signals recorded from two electrodes simultaneously. Signals are segmented into small pieces of length s (here, s = 40 ms). For each segment, a normalized measure of correlation is computed, r, and the values are averaged over longer stretches of the signal, resulting in $\bar{r}_s$. (B) To compute a complete CCH with all time shifts, φ, the segmentation must always be applied anew after each shift. (C) For simulations in D–F and in Figs 3 and 4, each signal is composed by the addition of two continuous components: a regular slow one and a noisy fast one. The added noise always had high frequency (1 kHz). Hence, the fast components were correlated with $r < 1.0$, the actual correlation depending on the amplitude of noise. In contrast, the slow components were always correlated perfectly (r = 1.0). (D) A classical CCH computed for a pair of signals generated by the methods in C. Both slow and fast components are visible. (E) Scaled correlation with s larger than the period of the slow component produces a cross-correlation plot of identical shape to the classical CCH. (F) When the scale is reduced to the period of the fast component, the contribution of the slow component to the CCH is removed and the correlation properties of the fast component are revealed much more accurately. The horizontal dashed line indicates the correlation inserted into the fast components, which should be recovered by the analysis.

series of adjacent segments of length s, and then coefficients of correlation are computed for each segment (Fig. 2A, left). The correlation coefficients are subsequently averaged across all segments in a trial, and these results are averaged next over repeated experimental trials (if any). In the present study, all of the averaging of correlations was made without Fisher's z-transformations of r-values (Fisher, 1915) (see a later Discussion and Appendices A and E on the pros and cons of using such transformations).

Thus, the scaled coefficient of correlation $\bar{r}_s$ at the scale s is given by

$$\bar{r}_s = \frac{1}{K}\sum_{k=1}^{K} r_k, \tag{8}$$

where r_k indicates the correlation computed for segment k, $k \in [1 \ldots K]$. K is the number of time segments that can be fit into the total length of the signal, T, without overlap between the segments, and is given by

$$K = \text{round}\left(\frac{T}{s}\right). \tag{9}$$

For example, for a total time period T = 2 s and segment size s = 25 ms (a value suitable for measuring synchrony supported by oscillations of 40 Hz or higher), the total time period will be divided into $K = 2000/25 = 80$ segments, and for each segment another value of r will be computed (later we also discuss cases in which some segments are skipped due to missing data). The duration of the segment is denoted as the scale of the analysis. Correlation coefficients other than r may also be used (e.g. Spearman's rho described in Appendix B).

As in the regular CCH, the above calculation also needs to be repeated for all necessary time shifts, φ, between the reference and the target. To obtain proper estimates of correlation for all possible shifts, it is necessary to segment the signals only after the target signal is shifted (as indicated in Fig. 2B). These repeated segmentation processes, i.e. following each shift, allow a scaled CCH to be computed legitimately for shifts that are larger than the scale of the

analysis, i.e. $\varphi > s$, which is the case for most of the CCHs shown in the present study (e.g. shifts of ± 80 ms with s = 30 ms). The final CCH is constructed simply by plotting $\bar{r}_s$ as a function of the time offset, φ (e.g. ± 80 ms in steps of 1 ms).

The chosen duration of the segments, s, is thus central to the present analyses as it determines the time scales of the signal components that will be preserved (the components with time scale ≤ s) or removed (those of the time scale > s). The segmentation process reduces the variance only for the slow components, whereas the fast components remain to be sampled with their full variance. This is illustrated in Fig. 2C, where the variability (vertical dispersion) of a composite signal is smaller within a 20 ms than within a 100 ms window ($\text{range}_1 < \text{range}_2$). See also the proof in Appendix C.

Mathematically identical cross-correlation functions are used to compute the correlogram for binary signals (e.g. action potentials) and continuous signals [e.g. local-field potentials (LFPs)] or for a combination of the two. However, traditionally, in statistics the correlations for each signal type (or their combination) have different names. For the pairs of binary signals, the measure is known as the phi coefficient of correlation and for the combination of binary and continuous signals, it is known as the point-biserial coefficient of correlation. Details on how Pearson's r can be calculated most speed-efficiently for various types of signals are given in Appendix B, which also provides information on how to access freely Matlab and C++ libraries for the calculation of SCA.

Example calculation of scaled correlation analysis

Example applications of SCA to simulated continuous signals are shown in Fig. 2C–F. Each of the signals in a correlated pair consisted of two oscillatory components, one component having a fast and the other a slow oscillatory rhythm (Fig. 2C) (usually, 5× ratio in oscillation frequencies). The examples in Fig. 2D–F were calculated with the maximal possible correlation between the corresponding slow components, r = 1.0, and a medium-range correlation between the corresponding fast components, r = 0.6.

The goal of the analysis was to accurately extract the correlation of the fast components and to remove, as much as possible, the contributions of the slow components. This was obviously not possible by computing a CCH without the use of scaled correlation (referred to here as classical CCH), as the resulting CCH was reflecting the superposition of the slow and fast components (Fig. 2D). A similar result was obtained when SCA was computed with a large scale that corresponded to the time scale (i.e. oscillation period) of the slow components (s = 100 ms) (Fig. 2E). In this case, the strength of correlation for the fast component at the zero phase offset was overestimated (r = ∼0.80 instead of 0.60) and the shape of the correlogram was the same as in the classical CCH (as in Fig. 2D), reflecting large contributions of the slow components. However, when the scale was shortened to the size that matched the time constant of the fast components (s = 20 ms), the contribution of the slow component was almost entirely eliminated despite its large correlation, and the shape of the resulting CCH was dominated by the fast components (Fig. 2F). The correlation estimated at the center peak (r = 0.5996) was very close to its true value. This illustrates that SCA with the scale larger than the time constants of signal components produces a correlogram of a shape identical to a classical CCH, whereas a decrease in the scale changes the shape to reflect the fast components.

How does scaled correlation analysis relate to a normalization of a cross-correlation histogram?

The absolute values on the y-axis depend on the voltages measured by field potentials or, in the case of spiking signals, on the firing rates of neurons. Hence, for comparisons, such CCHs often need to be normalized by various methods, which may involve fitting a Gabor function (König, 1994), or a computation of Pearson's r between spike trains (e.g. Lamme & Spekreijse, 1998). In the latter case, a single correlation coefficient is computed for the entire length of the analyzed signals, multiple r's being averaged only between repeated trials. Hence, this form of normalized CCH corresponds to scaled correlation with s equal to the length of the trial. As shown in Fig. 2D and E, given that s is equal to the total length of the signal, SCA returns a CCH of the shape that is identical to the classical CCH (proof provided as a part of Appendix D). Normalizations based on non-segmented data do not remove the slow components. They act only as scaling factors for the y-axis of the CCH. To remove a slow component from correlation it is necessary to use segments smaller than the period of that component. In that way, the correlation at each segment is normalized prior to the averaging.

Mathematical theory of scaled correlation

In Appendix E we provide a proof that, if all segments have identical means and variances, the average Pearson's correlation obtained with small s is identical to the value of the single correlation coefficient computed across the entire signal (i.e. with maximum segment size, s). This result justifies the averaging procedure in Eqn 8. Note also that this identity does not hold if Fisher's z-transformation is applied to the averaging process.

In Appendix D, we show analytically that scaled correlation removes the contribution of the slow components by estimating its contribution through a form of low-pass filtering and subtracting it from the total correlation. In effect, scaled correlation produces implicit low-pass filtering that is similar to a moving average filter.

Analysis of simulated signals

Pairs of continuous signals

By using simulations similar to those shown in Fig. 2C–F, we investigated systematically the importance of, and the dependencies between, the following three factors: (i) the segment size, s, (ii) the ratio between the amplitudes of the fast and the slow components, and (iii) the ratio of the oscillation frequencies of the two components.

To investigate the application on continuous signals we used both signals with a single oscillatory component (Fig. 3A and B) and signals composed of two oscillatory components (Fig. 3C–E). The composed signals were generated as illustrated in Fig. 2C (see also Materials and methods). Each data point in Fig. 3A–E is calculated on a 5 s simulated signal and, to focus the analysis on the magnitudes of correlations, only the values of the center peaks of scaled CCHs (i.e. φ = 0) are shown in these plots. In addition, representative complete CCHs are shown in Fig. 3F–J.

Single component. The relationship between segment size and measured strength of correlation was investigated for two different oscillation frequencies of a single oscillatory component (50 and 10 Hz) and four levels of correlation strength (r = 0.2, 0.4, 0.6 and 0.8; color coded). In Fig. 3A and B it can be seen that the correlations were estimated correctly only if the segment sizes were equal to or larger than the period of the oscillatory rhythm (dashed vertical lines). If the segment sizes were smaller than that, the correlations were always reduced, the magnitude of the reduction depending on the degree of discrepancy between the period of the

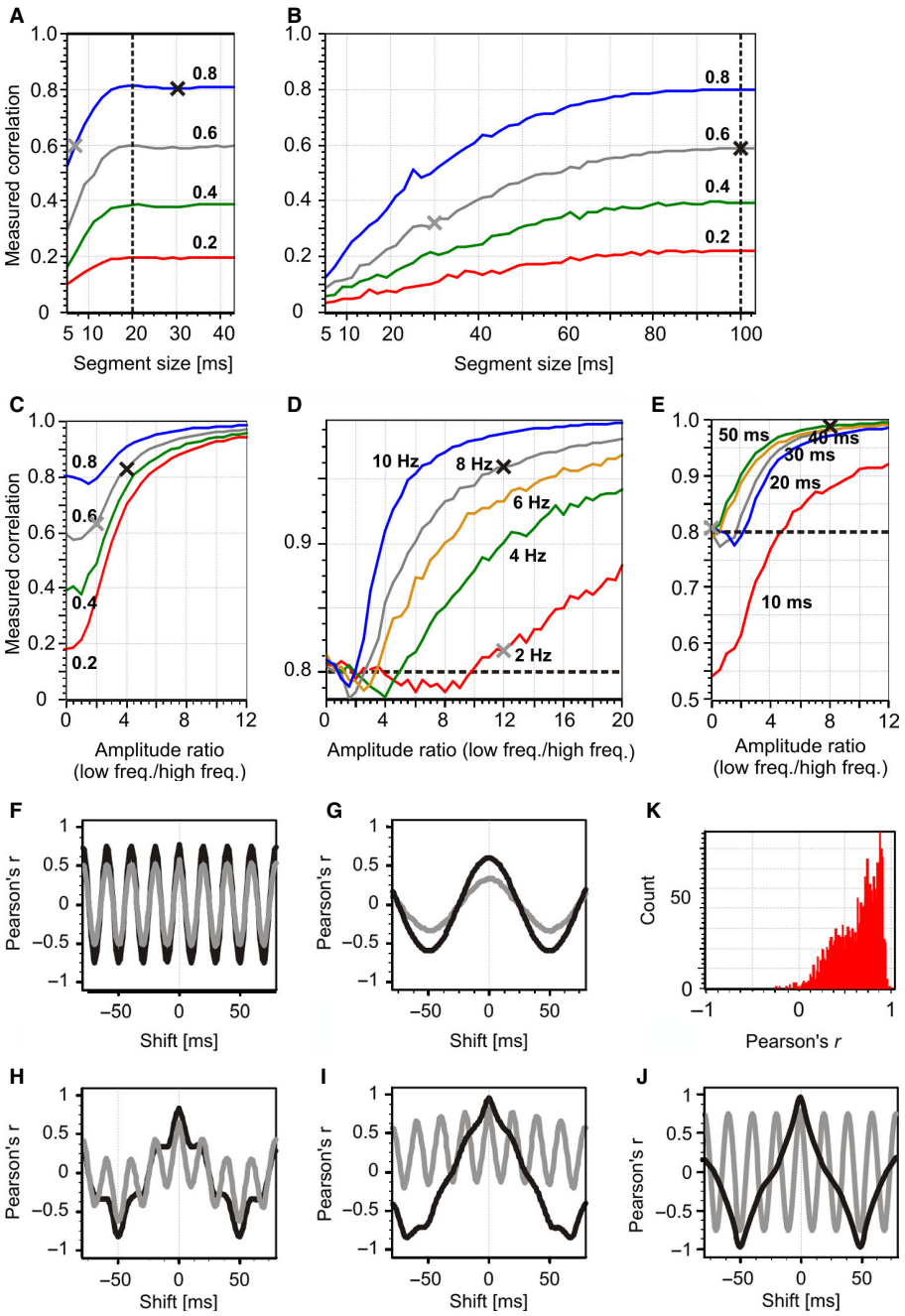

FIG. 3. Analysis of the degree to which SCA attenuates the contributions of slow components in simulated continuous signals. Signals have one oscillating component of either 50 Hz (A) or 10 Hz (B). The color code indicates the strength of correlation inserted into the signals (r = 0.2–0.8) and the vertical dashed line indicates the segment size that corresponds to the period of the oscillation cycle. (C–E) Signals with two oscillatory components composed as described in Fig. 2C. (C) The strength of correlation between high-frequency components (50 Hz) was manipulated (color coded), whereas the correlation between the slow components (10 Hz) was kept constant (r = 1.0) (s = 20 ms). (D) The frequency of the slow component was manipulated (color coded), whereas the correlation between fast components was kept constant (r = 0.8; dashed line) (s = 20 ms). (E) Scale size was manipulated (color coded), the correlations and frequencies of slow components being constant (r = 0.8 and f = 10 Hz, respectively). The crosses indicate data points for which cross-correlograms are shown in F–J. (F) CCHs for the data points in A. Gray, s = 7 ms; black, s = 30 ms. (G) CCHs for the data points in B. Gray, s = 30 ms; black, s = 100 ms. (H) CCHs for the data points in C. Gray, amplitude ratio = 2; black, amplitude ratio = 4. (I) CCHs for the data points in D. Gray, f(slow) = 2 Hz; black, f(slow) = 8 Hz. (J) CCHs for the data points in E. Gray, amplitude ratio = 0; black, amplitude ratio = 8. (K) Distribution of r-values across 250 segments of duration s = 20 ms used to calculate the center peak of the CCH in H (gray). For interpretation of color references in figure legend, please refer to the Web version of this article.

signal component and the segment size. Importantly, a small discrepancy between the scale and the signal period does not much affect the estimated correlation – a property of SCA that should be considered when choosing the segment size and when interpreting the results of an analysis.

Two components. Signals composed of two oscillatory components consisted of varying degrees of correlation (r_{FAST} = 0.2–0.8) for the fast component (50 Hz) and fixed correlation (r_{SLOW} = 1.0) for the varying frequencies of the slow component (2–10 Hz). A variable that strongly affected the measured correlation was the ratio between the

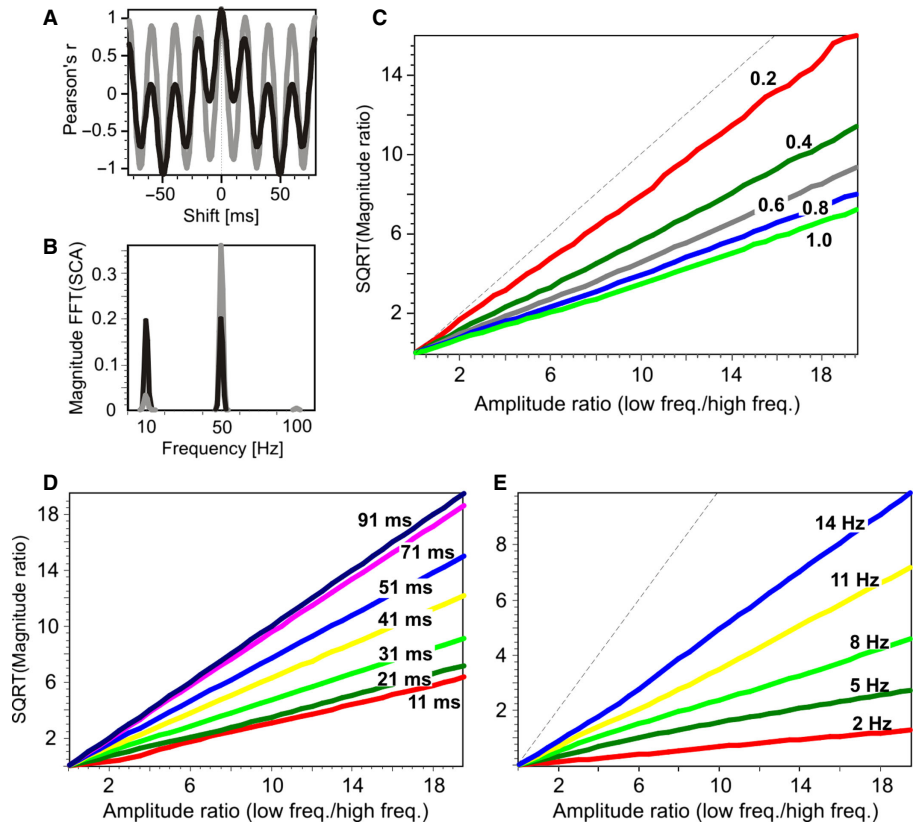

FIG. 4. Analysis of the magnitude spectrum of scaled cross-correlograms. (A) Scaled correlograms computed with long (black, s = 100 ms) and short (gray, s = 20 ms) scale for combined signals at 11 and 50 Hz of equal amplitude. (B) Magnitude of the FFT for the correlograms in A. (C) Square root (SQRT) of the ratio between peak sizes from B at 11 and 50 Hz, shown as a function of the ratio between the amplitudes of the slow and fast component (x-axis) and the strength of correlation between the fast components (color coded). (D) Instead of the correlation strength as in E, the sizes of the scale were manipulated (color coded). (E) Similar to C and D but the frequency of the slow component was manipulated (color coded). For interpretation of color references in figure legend, please refer to the Web version of this article.

amplitudes of the slow and fast components, and this is indicated on the x-axis of all plots. If not specified otherwise, the scale of the analysis was s = 20 ms.

The finding that the relative amplitude of components strongly determines the measured correlation is shown in Fig. 3C, where the frequency of the slow component was set to 10 Hz. SCA attenuated the slow components well when their amplitude was similar to that of the fast components. However, when the slow component had extremely large amplitudes (i.e. > ~4× larger), the measured correlation remained dominated by the slow components.

This result did not depend much on the true correlations between the fast components (Fig. 3C), each value of r being affected in a qualitatively similar way. However, the relative difference in the oscillation frequencies was an important variable (Fig. 3D). As this difference increased, increasingly larger differences in the amplitude could be absorbed by SCA and r_{FAST} could be estimated accurately. For example, 2 Hz components could have as much as 12× larger amplitude than that of 50 Hz components and still not prevent an accurate estimation of the correlation between the 50 Hz components (red curve in Fig. 3D).

Finally, the choice of the scale, s, affected the measured correlations between multi-component signals similarly to the single-component signals. To recover the original correlation between the fast components (r = 0.8), it was necessary that the scale was close to the oscillation period of that component (ideally, 20 ms for 50 Hz; Fig. 3E). However, the scale should not be much smaller, as it then also attenuates the correlation between the fast components (red line in Fig. 3E).

Representative examples of auto-correlograms and cross-correlograms are shown in Fig. 3F–J, which correspond to the data points marked with crosses in Fig. 3A–E, respectively. The choice of scale, s, does not affect the overall shape of the CCH when signals have only one component, but only the magnitudes of measured correlations are affected (Fig. 3F and G). In contrast, for multi-component signals the shapes of CCHs can change drastically as a function of scale. As the contributions of slow components to the measured r reduce with a decrease in s, so does their contribution to the shape of the correlogram (Fig. 3H–J).

Even when the average $\bar{r}_s$ is computed accurately it is a result of many r-values that can vary considerably across individual segments. For continuous signals, these distributions are also unimodal. An example distribution is shown in Fig. 3K, which has an average of 0.65 and corresponds to the center peak of the CCH in Fig. 3H (gray curve).

The contributions of slow and fast components to a CCH can be quantified by computing the fast Fourier transform (FFT) of a correlogram (here, this was done by computing correlograms for lags between ± 512 ms and considering the leftmost 1024 out of 1025 points for the FFT). For example, scaled correlograms applied to two-component signals with s = 100 and s = 20 ms in Fig. 4A (only parts of the correlograms are shown, spanning ± 80 ms); the magnitude spectrums are shown in Fig. 4B. With a long segmentation window, the magnitude of the fast and slow component is about the same (black curve). However, with the segmentation window that favored the fast component, the magnitude of the fast

component became about an order of magnitude higher than for the slow component (gray line).

The sizes of the peaks in the magnitude spectrum of the correlogram scale with the square of the amplitude of the slow and fast components (assuming that the target and reference have components of identical amplitudes). This follows from the Wiener–Khinchin theorem, which states that the Fourier transform of the auto-correlation function is equivalent to the power spectrum. Therefore, the magnitude spectrum of the cross-correlation is equivalent to the cross-power spectrum [described by Blackman & Tukey (1958)] and, thus, the magnitude peaks scale with the square of the amplitude of signal components. In scaled cross-correlograms, changes in the magnitude spectrum reflect the changes in the shape of the CCH.

To investigate systematically the relation between the spectral magnitude peaks of the correlogram, the properties of the signals, and the scale of the analysis, we plotted the ratio between the amplitude of the signals vs. the square root of the ratio of their magnitudes at 11 and 50 Hz (the two frequencies were chosen not to be integer multiples of each other to avoid harmonics in the magnitude spectrum from interfering with the calculations of peak ratios) as a function of correlation between the fast components (with s = 21 ms; Fig. 4C), segment size (with $r_{FAST} = r_{SLOW} = 1.0$; Fig. 4D), and frequency of the slow component (with s = 21 ms and $r_{FAST} = r_{SLOW} = 1.0$; Fig. 4E).

The relationships between the two types of ratios were linear in all cases, as indicated by straight lines in Fig. 4C–E. Thus, the square root of the ratio between the FFT magnitudes in the scaled CCH was always a linear function of the ratio of the amplitudes of the signal components. The correlations, segment sizes and frequencies affect only the slopes of these linear relationships. The less SCA removes the slow component, the closer is this slope to 1.0 (indicated by dashed lines in Fig. 4C–E). The slope approaches 1.0 as the correlation of the fast component approaches 0.0 (Fig. 4C), as the segment size approaches the period of the slow component (Fig. 4D), and as the frequency of the slow component approaches that of the fast component (Fig. 4E). This analysis indicates that, in continuous signals, SCA operates well across different parameter values and can hence be used as a versatile tool for removing slow components from CCHs.

Pairs of binary signals

Unlike the above examples of continuous signals, in which signal components were based on oscillatory patterns of given frequencies, we generated the spike events using non-homogeneous Poisson processes, i.e. probabilities modulated by a certain envelope function (half-sinusoidal in our simulations, Fig. 5A) (see also Materials and methods). The resulting spike trains can be represented as sequences of 1's and 0's (Fig. 5B), indicating the presence and absence of spikes within each time bin (we used bins of 1 ms in all cases). Therefore, the oscillatory components are not inserted into the signal directly but, rather, ''modulate'' another high-frequency signal. See Materials and methods for more details on generating artificial spike trains for the present analyses.

When Pearson's r is applied to binary signals it is known as the φ (phi) coefficient of correlation. Calculation can be made quickly based on a contingency table containing the counts of all four possible combinations of spiking events across the bins (Table B1 in Appendix B): those that contribute to positive correlations, either both neurons fire or both neurons are silent (entries b and c, respectively); and those that contribute to negative correlations, only one neuron fires and the other is silent (entries a and d). The resulting correlation is a net effect of those four counts, as described in Eqn B3 (Appendix B).

Empty segments. When computing scaled correlation between pairs of binary signals it is necessary to ensure a proper treatment of empty segments of the spike trains. As the duration of the segments reduces, inevitably, within many segments, one or both spike trains will not have a single spike (Fig. 5B). In those cases, φ cannot be calculated due to a division by zero (i.e. in Eqn B3, Appendix B, either the term $c + d$ or $a + c$ is 0). In other words, a signal without spikes does not have variance and, without variance, no correlation can be defined.

A mathematically proper approach is to define the value of correlation for this segment as not-available or not-a-number (e.g. indicated as NaN in Matlab), which means that these segments should not be taken into the average. Consequently, the number of averaged segments is smaller than the total number of segments K. The smaller the s, the larger proportion of segments is expected to be removed from the analysis. This can be seen from the fact that, for a Poisson process, the probability of observing no events in a given interval drops exponentially as a function of the size of the interval and the rate of the process.

The alternative would be to assign zero correlation values to these segments. This approach would not change the shape of a CCH but would affect the magnitudes of estimated correlations, the included zeros reducing the average φ considerably (see Fig. 5C). If zero segments were kept in the analysis, the averages would favor higher firing rates over lower ones and a direct comparison between scaled correlograms would become similar to a comparison of the absolute counts of coincident events between classical CCHs. Such correlations would largely reflect the relative duration of the periods of activity and non-activity for the given neurons, which is not interesting for most analyses. Hence, with the exception of Fig. 5C, all of the analyses presented here were made by removing from the averages the segments that lacked spikes, and this is how we define SCA for binary signals.

By using simulations similar to those shown in Figs 3 and 4, we investigated systematically the following four factors: (i) the segment size, s, (ii) the ratio between the amplitudes of the probability functions in Fig. 5A of the slow and fast components (which is a counterpart of the amplitude in continuous signals), (iii) the ratio of the oscillation frequencies of the two components, and (iv) the combined firing rate of the two spike trains.

Single component. With a non-homogeneous Poisson spike process, the correlation values are expected to be much lower than those obtained with continuous signals (Macke *et al.*, 2009). This is due to the nature of spiking signals, where a very small bin size (e.g. 1 ms) makes the probability of observing coincidences modulated by the signal of interest (e.g. the 60 Hz probability function) small, inducing a correlation smaller than the normalized co-variance of continuous signals. The positive contributions by spikes (i.e. entry b in Table B1 in Appendix B) require the events in both spike trains to occur in the same bin, the likelihood of which event is << 1.0 even if the firing probability functions in Fig. 5A are correlated perfectly. Thus, the count of negative contributions (entries a and d in Table B1 in Appendix B) is likely to be non-zero.

We investigated the relationship between the segment size and measured strength of correlation by simulations for two different oscillation frequencies of a single oscillatory component (50 and 10 Hz). For each component, we used two levels of correlation strength (color coded). As found for continuous signals, the correlations in binary signals were also estimated accurately only if the

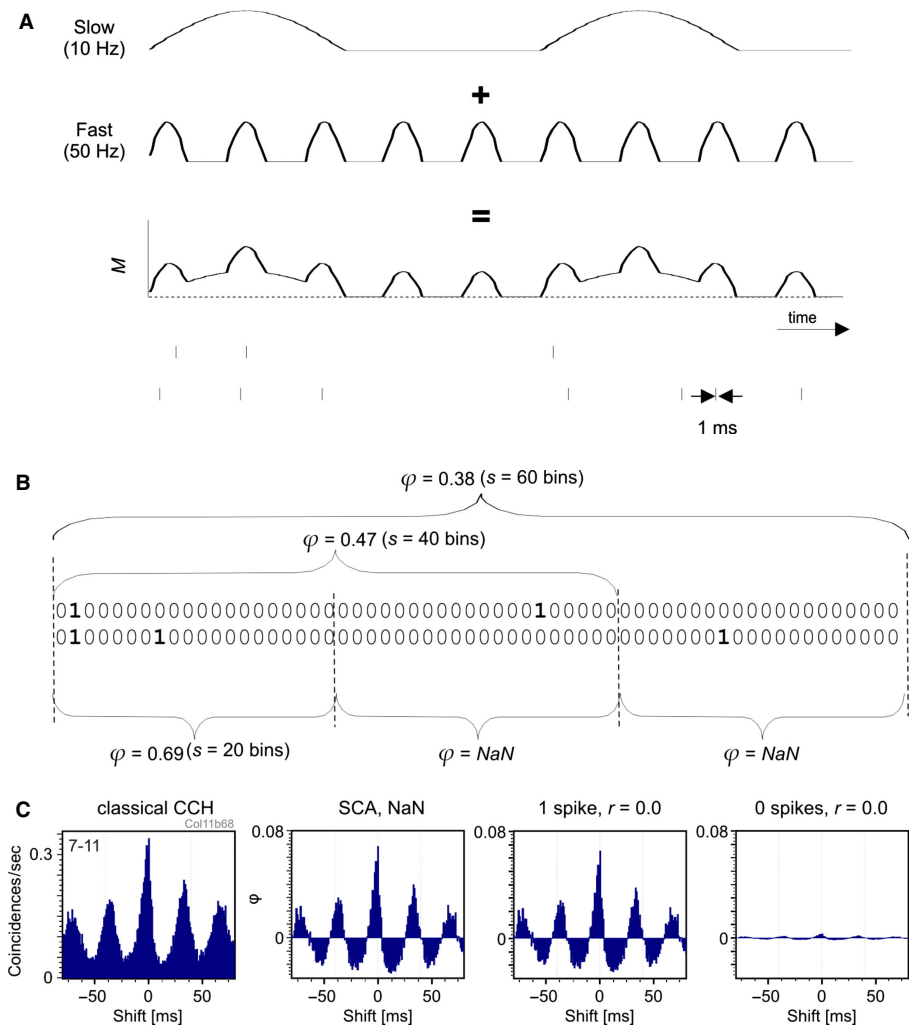

FIG. 5. Analysis of scaled correlation for binary signals. (A) For simulations in Fig. 6, each spike train is created from a non-homogeneous probability function that is created by adding two half-sinusoidal components: a slow one and a fast one. The probability functions of the pairs of spike trains always had a correlation of $r = 1.0$. (B) A segment in which one or both spike trains lack spikes (empty segment) needs to be assigned a not-a-number value (*NaN*) and taken out of analysis. (C) Assigning zero to empty segments does not change the shape of the CCH but reduces the correlation strength. Far left: classical CCH. Middle left: scaled correlation with $s = 40$ ms and with assigning *NaN* to empty segments. Middle right: the same scaled correlation but assigning zero only to segments that lack spikes in only one of the trains (when both spike trains are empty for the segment, the latter is discarded). Far right: zero is also assigned to segments that lack spikes in both spike trains. If the neurons are silent for a considerable amount of time (i.e. low firing rates), as is the case in this example, assignment of zeros reduces the magnitudes of correlations considerably.

segment sizes were equal to or larger than the period of the oscillatory rhythm (Fig. 6A and B). As expected, the correlations reduced when the size of the segment reduced to a sufficient degree.

There was one difference to the results with continuous signals. When the firing rates were relatively low (≤ ∼20 spikes/s), i.e. in the range of cortical single units, and the segment sizes were small (< ∼40 ms), i.e. corresponding to the periods of gamma and beta oscillations, the measured correlation values did not necessarily decrease with the reduction in segment size but sometimes exhibited an increase (Fig. 6A, green and red traces). The reason for that increase in correlation strength lies in the nature of modulated high-frequency signals, i.e. as the small segment sizes increase the number of segments not included in the analysis, they also increase the number of spikes disposed from the analysis. Notably, this disposal is selective for spikes that provide negative contributions to the computed correlation (entries *a* and *d* in Table B1 in Appendix B), as illustrated in Fig. 5B and, consequently, the number of positive contributions (entries *b* and *c*) relatively increases – leading to higher correlations. In other words, in terms of a reduction of sample variability, SCA achieves variance reduction by removing spikes that do not have matches in the counterpart spike trains – the variance of any binary signal being a direct function of the number of the events, i.e. var = $P(1 - P)$, where P indicates a probability to encounter an event and is given by c/n, where c is the number of events in a binary series of the length n.

Two components. In spiking signals it is not possible to create two binary signals, each with its own coefficient of correlation and then sum them up to produce a composite signal that would maintain both correlations, each at a different time scale. This is because, in spikes, all components (slow and fast) are represented by binary events, only the underlying probability functions being continuous. As a consequence, an analysis made for continuous signals in Fig. 3C–E cannot be defined for binary signals. Rather, we focused the analyses on the shapes of CCH (as in Fig. 4), as the shapes reflect the statistical properties of the underlying probability functions. In Fig. 6C–E we

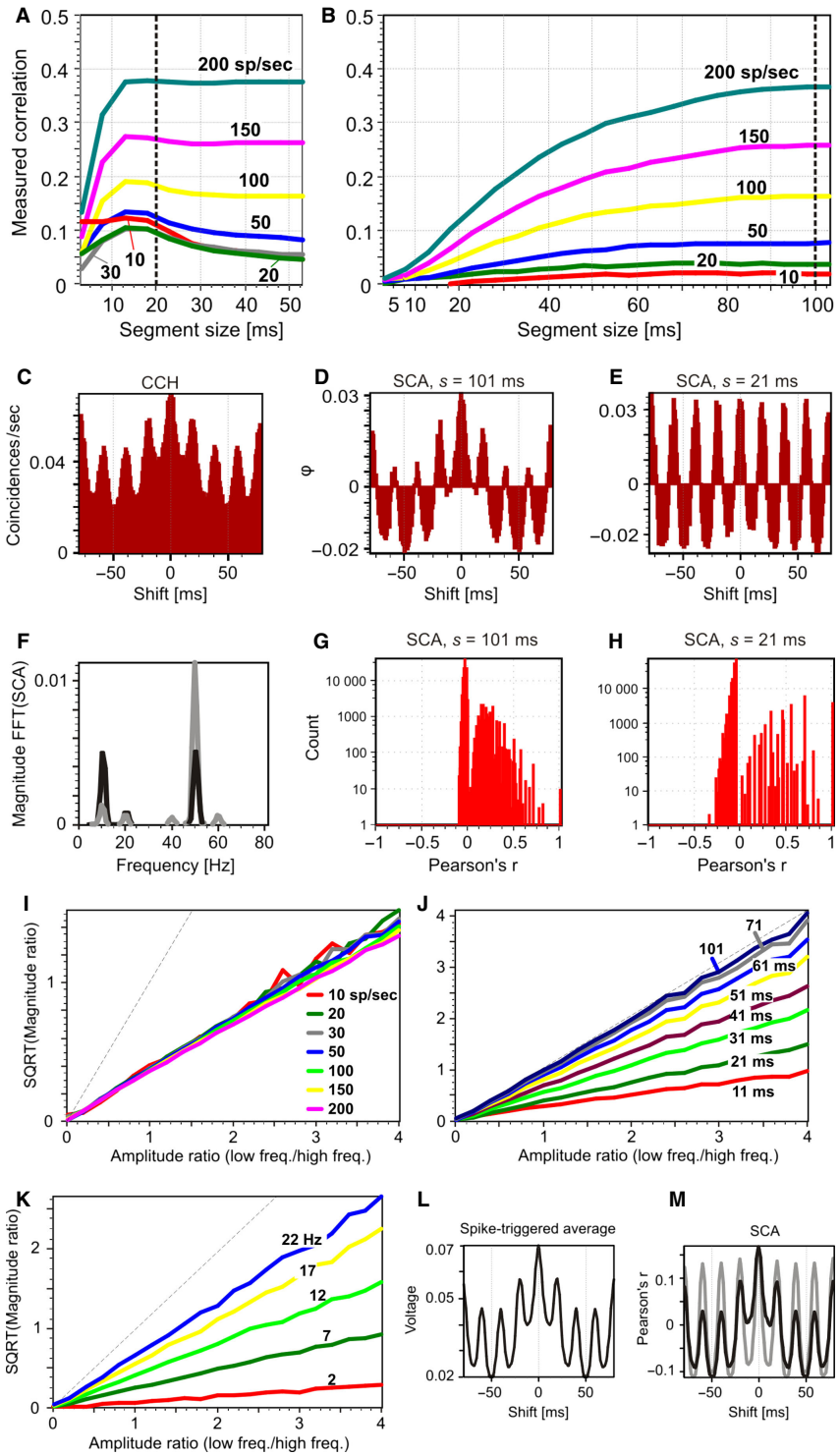

FIG. 6. Analysis of the degree to which SCA attenuates contributions of slow components in pairs of binary signals (A–K) and in combinations of binary and continuous signals (L and M). Binary signals have one oscillating component of either 50 Hz (A) or 10 Hz (B). The color code indicates the combined firing rate of the spike trains (10–200 spikes/s) and the vertical dashed line indicates the segment size that corresponds to the period of the oscillation cycle. (C–E) An example effect of scaled correlation on the shape of CCH that contains two components, slow and fast (frequencies of 11 and 50 Hz, respectively). (C) Original CCH. (D) Scaled correlogram with s = 101 ms. (E) Scaled correlogram with s = 21 ms. (F) Magnitude of the FFT for the correlograms in D (black) and E (gray). (G and H) Distribution of r-values in D and E, respectively. (I–K) Analysis of the magnitude spectrum of scaled cross-correlograms by computing the square root (SQRT) of the ratio between peak sizes as illustrated in F at 11 and 50 Hz, shown as a function of the ratio between the amplitudes of the slow and fast component probability functions (x-axis). Color codes were used to indicate different combined firing rates (I), segment sizes (J), and the frequency of the slow component (K). (L–M) The same analysis as in C–E but for combinations of continuous and binary signals with 10 and 50 Hz components. (L) Spike-triggered average of the continuous signal (equivalent to a CCH between the two signals). (M) Scaled correlation computed with s = 101 ms (black) and s = 21 ms (gray). For interpretation of color references in figure legend, please refer to the Web version of this article.

show an example of a change in the shape of CCH depending on the choice of the scale of analysis. The original CCH for a combination of 10 and 50 Hz signals of equal amplitude (combined firing rate = 40 spikes/s) indicates the presence of both components (Fig. 6C) and so does SCA with large scale, which reveals the identical shape (Fig. 6D). Importantly, SCA computed with short segments (s = 21 ms) removes the slow, revealing the fast component (Fig. 6E), much like the analysis of continuous signals (e.g. Fig. 4A). Also, the analysis of the magnitude of the FFT of the correlogram on these two scaled correlograms indicates an increase in the relative magnitude of the fast component and concomitant reduction in the magnitude of the slow component (black vs. gray trace in Fig. 6F), much as was the case for continuous signals (Fig. 4B).

For binary signals, the distributions of individual r-values are bimodal (Fig. 6G and H), with the cutting point at $r = 0$. With low firing rates, a segment is likely not to contain a single coincident event, in which case the correlation of the segment will have a small negative value. In the case that a segment contains a coincidence, the correlation will be most likely to be positive, and it may cover any value between 0 and 1.0, including the perfect correlation of $r = 1.0$ (when this coincidence is the only event within the segment).

We made a detailed analysis of the effects of scale size on the shape of the correlograms by using the same method based on FFT as reported for continuous signals. We plotted the amplitude ratio between probability functions of slow and fast components (Fig. 5A) against the square root of the magnitude ratio in FFT and systematically manipulated the firing rates of units (11 and 50 Hz; s = 21 ms; Fig. 6I), the segment size (firing rate = 40 spikes/s; Fig. 6J), and the frequency of the slow component (firing rate = 40 spikes/s; Fig. 6K). Again, the relationships between the two ratios stayed linear for all parameter values. Moreover, the results of the analysis were fully independent when the firing rates were changed (rates were changed by an equal factor for the slow and fast components; Fig. 6I). Much as for the continuous signals, the slope of the linear relationship for binary signals approached 1.0 as the scale approached the period of the slow component (Fig. 6J), and as the frequency of the slow component approached that of the fast component (Fig. 6K). The results indicate that, when the shape of the CCH is of concern, SCA removes slow components from binary signals in much the same way as from continuous signals.

Combinations of continuous and binary signals

The SCA can also be applied to analyses that correlate a binary signal with a continuous signal (e.g. LFP correlated to spiking activity) – also known as a spike-triggered average (Gray & Singer, 1989). When Pearson's r is computed with such combined signals, it is called the point-biserial coefficient of correlation and is described in Appendix B.

The results obtained in the analyses of those combined signals were very similar to and fully consistent with those obtained for continuous and binary signals separately. In Fig. 6L and M we show examples of the classical CCH and scaled CCH made with long (s = 101 ms) and short (s = 21 ms) scales. The size of the scale has the same effect as shown previously in Figs 4A and 6C–E for continuous and binary signals, respectively. For the sake of brevity, other analysis results are not shown.

Applying scaled correlation analysis to neurophysiological data

In Fig. 7A–J we show examples of CCHs computed from neuronal spiking activity recorded from the cat visual cortex under anesthesia and in response to visual stimulation (see Materials and methods for details). These examples compare the use of SPs with the use of SCA. In Fig. 7A, an example of a CCH is shown with a flat SP (i.e. no rate co-variation), and consequently the shape of the correlogram obtained with SCA (Fig. 7F) was very similar in many details to the classical one, also when the SP is subtracted (CCH − SP). Moreover, the detailed structures of the CCHs, i.e. the relative sizes of the neighboring bins, remained largely preserved across all of the plots. This illustrates that, without rate co-variation, SCA produces the same shape of a CCH as the classical approaches – including all of the details on the bin-by-bin basis [see Appendix F for the estimation of significance of averaged correlation coefficients in SCA based on the method of fixed effects by Hedges & Olkin (1985)].

In Fig. 7B we show an example of a CCH that consists only of slow components. The graph indicates slow rate co-variation without a narrow center peak. The SP was not fully successful in removing these slow components, suggesting that the slow rate co-variation was not time-locked perfectly to the stimulus onset – a problem that the SP cannot resolve. In contrast, SCA with s = 40 ms removed this rate co-variation much more efficiently, as indicated by a near-flat CCH (Fig. 7G). Also, as shown in Fig. 7C, SCA can remove rate co-variation even when the SP is completely flat and, thus, when rate co-variation is fully independent of the timing of the stimulus. In this case, the classical CCH exhibits a wide peak and the SP is nevertheless flat. With s = 40 ms, SCA removed this broad peak almost entirely (Fig. 7H), which should be contrasted to the failure to do so by a subtraction of the SP from the classical CCH.

In Fig. 7D and E, we show two example CCHs for the same pair of units but in response to different stimuli (grating and plaid stimuli, respectively, see Materials and methods). Here, an estimate of the change in the strength of synchrony is hindered by the slow rate co-variation in the original CCHs. SPs also do not help much. Only SCA is helpful because – as judged by the shape of CCHs – it removes the slow components much more efficiently than does the SP (Fig. 7I and J). In addition, Fig. 7D illustrates a real-world example in which SCA can lead to a switch in the sign of correlation; the troughs of the oscillation that are positioned at half the period of the oscillation cycle indicate negative correlations detectable only when SCA is applied (e.g. Fig. 7I). This is not always achieved by subtraction of the SP as troughs remain positioned above the baseline of the CCH, which is another indicator that SPs do not account fully for the rate co-variation.

To illustrate further the versatility of scaled correlation in practice with spiking data, four examples of CCHs with unusual shapes and the corresponding SCA (s = 30 ms in all cases) are shown in Fig. 7K–N. Irrespective of the shape, scaled correlation removes the slow components and retains the fast components.

These results indicate that the conclusions obtained from simulations also apply to real data; if a classical CCH indicates large rate co-variation, SCA will remove these slow components but will retain detailed information about the fast components.

Multi-scale analysis

Further analysis of the non-stimulus-locked rate co-variation in Fig. 7C revealed that the underlying source is an oscillatory rhythm in the theta range, which is shown in detail in Fig. 8A. The theta component is visible when the cross-correlation window is expanded to ± 1000 ms. The resulting plots show an oscillatory rhythm of ~5 Hz. Interestingly, this is not the only source of slow activity in this CCH. Theta activity is superimposed on top of yet another slow component that had a time period of > 1 s. The SP captured this

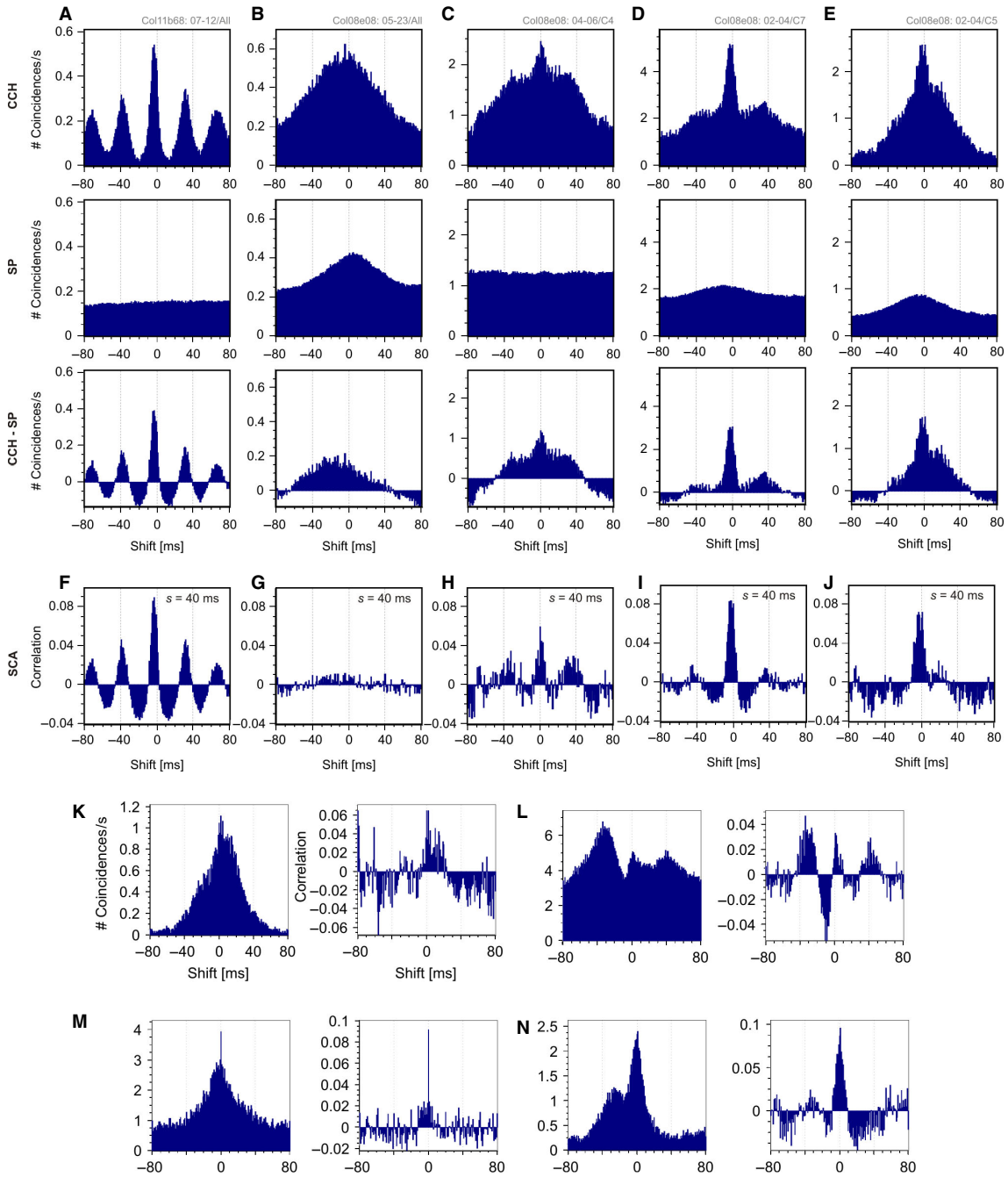

FIG. 7. Example application of scaled correlation to spiking signals recorded from the cat visual cortex. (A–E) CCH, SP and the difference between the two (CCH − SP) shown for five example pairs of multi-unit activity recorded from the cat visual cortex. (A) An example of precise neuronal synchrony (large center peak) supported by strong oscillatory activity in the beta range (large satellite peaks at ∼35 ms phase shift). (B) Example CCH that does not indicate neuronal synchronization but only slow rate co-variation as indicated by the wide center peak and the elevated SP. This result is typically obtained when CCH is computed between spike trains that include strong transient changes in rate responses due to, e.g. an abrupt onset of the stimulus (the so-called ON-responses). (C) Example CCH in which the center peak contains both a narrow component indicating neuronal synchrony and a much slower wide component. In this example, the slow component is not time-locked to the stimulus, as indicated by a flat SP. (D and E) The CCHs are computed for the same pair of units but in response to two different stimuli, illustrating the difficulty in determining how synchronization strength changes as a function of stimulus properties. (F–J) Application of SCA to the CCHs shown in A–E by using the scale s = 40 ms, which is suitable for extraction of signals supported by an oscillation frequency of 25 Hz or higher. (K–N) Further examples of CCHs of unusual shapes illustrating that SCA maintains the detailed structure of the correlogram at fast time scales. In all cases s = 30 ms.

slowest component well, the oscillatory pattern in the theta range being revealed accurately after its subtraction from the original CCH (CCH − SP, Fig. 8A). This indicates that this slow component is locked to the stimulus. As would be expected, SCA revealed the same oscillatory pattern when computed with the same cross-correlation window (± 1000 ms) and with an appropriate scale (s = 200 ms) (Fig. 8A, SCA). Again, SCA and CCH − SP match in much of the detailed relative relations between the neighboring bins, indicating that SCA is an accurate method for removing the slow components from CCHs.

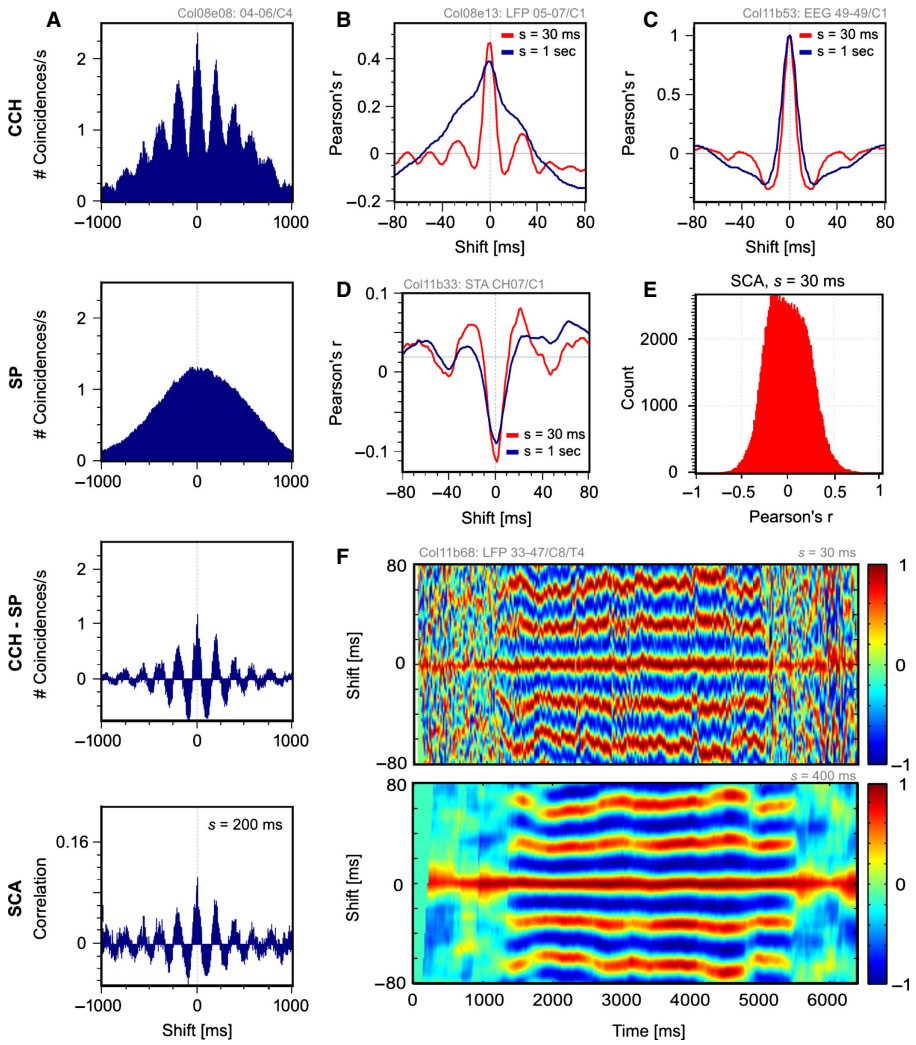

FIG. 8. Example of a multi-scale analysis and application of SCA to real continuous signals. (A) A raw CCH, SP, their difference and SCA computed for the same data as in Fig. 7C except that the cross-correlation window is ±1000 ms and the scale s = 200 ms. (B–D) SCA computed on signals other than pairs of spike trains. (B) SCA for continuous data obtained by recording LFPs computed with large (s = 1000 ms; blue) and small (s = 30 ms; red) scale. (C) The same as in B but calculated on an electroencephalogram. In this case an auto-correlation histogram is computed. (D) Scaled correlation computed for one continuous (LFP) and one binary signal. (E) The distribution of r-values of the scaled correlogram in D (s = 30 ms). (F) Intensity plot of sliding window analysis with different scales. SCA for a pair of LFP signals over a ∼6.5 s period computed either with s = 30 ms (upper graph) or s = 400 ms (lower graph) with sliding windows of a size equal to the scale (i.e. 30 or 400 ms) that were slid in steps of 20 ms. The stimulus was presented at 1000 ms and was removed at 5000 ms. For interpretation of color references in figure legend, please refer to the Web version of this article.

Local-field potentials and electroencephalogram signals

Example applications of SCA to continuous signals are shown for LFPs (Fig. 8B, CCH) and electroencephalogram signals (Fig. 8C, auto-correlation histogram). Similar to the application on spiking activity, the correlations between slow components of continuous signals are removed efficiently and the dynamics of fast components is revealed when small scales are chosen.

In Fig. 8D we show example spike-field correlograms with SCA computed at two different scales. Here, for small values of s, stronger correlations are detected than for large values of s, indicating that the slow components attenuated the correlations produced by the fast components. The distribution of r-values is shown in Fig. 8E.

Sliding window analysis is also a popular type of application of CCH to data analysis where the calculations are made over small consecutive time windows and it reveals in this way how synchronization and/or oscillations evolve over time (e.g. along an experimental trial) (e.g. Roelfsema *et al.*, 1997). Sliding window analysis can also be performed with SCA and an example for a pair of LFP signals is shown in Fig. 8F. Here a window of size equal to the scale was slid in steps of 20 ms. For each window, scaled correlation CCH was computed and plotted as an intensity plot. When sliding window analysis is performed with a small scale (s = 30 ms, top), many details of the underlying dynamics can be recovered in the plot. These details are hidden in the plots computed with a large scale (s = 400 ms, bottom) or with a classical CCH (not shown).

Comparison to spectral methods

Spectral techniques are widely used to study different frequency components of neurophysiologic signals (Jarvis & Mitra, 2001; Pesaran *et al.*, 2002) and have also been used to address issues similar to those for which SCA has been designed. Thus, it is important to know how SCA compares with analyses based on various spectral techniques. We first investigated the degree to which spectral techniques can be used as an alternative to SCA for removing the slow components from a CCH. Next, we compared the performance of

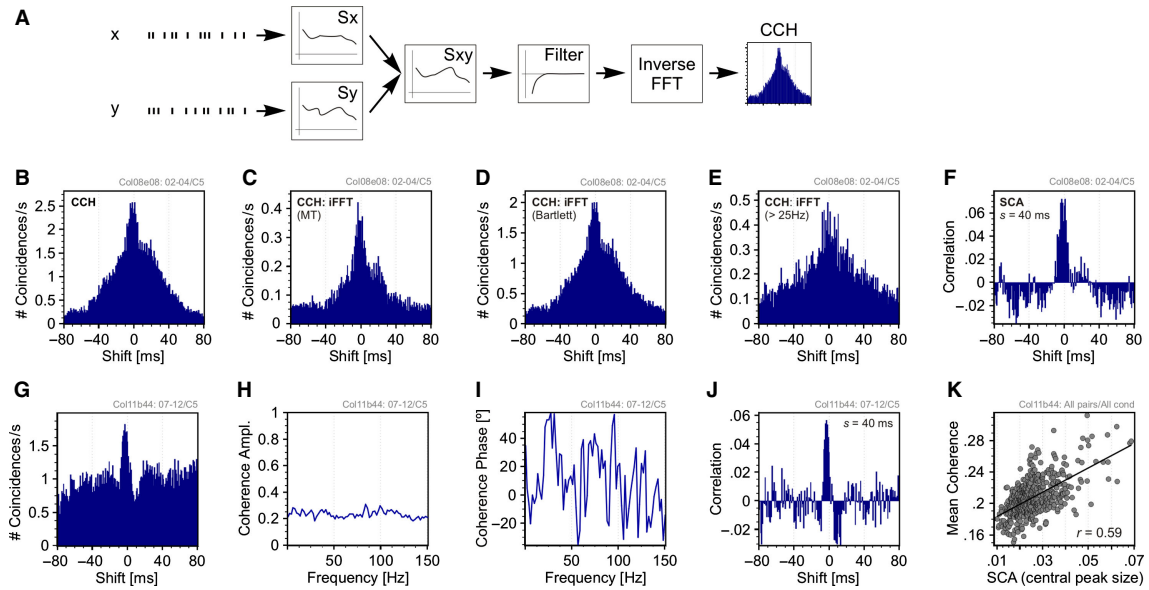

FIG. 9. Comparison between correlation analysis and spectral techniques. (A) Schematic representation of computing a filtered CCH on binary signals. Sx, Sy and Sxy are the spectra of the first, x, and second, y, spike train, and the cross-spectrum, respectively. (B) A CCH with a fast and slow component. The CCH in B is reconstructed by reversing the cross-spectrum (iFFT) estimated with multi-taper (MT) (C), or rectangular Bartlett window (D). (E) The CCH in B filtered by reversing a high-passed cross-spectrum estimated with the Bartlett window. (F) CCH in B computed with scale correlation, s = 40 ms. (G) An example CCH with very weak oscillatory component. (H) Coherence magnitude and (I) coherence phase for the data used to compute the CCH in G. (J) Scaled correlation corresponding to data in G. (K) Correlation between the size of the central peak in SCA (computed with s = 6000 ms) and average coherence, computed for all pairs of cells and all stimuli in a data set with weak oscillations.

coherence techniques as measures of synchronization with those based on cross-correlation computed with scaled correlation.

Removing slow components from a cross-correlation histogram by filtering

One potential approach for removing slow components from pairs of signals comes from the Wiener–Khinchin theorem, from which it follows that the CCH is the inverse Fourier transform of the cross-spectrum (Blackman & Tuckey, 1958). The cross-spectrum can be computed by multiplying the Fourier spectrum of the first signal with the complex conjugate of the Fourier spectrum of the second signal (Jenkins & Watts, 1968). Thus, for a CCH between binary signals x and y, one may attempt to remove the slow components from the CCH by first computing the Fourier spectra of the two signals (S_x and S_y), next computing the cross-spectrum between the two signals (S_{xy}), and then by filtering the cross-spectrum (by setting the low-frequency components to zero). Finally, the 'filtered' CCH is computed as the inverse FFT of the 'filtered' cross-spectrum. See Fig. 9A for the computational steps required for such a calculation.

To obtain a smooth estimate of the frequency spectra, it is necessary to apply windowing techniques (Jenkins & Watts, 1968). We first considered the windowing method based on multi-tapers because such methods have been already used with spiking signals (Jarvis & Mitra, 2001; Pesaran *et al.*, 2002). With multi-tapers, the original signals are multiplied with a set of orthogonal tapering functions (e.g. Slepian sequences), the Fourier transforms of the resulting product signals are computed for each taper separately, and finally the spectral components are averaged across all of the tapers (Percival & Walden, 1993). To exemplify this, we first reconstructed the CCH in Fig. 9B (replotted from Fig. 7E) by using three Slepian tapers. The shape of the resulting CCH (Fig. 9C) only resembled the original but much of the structure was changed and the detailed structure was absent even in this non-filtered CCH. Thus, tapers produce spurious components and hence could not be expected to yield reliable results when filtering is applied.

Another, simpler, spectral smoothing method, the Barlett method (Djurić & Kay, 1999), produced better results. Here, the signals are windowed with a rectangular function and hence spurious components are not added to the reconstructed CCH. The reconstructed example CCH is shown in Fig. 9D. Therefore, we attempted to remove slow components from CCHs reconstructed by using Barlett's windowing method and by setting the low-frequency bins (≤ 25 Hz, corresponding to s = 40 ms) of the cross-spectrum to zero. This filtering did not work to a satisfactory degree. For example, when the CCH in Fig. 9B was 'filtered' by this method, the resulting CCH still contained large slow components, and fast components also seemed to be attenuated (Fig. 9E). In contrast, scaled correlation with s = 40 ms removed the slow component efficiently (Fig. 9F).

Scaled correlation and coherence

In the frequency domain, an equivalent of correlation is coherence (Jenkins & Watts, 1968). Coherence measures the periodic correlation between signals, and has been suggested as an alternative to correlation analysis (Pesaran *et al.*, 2002; Sandberg & Hansson, 2006). We investigated how this method relates to scaled correlation, in particular when it is applied to non-periodic signals. As an example, we show a CCH with a narrow center peak but with little or no oscillatory activity (Fig. 9G), suggesting that the signals, although synchronized, do not exhibit prominent periodicity. This is confirmed by the coherence analysis computed by using the multi-tapers (Zeitler *et al.*, 2006; again, by using three Slepian tapers). Spectra were estimated with non-overlapping sliding windows of 512 ms. Coherence showed no dominant frequency (Fig. 9H) and a noisy phase relationship between signals (Fig. 9I). Therefore, there was no peak frequency at which correlation between signals could be measured. In

contrast, SCA, which does not rely on periodicity, in this case showed a clear center peak (Fig. 9J).

We next investigated whether in these cases SCA correlated to the average coherence computed over the whole frequency range between 0 and 500 Hz (the sampling frequency was 1 kHz). To this end, we computed the correlation between the size of the peak of SCA and coherence averaged across all bands for 36 pairs (resulting from nine multi-units), the responses of which to 14 stimulation conditions (504 data points in total) were recorded simultaneously and did not exhibit periodic activity, as assessed from auto-correlation functions (average oscillation score in the 20–40 Hz band = 2.37, see Mureşan *et al.*, 2008). The scale, *s*, was set equal to the trial length. The correlation was positive ($r = 0.59$; see Fig. 9K). As would be expected, this correlation was much smaller with strong periodic activity in neuronal responses. In another data set, recorded from the same multi-units and stimuli but at a later time, neurons exhibited oscillatory responses in the beta-high band (oscillation frequency = ~27 Hz; average oscillation score in the 20–40 Hz band = 6.81). In this case, the correlation between the averaged coherence and SCA peak was low ($r = 0.28$) but the coherence at the oscillation frequency of 27 Hz correlated much better with SCA ($r = 0.57$) (results not shown). Therefore, coherence measures produce results that are similar to those obtained by SCA provided that there is good periodicity structure in the data. However, when periodicity is missing, another type of measure extracted from coherence results may be more optimal to describe the signals. In contrast, SCA does not rely on the assumptions of periodicity and, hence, its results are independent of the presence of this property in the data.

Discussion

In the present study we proposed a measure of neuronal synchrony based on the reduction of the sampled signal variances. The method enables the segregation of correlations at different time scales (e.g. frequency ranges). By basing the analysis on a fast (short) time scale, the contributions of correlations with slower time scales are strongly attenuated in the resulting CCH or auto-correlation histogram. This has the effect that unwanted (slow) rate co-variations are removed from the CCH. SCA can be applied to binary signals, continuous signals, and combinations of continuous and binary signals to remove the contributions of slow components and to extract precise neuronal synchronization between these signals. SCA is more efficient at removing slow components than the SP as it can be applied even when SPs are flat, i.e. when rate co-variation is not stimulus-locked.

The attenuations made by scaled correlation are not always perfect. The effects of the method are limited when the difference between the time scales is small and, in the same time, the signals that need to be attenuated have much larger amplitudes than the signals of interest. Nevertheless, as the simulations show, SCA attenuates slow signals well for a wide range of parameters and, as our experience indicated, it performs very well on neurophysiological data.

An advantage of using Pearson's coefficient of correlation is that its mathematical and statistical properties have been studied in much detail. The procedures for averaging multiple *r*-values have been investigated (Fisher, 1915; Corey *et al.*, 1998; Hunter & Schmidt, 1990; Field, 2001; Raju & Brand, 2003; Millsap, 1988, 1989) and the tables and algorithms for testing the statistical significance of *r* are available. We have also proposed a correction for multiple comparisons that is suitable for application to CCHs based on the requirement that three neighboring peaks are significant (Appendix F).

The calculation of SCA is fast and, to assist its easy implementation, we provide, as a free download, open-source, speed-optimized routines and compiled libraries (see Appendix B for details and links). Most of the demonstrations and tests provided in the present study were based on the extraction of correlations on fast time scales (e.g. < 50 ms), in the range of beta/gamma oscillations. However, the same principles apply for examining signals at any other time scales (e.g. preserving those in the range of theta oscillations), as the time scale of interest can be freely chosen. Also, the application of SCA is not limited to neuronal activity but the same tools can be applied to any type of signals if it is of interest to segregate the contributions of fast and slow components to cross-correlation or auto-correlation functions. Thus, the relevant scale may depend in each analysis on the research question at hand and may thus be decided *a priori* by the researcher. Alternatively, the scale of interest may be chosen after an initial inspection of the data by applying the classical CCHs, or a frequency analysis (e.g. Fourier spectrum). Scaled correlation may prove particularly useful for extracting small time delays in neuronal spiking activity. These delays are typically extracted from CCHs and require the analysis to focus on beta and gamma oscillations (König *et al.*, 1995; Schneider *et al.*, 2006; Nikolić, 2007; Havenith *et al.*, 2011).

Choosing between scaled correlation analysis and spectral methods

One straightforward approach to removing slow components from signals is to simply filter the input signals prior to the computation of the cross-correlation. The limitation of this approach is that it is applicable only to continuous signals because binary series (point processes) cannot be filtered such that another binary signal is obtained. In other words, for binary signals, filtering is not defined because it should be restricted only to the removal or insertion of binary events (spikes). Therefore, filtering cannot be used as a general approach for removing slow components from CCHs. Scaled correlation does not filter signals directly and, hence, SCA can be applied equally efficiently to signals of any nature, i.e. binary or continuous.

To test an alternative to direct filtering on binary data, we relied on the Wiener–Khinchin theorem (Blackman & Tuckey, 1958). We computed the cross-spectrum of the two spike trains, set its low-frequency bins to zero, and then inverse-Fourier transformed it to obtain a ''filtered'' CCH. We showed that, only without filtering, this approach can reconstruct the original CCH fairly accurately and only if certain windowing techniques (e.g. Bartlett) but not others are used. For example, the reconstruction of a CCH from the cross-spectrum estimated with multi-tapers has the problem that the reconstructed CCH also contains components corresponding to the tapers. Thus, the shape of the reconstructed CCH also does not correspond to the original. Consequently, although useful for a number of analyses (Pesaran *et al.*, 2002), multi-taper methods cannot be used to reconstruct a CCH and, hence, also cannot be used to remove slow components from a CCH. Problems also exist with other spectral methods because the spectral representation of binary and/or non-periodic signals is spread across multiple frequency components of the spectrum. Therefore, by filtering signals by setting the low-frequency bins to zero (Jenkins & Watts, 1968), the representation of the slow components is not eliminated completely.

We conclude that spectral filtering methods, although useful for a number of analyses, cannot be used for the accurate removal of slow components from CCHs. Particularly strong limitations are encountered when the correlated signals have representations spread across multiple components of the frequency spectrum, as is the case with trains of action potentials and/or with non-periodic signals. Therefore,

for any analysis based on CCHs, scaled correlation is a more efficient way to selectively extract the correlations between the fast components of the signals.

Our results also showed that coherence could not be a replacement for SCA (and vice versa) as the two measures are correlated only in some cases and to a limited degree. The strength of correlation depends on data properties and on the chosen features of the coherence function. Thus, as described previously by Jenkins & Watts (1968), correlation and coherence are not identical measures but provide complementary information.

In general, the main property that distinguishes the present methods from the spectral techniques is that scaled correlation does not assume a periodic nature of the signals, being equally applicable to the measurement of synchrony with and without oscillations. Consequently, depending on the researcher's preference and the scientific problem at hand, SCA may be chosen over other techniques.

Fisher's z-transformation

One commonly recommended procedure for averaging the values of r is to make a Fisher z-transformation of r-values prior to their averaging, and then transform the average back into an r-value (Fisher, 1915). This procedure is designed to reduce the skew in r-distributions that occurs with larger values of r and to thereby reduce the bias towards underestimating the average of such skewed distributions. However, there are different opinions among researchers about whether or not such a transform is beneficial to the analysis (Silver & Dunlap, 1987; Corey *et al.*, 1998; Hunter & Schmidt, 1990; Field, 2001). Fisher's z-transformation is an option when computing SCA with continuous signals (the equations are provided in Appendix A) but should not be used with spike signals for the following reasons. As we have shown, the distribution of r's has a large number of small (negative) values (see Appendix E). These small values do not suffer from the problem of skewed distributions. More importantly, the distribution is also very likely to contain values with $r = 1.0$, which occur when, within the segment, the two units fire one or more pairs of spikes in perfect coincidence. Fisher's z-transformation cannot be added to the sum with $r = 1.0$ as it produces $+\infty$.

In conclusion, in the measurements of precise neuronal synchrony, the issue of contaminating slow rate co-variation does not need to be a problem. With the application of SCA, slow rate co-variation can be efficiently separated from precise synchrony and the false detection of synchrony can be prevented. For these reasons, SCA may serve as a versatile tool for the investigation of correlations across a variety of neurophysiological signals.

Acknowledgements

The authors would like to thank Julia Biederlack for help with the acquisition of the data used to compute the example analyses, Saskia Nagel and Fabian Fußer for the help in acquiring extensive practical experience with the present methods, and Martha N. Havenith for fruitful discussions. Financial support was provided by a grant from the Deutsche Forschungsgemeinschaft (number NI 708/2-1), Hertie Foundation, Alexander von Humboldt Stiftung, LOEWE Neuronale Koordination Forschungsschwerpunkt Frankfurt (NeFF), Max-Planck Geselschaft, Frankfurt Institute for Advanced Studies, a grant from the Romanian Government (Human Resources Program, project number PNII-RU TE-11/2010, contract no. 23/28.07.2010 financed by CNCS/UEFISCDI), and a grant for the ''Max Planck – Coneural Partner Group''.

Abbreviations

CCH, cross-correlation histogram; FFT, fast Fourier transform; LFP, local-field potential; SCA, scaled correlation analysis; SP, shift predictor.

References

Aguinis, H. & Whitehead, R. (1997) Sampling variance in the correlation coefficient under indirect range restriction: implication for validity generalization. *J. Appl. Psychol.*, **82**, 528–538.

Alexander, R.A., Carson, K.P., Alliger, G.M. & Barrett, G.V. (1984) Correction for restriction of range when both X and Y are truncated. *App. Psychol. Meas.*, **8**, 231–241.

Averbeck, B.B., Latham, P.E. & Pouget, A. (2006) Neural correlations, population coding and computation. *Nat. Rev. Neurosci.*, **7**, 358–366.

Beggs, J.M. & Plenz, D. (2003) Neuronal avalanches in neocortical circuits. *J. Neurosci.*, **23**, 11167–11177.

Biederlack, J.M., Castelo-Branco, M., Neuenschwander, S., Wheeler, D., Singer, W. & Nikolić, D. (2006) Brightness induction: rate enhancement and neuronal synchronization as complementary codes. *Neuron*, **52**, 1073–1083.

Blackman, R.B. & Tukey, J.W. (1958) *The Measurement of Power Spectra From the Point of View of Communication Engineering*. Dover, New York, NY.

Brody, C.D. (1999) Correlations without synchrony. *Neural Comput.*, **11**, 1537–1551.

Corey, D.M., Dunlap, W.P. & Burke, M.J. (1998) Averaging correlations: expected values and bias in combined Pearson rs and Fisher's z transformations. *J. Gen. Psychol.*, **125**, 245–261.

Djurić, P.M. & Kay, S.M. (1999) Spectrum estimation and modeling. In Madisetti, V.K. & Williams, D.B. (Eds), *Digital Signal Processing Handbook*. CRC Press, Boca Raton, FL.

Field, A.P. (2001) Meta-analysis of correlation coefficients: a Monte Carlo comparison of fixed- and random-effects methods. *Psychol. Methods*, **6**, 161–180.

Fisher, R.A. (1915) Frequency distribution of the values of the correlation coefficient in samples of an indefinitely large population. *Biometrika*, **10**, 507–521.

Fries, P., Roelfsema, P.R., Engel, A.K., König, P. & Singer, W. (1997) Synchronization of oscillatory responses in visual cortex correlates with perception in interocular rivalry. *Proc. Natl. Acad. Sci. USA*, **94**, 12699–12704.

Gerstein, G.L. & Perkel, D.H. (1972) Mutual temporal relationships among neuronal spike trains. Statistical techniques for display and analysis. *Biophys. J.*, **12**, 453–473.

Gray, C.M. & Singer, W. (1989) Stimulus-specific neuronal oscillations in orientation columns of cat visual cortex. *Proc. Natl. Acad. Sci. USA*, **86**, 1698–1702.

Gray, C.M., König, P., Engel, A.K. & Singer, W. (1989) Oscillatory responses in cat visual cortex exhibit inter-columnar synchronization which reflects global stimulus properties. *Nature*, **338**, 334–337.

Grün, S., Diesmann, M. & Aertsen, A. (2002) Unitary events in multiple single neuron activity. I. Detection and significance. *Neural Comput.*, **14**, 43–80.

Hahn, G., Petermann, T., Havenith, M. N., Yu, S., Singer, W., Plenz, D. & Nikolić, D. (2010) Neuronal avalanches in spontaneous activity in vivo. *J. Neurophysiol.*, **104**, 3312–3322.

Havenith, M.N., Yu, S., Biederlack, J., Chen, N.-H., Singer, W. & Nikolić, D. (2011) Synchrony makes neurons fire in sequence – and stimulus properties determine who is ahead. *J. Neurosci.*, **31**, 8570–8584.

Hedges, L.V. & Olkin, I. (1985) *Statistical Methods for Meta-Analysis*. Academic Press, Orlando, FL.

Held, J.D. & Foley, P.P. (1994) Explanations for accuracy of the general multivariate formulas in correcting for range restriction. *App. Psychol. Meas.*, **18**, 355–367.

Hunter, J.E. & Schmidt, F.L. (1990) *Methods of Meta-Analysis: Correcting Error and Bias in Research Findings*. Sage, Newbury Park, CA.

Ikegaya, Y., Aaron, G., Cossart, R., Aronov, D., Lampl, I., Ferster, D. & Yuste, R. (2004) Synfire chains and cortical songs: temporal modules of cortical activity. *Science*, **204**, 559–564.

Jarvis, M.R. & Mitra, P.P. (2001) Sampling properties of the spectrum and coherency of sequences of action potentials. *Neural Comput.*, **13**, 717–749.

Jenkins, G.M. & Watts, D.G. (1968) *Spectral Analysis and Its Applications*. Holden-Day, San Francisco, CA.

Kim, S.H. (1992) *Statistics and Decisions: An Introduction to Foundations*. CRC Press, Boca Raton, FL.

König, P. (1994) A method for the quantification of synchrony and oscillatory properties of neuronal activity. *J. Neurosci. Methods*, **54**, 31–37.
König, P., Engel, A.K., Roelfsema, P.R. & Singer, W. (1995) How precise is neuronal synchronization? *Neural Comput.*, **7**, 469–485.
Kuo, Z.-Y. (1930) The genesis of the cat's response to the rat. *J. Comp. Psychol.*, **11**, 1–30.
Lamme, V.A & Spekreijse, H. (1998) Neuronal synchrony does not represent texture segregation. *Nature*, **396**, 362–366.
Macke, J.H., Berens, P., Ecker, A.S., Tolias, A.S. & Bethge, M. (2009) Generating spike trains with specified correlation coefficients. *Neural Comput.*, **21**, 397–423.
Millsap, R.E. (1988) Sampling variance in attenuated correlation coefficients: a Monte Carlo Study. *J. Appl. Psychol.*, **73**, 316–319.
Millsap, R.E. (1989) Sampling variance in the correlation coefficient under range restriction: a Monte Carlo Study. *J. Appl. Psychol.*, **74**, 456–461.
Moca, V.V., Nikolić, D. & Mureşan, R.C. (2008) Real and modeled spike trains: where do they meet? In Vera Kurková, Roman Neruda & Jan Koutník. (eds.), *Lecture Notes in Computer Science*. Springer, Berlin, Heidelberg, pp. 488–497.
Munk, M.H.J., Nowak, L.G., Nelson, J.I. & Bullier, J. (1995) Structural basis of cortical synchronization II. Effects of cortical lesions. *J. Neurophysiol.*, **74**, 2401–2414.
Mureşan, R.C., Jurjut, O.F., Moca, V.V., Singer, W. & Nikolić, D. (2008) The oscillation score: an efficient method for estimating oscillation strength in neuronal activity. *J. Neurophysiol.*, **99**, 1333–1353.
Nikolić, D. (2007) Non-parametric detection of temporal order across pairwise measurements of time delays. *J. Comput. Neurosci.*, **22**, 5–19.
Nikolić, D., Häusler, S., Singer, W. & Maass, W. (2009) Distributed fading memory for stimulus properties in the primary visual cortex. *PLoS Biol.*, **7**, e1000260.
Nowak, L.G., Munk, M.H.J., James, A.C., Girard, P. & Bullier, J. (1999) Cross-correlation study of the temporal interactions between areas V1 and V2 of the macaque monkey. *J. Neurophysiol.*, **81**, 1057–1074.
Percival, D.B. & Walden, A.T. (1993) *Spectral Analysis for Physical Applications*. Cambridge University Press, Cambridge.
Pesaran, B., Pezaris, J.S., Sahani, M., Mitra, P.P. & Andersen, R.A. (2002) Temporal structure in neuronal activity during working memory in macaque parietal cortex. *Nat. Neurosci.*, **5**, 805–811.
Pipa, G., Wheeler, D.W., Singer, W. & Nikolić, D. (2008) NeuroXidence: reliable and efficient analysis of an excess or deficiency of joint-spike events. *J. Comput. Neurosci.*, **25**, 64–88.
Raju, N.S. & Brand, P.A. (2003) Determining the significance of correlations corrected for unreliability and range restriction. *App. Psychol. Meas.*, **27**, 52–71.
Roelfsema, P.R., Engel, A.K., König, P. & Singer, W. (1997) Visuomotor integration is associated with zero time-lag synchronization among cortical areas. *Nature*, **385**, 157–161.
Runyon, R.P. & Huber, A. (1980) *Fundamentals of Behavioral Statistics*. Addison-Wesley Publishing Company, Reading, MA.
Sandberg, J. & Hansson, M. (2006) Coherence estimation between EEG signals using multiple Window Time-Frequency Analysis compared to Gaussian Kernels. *Proceedings of European Signal Processing Conference*, September 4–8. Florence, Italy.
Schneider, G. & Nikolić, D. (2006) Detection and assessment of near-zero delays in neuronal spiking activity. *J. Neurosci. Methods*, **152**, 97–106.
Schneider, G. & Nikolić, D. (2008) A stochastic framework for the quantification of synchronous oscillation in neuronal networks. *Proceedings of the Fifth International Workshop on Computational Systems Biology*. WCSB, Leipzig, Germany, pp. 169–172.
Schneider, G., Havenith, M.N. & Nikolić, D. (2006) Spatio-temporal structure in large neuronal networks detected from cross-correlation. *Neural Comput.*, **18**, 2387–2413.
Silver, N.C. & Dunlap, W.P. (1987) Averaging correlation coefficients: should Fisher's z transformation be used? *J. Appl. Psychol.*, **72**, 146–148.
Staude, B., Rotter, S. & Grün, S. (2008) Can spike coordination by differentiated from rate covariation? *Neural Comput.*, **20**, 1973–1999.
Toothaker, L.E. (1993) *Multiple Comparison Procedures*. Sage University Inc., Newbury Park, CA.
Zeitler, M., Fries, P. & Gielen, S. (2006) Assessing neuronal coherence with single-unit, multi-unit, and local field potentials. *Neural Comput.*, **18**, 2256–2281.

Appendix A: Fisher's *z*-transformation of *r*-values

To average the values of r by using Fisher's z-transformation, each r is first converted into a Fisher's z, denoted as z' (Fisher, 1915), by computing the inverse hyperbolic tangent

$$z' = \operatorname{arctanh}(r) = 1/2[\ln(1+r) - \ln(1-r)] \qquad (A1)$$

where ln is a logarithm with natural base e. Note that if $r = 1$ or $r = -1$, z' cannot be computed. After the transform, the values of z' can be averaged and the result, $\bar{z}'$, can be converted back to r by computing the hyperbolic tangent

$$r_z = \tanh(\bar{z}') = \left(e^{2\bar{z}'} - 1\right) / \left(e^{2\bar{z}'} + 1\right) \qquad (A2)$$

Note that Fisher's z-transformation is not the same as the standard z-score although both traditionally use the same symbol (z) to indicate the respective values.

Appendix B: calculating Pearson's coefficients of correlation for different types of signals

Pearson's r between variables x and y is defined theoretically as the product moment correlation, which for a sample is computed as follows

$$r = \frac{\Sigma z_x z_y}{N-1} \qquad (B1)$$

where N indicates the number of measurements and z is the standard score (z-score) for each measurement (not a Fisher's transform). Thus, Pearson's r is a measure of correlation normalized to a unit variance, and its square (r^2) can be interpreted as the proportion of variance explained in one variable by knowing the value in another variable. Other formulas are used for the computationally efficient calculation of r.

Continuous signals

For pairs of continuous signals, such as LFP or electroencephalogram, the following equation can be used to compute r quickly

$$r = \frac{N\sum xy - (\sum x)(\sum y)}{\sqrt{N(\sum x^2 - (\sum x)^2)N(\sum y^2 - (\sum y)^2)}} \qquad (B2)$$

where x and y are the raw measurements of electric potentials for the two variables and N is the number of measurements used to compute r. For example, if the scale $s = 50$ ms and the sampling rate of the continuous signal is 1 kHz (i.e. 1 measurement/ms), there will be a total of $N = 50$ measurements for each r. Thus, prior to applying the equation, one needs to make one run through the data set (e.g. one 'for' loop) and compute five sums: Σx, Σy, Σx^2, Σy^2 and Σxy. If the measurements are given as integers, the calculation will be faster if: (i) these sums are also computed with integer arithmetic (type 'long' should be used) and (ii) floating point operations are then used only for the final calculation of Eqn B2. In MATLAB, function 'corr(X)' can be used to compute Pearson's coefficient of correlation.

Binary signals

For binary signals, such as the time stamps of action potentials (spikes), the version of Pearson's r known as the phi (φ) coefficient of

correlation (Kuo, 1930) should be used. The phi coefficient of correlation is mathematically equivalent to Pearson's r but the calculation is optimized for the use of dichotomous and nominal variables. The calculation assumes that data are organized into time bins, each bin having a short duration (e.g. 1 ms) and containing either a 0 or 1, indicating the absence or presence of an event, respectively (e.g. an action potential). For larger time bins (e.g. 5 ms), multiple action potential events can occur within a single bin, in which case only one of them can be counted (i.e. the values cannot exceed 1). The calculation of φ begins with a count of coincident spikes, b, coincident lack of spikes, c, bins with spikes only in one variable, a, and only in the other variable, d, which can be shown as a contingency table (Table B1).

TABLE B1. Contingency table for the computation of the φ coefficient of correlation between two binary variables X and Y

Y/X	0	1	Totals
1	a	b	$a + b$
0	c	d	$c + d$
Totals	$a + c$	$b + d$	N

A value of 1 indicates the presence of at least one event (e.g. action potential) in a given bin (e.g. 1 ms size) and a 0 indicates the absence of the event. The count of coincident events is given by value b, whereas c represents the number of time bins in which no events occurred in either of the two signals, and a and d give the counts of events that did not have a coincident counterpart in the other respective signal. The coefficient φ is computed by entering the values $a - d$ into Eqn B3.

After the frequencies $a - d$ are determined, φ is computed by the following formula

$$\phi = \frac{(bc - ad)}{\sqrt{(a+b)(c+d)(a+c)(b+d)}}. \qquad (B3)$$

Here we provide an example of the calculation of the φ coefficient of correlation for a short segment of data with ten bins and two spikes in each signal. In this example, only one coincident event occurred (shown in Fig. B1).

Fig. B1. Two example spike trains with two action potentials each. r

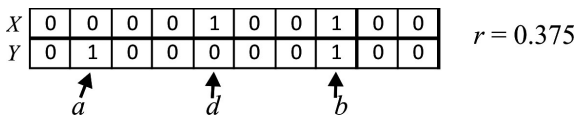

indicates Pearson's coefficient of correlation computed with Eqn B2. The bins counted for values a, b and d are indicated by arrows. All other bins count for the value of c.

The counts in the contingency Table B1 are as follows

Y/X	0	1	Totals
1	1	1	2
0	7	1	8
Totals	8	2	10

By using Eqn B3, this leads to the following calculation of the phi coefficient of correlation

$$\phi = \frac{7 - 1}{\sqrt{2 \cdot 8 \cdot 2 \cdot 8}} = \frac{6}{\sqrt{256}} = 0.375.$$

Combination of continuous and binary signals

Finally, for correlation between one continuous variable, x, and one binary variable, a form of Pearson's r known as the point-biserial coefficient of correlation should be used. This coefficient is computed most efficiently by the following equation

$$r_{PB} = \frac{(x_1 - x_0)\sqrt{P(1-P)}}{S_x}, \qquad (B4)$$

where x_1 and x_0 indicate the averages for the continuous variable in cases where the binary variable had the values 1 and 0, respectively, P is the probability that a value of 1 will be observed in the binary variable, and S_x represents the population standard deviation for the continuous variable. Note that

$$P(1 - P) = (n_1 n_0)/n^2, \qquad (B5)$$

where n_1 and n_0 indicate sample sizes (counts) for x_1 and x_0, respectively, such that $n = n_1 + n_0$. This equation can be used to correlate continuous signals such as LFP or electroencephalogram to neuronal spiking activity. Note also that, when computed for all possible time offsets between target and reference, x_1 can be interpreted as the spike-triggered average of LFP (or electroencephalogram) and r_{PB} as the normalized spike-triggered average.

Spearman's rho

In cases in which the applicability of Pearson's r, which is a parametric method, is doubted, one possibility is to compute the non-parametric Spearman's rho (ρ) coefficient of correlation. This measure of correlation is a Pearson's r computed on ranked data instead of the original data. Thus, if data are first ranked with values $1 \ldots N$, where N is the number of data points, and if for each pair a difference in ranks, D, is computed, then Spearman's rho is given by

$$\rho = 1 - \frac{6 \sum_N D^2}{N^3 - N}. \qquad (B6)$$

The routines for the computation of SCA are freely available as a source code in C++, a dynamic-link library for Windows or a dynamic-link library specialized only for the Matlab environment (but also only for the Windows operating system). The package is downloadable from http://www.raulmuresan.ro/sources/corrlib/ and also contains the routines for the calculation of classical CCHs together with instructions on how to use the routines.

Appendix C: variance across the entire data set

Claim

If the segments are equal in length, the variance of the entire data set is larger than or equal to the arithmetic mean of the variances of the segments: $\mathrm{Var}_G \geq \mathrm{Var}_S$.

Proof

For any random variable x, the mean is the value around which the second moment of x is minimal (Kim, 1992; p. 224)

$$\frac{1}{N}\sum_i (x_i-\mu)^2 = \min . \quad (C1)$$

For K segments, each with L samples (bins), the variance of the entire data set is

$$\mathrm{Var}_G = \frac{1}{KL}\sum_{k=1}^{K}\sum_{l=1}^{L}(x_{kl}-\hat{\mu})^2, \quad (C2)$$

and that of a segment k is

$$\mathrm{Var}_S = \frac{1}{L}\sum_{l=1}^{L}(x_{kl}-\mu_k)^2, \quad (C3)$$

where $\hat{\mu}$ indicates the arithmetic mean of the entire signal and μ_k indicates the mean of the k'th segment. $\hat{\mu}$ will, by definition, be different to the means of the individual segments, k, i.e. $\hat{\mu} \neq \mu_k$ Therefore, it follows from Eqn C1 that the summands in $\sum_{k=1}^{L}$ in Eqn C2 will always be larger when computed with the mean of the entire signal, i.e.

$$\sum_{l=1}^{L}(x_{kl}-\hat{\mu})^2 > \sum_{l=1}^{L}(x_{kl}-\mu)^2,$$

leading to $\mathrm{Var}_G > \mathrm{Var}_S$.

Appendix D: scaled correlation and filtering of correlations

Consider two time series X and Y, defined as follows

$$X = X_s + X_f + X_n \quad (D1)$$

and

$$Y = Y_s + Y_f + Y_n \quad (D2)$$

where X_s represents a time series that is slowly oscillating in amplitude (slow component), X_f is a time series that oscillates much faster than X_s (fast component), X_n is the noise, X_s, X_f and X_n are assumed to be mutually independent and Y_t is similarly defined as the summation of the three independent components Y_s, Y_f and Y_n. Also, in line with the conventions for computing cross-correlograms and given that we are interested primarily in time-averaged results, all of these time series are assumed to be homogeneous.

The cross-correlation between X and Y is by definition

$$\begin{aligned} E(XY) =& E((X_s+X_f+X_n)(Y_s+Y_f+Y_n)) \\ =& E(X_sY_s+X_sY_f+X_sY_n+X_fY_s+X_fY_n+X_nY_s+X_nY_f \\ &+X_nY_n+X_fY_f), \end{aligned} \quad (D3)$$

where E denotes the expected value.

The goal is to isolate the cross-correlation of the fast component, i.e. $E(X_fX_f)$.

Using Eqn D3, it can be written

$$\begin{aligned} E(X_fY_f) = E(XY) - E(&X_sY_s + X_sY_f + X_sY_n + X_fY_s \\ &+ X_fY_n + X_nY_s + X_nY_f + X_nY_n). \end{aligned} \quad (D4)$$

Assuming that the noisy processes X_n and Y_n have a mean of zero, Eqn D4 can be simplified into

$$\begin{aligned} E(X_fY_f) =& E(XY) - E(X_sY_s + X_sY_f + X_fY_s) \\ =& E(XY) - (E(X_sY_s) + E(X_s)E(Y_f) + E(X_f)E(Y_s)). \end{aligned} \quad (D5)$$

For the cases in which $E(X_s)$ and $E(Y_s)$ are of a moderate magnitude and $E(X_f) << 1$ and $E(Y_f) << 1$, the magnitude of the negative term in Eqn D5 is determined mainly by $E(X_fX_f)$, which is the cross-correlation between the slow processes X_s and Y_s.

It follows that the center bin of the classical cross-correlogram of the fast component is estimated as

$$E(X_fY_f) = E(XY) - X(X_sY_s) - \epsilon, \quad (D6)$$

where ε is zero if X_s is independent of Y_f, X_f is independent of Y_s, and the means of X_f and Y_f are 0.

Implicitly, scaled correlation estimates and subtracts a normalized form of the term $E(X_fY_f)$ from Eqn D6, which can be shown in the following way.

We first show that scaled correlation can be expressed in terms of a subtraction of the expected product between the means of the segments, $E(\mu_f\mu_f)$, from the classical cross-correlation.

Equation 8 from the main text can be linked to the average of correlation coefficients if the following is considered

$$\begin{aligned} \overline{r_s} =& \frac{1}{K}\sum r_k = \frac{1}{K}\sum_k \frac{E[(X_k-E(X_k))(Y_k-E(Y_k))]}{\sigma_{xk}\sigma_{yk}} \\ =& \frac{1}{K}\sum_k \frac{E(X_kY_k)-E(X_k)E(Y_k)}{\sigma_{xk}\sigma_{yk}}, \end{aligned}$$

where X_k represents the time series of the k-th segment (ranging between 1 and K).

Next, assuming that X and Y have the same variance across all segments, it follows that

$$\begin{aligned} \overline{r_s} =& \frac{1}{\sigma_x\sigma_y}\frac{1}{K}\sum_k [E(X_kY_k)-E(X_k)E(Y_k)] \\ \approx& \frac{1}{\sigma_x\sigma_y}(E(XY)-E(\mu_x\mu_y)), \end{aligned} \quad (D7)$$

where μ_X is the mean of segments of X.

Equation D7 states that, by calculating correlations on short segments for time series X and Y, scaled correlation in effect also computes the expected values for the product between μ_X and μ_Y, i.e. $E(\mu_x\mu_y)$. The averages μ_X and μ_Y are computed for each consecutive segment, and have $n = N/K$ sampling points (a positive integer; $s = n$*bin size), N being the total length of X and Y in sampling points ($t = N$*bin size), and K being the number of segments.

We next show that the subtraction of $E(\mu_x\mu_y)$ is an approximation of the $E(X_sY_s)$, and a part of this approximation is a procedure that acts as a moving average filter with low-pass properties.

Low-pass filtering is defined as a filter that passes low-frequency signals and attenuates signals with high frequencies, which can be achieved by calculating a moving average. For each data point, the moving average is computed by averaging the values of several neighboring data points, which is called the window of moving average, the size of which is given by the total number of averaged data points, d. Typically, the moving average is computed by sliding the window by a step of one data point, resulting in overlaps between subsequent window positions. In scaled correlation, due to the segmentation, the overlap is not necessary. It is sufficient to compute one average for each segment such that the length of the moving window, d, corresponds to the segment size, s.

To be precise, let us define X_c and Y_c as low-pass-filtered versions of X and Y by applying moving averages. Thus, μ_X and μ_Y are a sub-set of X_c and Y_c sampled at a constant interval, d.

It follows that the expectation of the product of the low-pass-filtered X and Y can be approximated, i.e. $E(X_cY_c)$ by the $E(\mu_x\,\mu_y)$.

The approximation error $|E(\mu_x\mu_Y) - E(X_cY_c)|$ is reduced 1when the segmentation length s reduces. Keep in mind that the length of this window also determines the properties of the low-pass filtering. Thus, the approximation error cannot be reduced without changing in the same time the cut-off frequency of the signal components that will be removed from the scaled correlation.

Finally, when s is equal to the total length of the signal, the term $E(\mu_x\,\mu_y)$ in Eqn D7 corresponds to the magnitude of the baseline of a normalized classical CCH, i.e. the product of the means of the X and Y. Therefore, a scaled cross-correlogram with s = data length will have a shape that is identical to that of the classical CCH, when the classical one is centered around zero after being corrected for the baseline.

Appendix E: conditions under which the average of segmented correlations equals non-segmented correlation

Claim

If the means and variances of signals are constant across all segments, the average scaled correlation obtained with small s is identical to the value of the single correlation coefficient computed across the entire signal (i.e. overall correlation determined with the maximum segment size, s).

Proof

Consider r computed across the entire pairs of signals x and y as the product moment correlation for population

$$r = \frac{\Sigma z_x z_y}{N}. \qquad (E1)$$

Note the division by N, rather than $N - 1$, which indicates the correlation estimate for the population. The standard score, z, is defined as

$$z = \frac{x - \mu}{\sigma},$$

where μ and σ indicate the mean and SD, respectively. If the signals are segmented and the mean and variance (i.e. σ^2) stay constant for each variable across all segments, correlation $\bar{r}$ averaged from r_1 to r_K can be written as

$$\bar{r} = \frac{\sum_{l=1}^{L} Z_{x_{1l}} Z_{y_{1l}} + \sum_{l=1}^{L} Z_{x_{2l}} Z_{y_{2l}} + \ldots + \sum_{l=1}^{L} Z_{x_{Kl}} Z_{y_{Kl}}}{KL} = \frac{\sum_{k=1}^{K}\sum_{l=1}^{L} Z_{x_{kl}} Z_{y_{kl}}}{KL}, \qquad (E2)$$

where indices $1\ldots K$ represent different segments and L is the number of measurements (bins) within a segment.

Following from the definition above, the value of the z-score does not depend on the actual number of segments, when μ and σ are constant across segments. For the correlations computed across the entire signal (Eqn E1), $N = KL$. Also, due to the consecutive segmentation of the signals, the nested sums over L and K can be expressed as a single sum over N. It follows that

$$\bar{r} = \frac{\sum_{n=1}^{N} Z_{xn} Z_{yn}}{N} \equiv r. \qquad (E3)$$

This concludes the proof.

To illustrate the applicability of this proof on binary signals, we give an example of two spike trains having in total $N = 21$ bins for which the correlation $\phi = -0.028$ (computed with Eqn B3). Each of the three segments has seven bins and the spike counts are the same across all segments, i.e. three and four spikes in all segments for the variables X and Y, respectively (Fig. E1). Equal spike counts make the means and variances equal across segments.

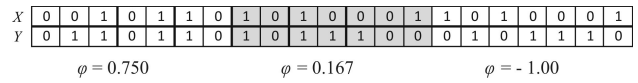

Fig. E1. Two hypothetical spike trains with different firing rates but with the same number of action potentials within each of the three segments. Segments are separated by the gray/white pattern. φ-values indicate correlation coefficients computed within each segment.

Correlations computed for each segment are different as they depend on the number of coincident events (3, 2 and 0 in the present example). Nevertheless, the average of these correlations, $\bar{\phi} = (0.75 + 0.167 - 1.0)/3 = -0.028$, is identical to that computed for the entire stretch of data.

Implications for Fisher's *z*-transformation

When Fisher's z-values are computed for the summands, Eqn E2 no longer applies and, thus, the identity Eqn E3 no longer holds. Foremost, Fisher's z-transformations cannot even be computed for the above example due to $\varphi = -1.0$ for which the transformation cannot be made. When the calculations were made for only the first two segments in which the correlations were suitable for Fisher's z-transformation, the 'corrected' average was $\bar{\phi} = 0.516$. This value was different from the single correlation coefficient computed across the two segments, $\varphi = 0.458$. Therefore, Fisher's z-transformation cannot be used with binary signals.

Appendix F: estimating the significance of *r*-values

Sometimes it is necessary to estimate whether a correlation coefficient obtained from SCA is significantly different from a zero correlation. The significance of a phi coefficient of correlation, which is based solely on binary signals, is usually determined by computing a chi-square test (e.g. Runyon & Huber, 1980). The significance of a coefficient of correlation that includes at least one continuous variable (hence including the point-biserial coefficient of correlation) is based on the Student's t-distribution. The t-value can be computed from r as follows

$$t = \frac{r}{\sqrt{\frac{1-r^2}{N-2}}}, \qquad (F1)$$

and is distributed with $N - 2$ degrees of freedom. N indicates the number of samples, which, in the case of spiking signals, corresponds to the number of bins. For example, with a 1 kHz sampling rate of the signal (1 ms bin), $r = 0.50$ is significant with $N = 12$ and 22 at $\alpha = 0.05$ and 0.01, respectively (t-values = 1.83 and 2.58, respectively; one-tailed test). With a 1 ms bin size, this amounts to a duration of segments of only 12 or 22 ms. Equation F1 should not be used for $N < 6$ as the estimates become inaccurate. High accuracy may be achieved with $N \geq 60$ (Millsap, 1988, 1989). For binary signals, the correlations are typically much smaller and will require longer stretches of signal to reach significance.

Significance of average correlations

Due to the nature of scaled correlation, it is necessary to compute the significance of an average of correlation coefficients rather than that of a single coefficient. For testing the significance of $\bar{r}$, we propose the method of fixed effects of Hedges & Olkin (1985) developed for testing the significance of average correlation coefficients in meta-studies. According to Hedges & Olkin (1985) (see also Field, 2001), the SE of the average correlation coefficient can be estimated from the number of estimates of r used to compute the average, which corresponds to the number of segments, K, and from the sample size for each r, which corresponds to the number of samples (bins) within each segment, L. Hence, the SE is given by

$$\mathrm{SE}(\bar{r}) = \sqrt{\frac{1}{K(-3L)}}. \qquad (F2)$$

The likelihood of obtaining the given $\bar{r}$ by chance is then obtained simply from the following z-score

$$z_{\bar{r}} = \frac{\bar{r}}{\mathrm{SE}(\bar{r})}. \qquad (F3)$$

For example, for $K = 400$ segments and for 25 samples in each segment (e.g. $s = 25$ ms with a 1 kHz sampling rate; a total of 10 s of signal), the SE is

$$\mathrm{SE}(\bar{r}) = \sqrt{\frac{1}{1000(22)}} = 0.01066,$$

which, even for a very small $\bar{r} = 0.05$ leads to a z-score = 4.69 and a highly significant value of $P = 1.36 \times 10^{-6}$.

However, with spiking signals these significances will be smaller because usually only a portion of segments contain spikes for both neurons and, thus, only a portion of segments will be taken into analysis. For example, with a firing rate of 10 spikes/s and with the assumption of independence between the neurons, it is expected that only 15 segments out of 40 (37.5%) will be valid. Equations F2 and F3 lead to $\mathrm{SE}(\bar{r}) = 0.0714$ and, for the same $\bar{r} = 0.05$, to $P = 0.002$ (z-score = 2.87).

Controlling for multiple comparisons

The next step is to control the type I error in statistical inference, which is the problem of false-positive detection of significant correlations. When computing CCHs, this can lead to a considerable problem due to the large number of estimates made across different offsets in each CCH. For example, if two signals are not correlated, and the significance is tested at $\alpha = 0.01$ for $m = 161$ correlations (±80 ms shift with 1 ms binning plus the center bin), it is expected that in $p(m) = 1 - (1 - \alpha)^m = 0.80$ or in 80% of cases at least one bin will nevertheless be significant. Thus, without a correction, a researcher is in danger of concluding incorrectly that, at some time delay, the two variables are correlated.

A number of correction methods have been proposed for similar problems with multiple comparisons in which one can, for example, reduce the critical α value (see e.g. Toothaker, 1993). We propose here a correction method that is suitable for the large number of estimates made typically in a CCH and for the studies in which correlation peaks of interest are wider than the binning resolution of the CCH, as is usually the case. This correction procedure requires that a peak is considered significant only if at least three neighboring peaks are found to be significant by a standard, not corrected, test.

This requirement that three neighboring, i.e. consecutive, bins are significant controls well the probability of making a type I error in statistical inference. For our example with nominal $\alpha = 0.01$ for $m = 161$ correlation bins, the probability that any combination of three bins will be significant by chance already reduces from 80% to $p(m)*p(m-1)*p(m-2) = 0.51$ or 51%. When it is required that the three bins are neighbors, the conditional probability of corrected alpha decreases to $\alpha_{\mathrm{CORR}} = p(m)*\alpha^2 = 0.00008$. With the nominal $\alpha = 0.05$ this requirement leads to $\alpha_{\mathrm{CORR}} = 0.0025$ and with the nominal α-value relaxed further to 0.10, $\alpha_{\mathrm{CORR}} = 0.01$. Therefore, if three neighboring bins are significant (and the correlations point to the same direction), we can accept the significance of the peak confidently because the likelihood of making a type I error is small.

Finally, it is important to note that it will not always be necessary to compute the significance for individual CCHs. In many studies, the significance tests are made by pooling a number of CCHs obtained from different pairs of units and/or different subjects. Comparisons are then made across, for example, different experimental conditions (e.g. Biederlack *et al.*, 2006). Here, the sample size is defined by the number of pairs of units investigated, and the properties of such correlation estimates (e.g. their distributions) usually allow for the application of standard parametric statistics such as ANOVA. These latter types of tests are also often more desirable as they allow the researcher to generalize to the entire population rather than being limited to a conclusion about a single pair of units, as is necessarily a limitation of a significance test of an individual CCH.

Chapter 4 - Gamma-band synchrony may be responsible for plasticity in visual cortex.

Gamma-band synchrony may be responsible for plasticity in visual cortex

Feng W.[1,2,3], Vicente R.[1,2,3], Singer W.[1,2,3], Nikolić D.[1,2,3]

[1] Max-Planck Institute for Brain Research, 60528 Frankfurt am Main, Germany

[2] Frankfurt Institute for Advanced Studies, 60438 Frankfurt am Main, Germany

[3] Ernst Strüngmann Institute for Neuroscience in Cooperation with Max Planck Society, 60528 Frankfurt am Main, Germany

Correspondence:

Danko Nikolić, Ph.D.

Department of Neurophysiology,

Max-Planck Institute for Brain Research,

Deutschordenstr. 46,

D-60528 Frankfurt am Main,

Germany

Tel.: +49 69 96769 736

Fax: +49 69 96769 327

E-mail: danko.nikolic@gmail.com

Abstract

Synaptic modification mediated by Spike Timing Dependent Plasticity (STDP) is induced by synchronous pairing of pre- and post-synaptic spikes. Currently, not much is known about the role of gamma-band synchrony in the process of STDP. Here, we employed analytical and experimental methods to characterize the evolution of STDP in synchronized spike-trains. Based on a mathematical analysis of random walk for phenomenological STDP models, we found that the synaptic modification at equilibrium should change as a function of the strength of synchrony and of the time delay between the pre- and post-synaptic spikes. Similar result was found by feeding spike trains recorded from visual cortex of anaesthetized cats to a more realistic STDP model. We therefore conclude that the modification of synaptic gains in the cortex is closely related to gamma-synchronization between neurons.

Key words: spike timing dependent plasticity, random walk, synchrony, relative firing times, suppression model, gamma-oscillations

Introduction

Synchrony has been studied traditionally in the context of phenomena other than plasticity such as the selective attention (Fries et al., 2001; Womelsdorf and Fries 2006; Fan et al., 2007; Doesburg et al., 2008), perceptual grouping (Gray et al, 1989; Kreiter and Singer 1996) and multisensory integration (Lakatos et al., 2007). The reason that the relation between cortical plasticity and synchrony has not been in the focus of investigations was probably the broadly held opinion that, in the cortex synchrony, occurs predominantly with zero or near-zero delays (Roelfsma et al, 1997). However, recent studies have revealed that delays between neuronal activities synchronized in the gamma band are rarely zero but typically extend to several milliseconds, up to about 10-20 ms (Havenith et al., 2011; Schneider et al., 2007; Nikolić 2007; Schneider and Nikolić, 2006; König et al., 1995). This range is relevant for inducing STDP, as initially reported e.g. by Markram et al (1997).

Activity-dependent synaptic plasticity has been established as an essential component of several forms of learning and memory (Atonov et al., 2001; Tasanov and Manahan-Vaughan, 2007). The exact aspects of neuronal activity that determine synaptic potentiation and depression are still under research (Zucker, 1999; Rebola et al., 2010). Nevertheless, so far, it has been established that rate of discharge, level of depolarization and relative spike timing of neurons are major contributors to the calcium influx into the post-synaptic cells, which in turn trigger cascades of biochemical events leading to the strengthening and weakening of synapses (Caporale and Dan, 2008; Citri and Malenka, 2008). In particular, the sensitivity of synapses to relative spike-timing of neurons (a proxy for their cross-correlation) underlies implementation of a causal Hebbian learning rule: in the pioneering work of Markram and colleagues (1997), and of Bi and Poo (1998), the significant modification of the synapse was induced by specific pairing the excitatory post-synaptic potentials (EPSP) of the pre-synaptic

neuron on one side and the action potential (AP) of the post-synaptic neuron on the other side. Potentiation is achieved when EPSP precedes AP (a positive interval) and depression is produced when AP is generated prior to a buildup of EPSP (a negative interval). Thus, these studies demonstrated that synaptic modification is a result of correlated pre- and post-synaptic activities. In contrast, plastic modification of a synapse is absent or much weaker when the pre- and post-synaptic activities are uncorrelated (Jacob et al., 2007). Correlations in spiking activity are often referred to as neural synchrony, a phenomenon that is associated with delays in spike timing of the order of magnitude that does not exceed 15 or 20 ms (König et al., 1995; Nikolić 2007; Schneider and Nikolić, 2006; Schneider et al. 2006; Havenith et al, 2011; Wang et al. 2010).

The present study is motivated by the potential impact that gamma-band synchrony of neuronal discharges may exert on changes of synaptic strengths via STDP. First, we exploit the simplicity of an analytical model of STDP to derive theoretical predictions on the evolution of the synaptic strengths as a function of synchronicity between neuronal discharges. Second, we apply a phenomenologically-derived STDP rule (Froemke and Dan, 2002) to the timings of action potentials within the spike trains recorded from cortical area 17 of anesthetized cat. Given the synchronicity of the recorded spike trains, we investigate the putative modifications of synaptic strengths between pairs of recorded cells. In particular, we characterize how the synaptic changes may depend on the strength of synchronicity and oscillatory activity in the gamma range, and how this processes may be affected by the optimality of the visual stimulus.

The analytical model under study is motivated by the fact that the evolution of the synaptic weights under STDP conditions has stochastic components. Based on the experimental methods for inducing synaptic modifications, simplifications of the of the STDP rule have

been proposed by describing it as a random walk process (Kempter et al,1999; Williams et al., 2003; Elliot 2010). For this random walk, the synaptic weight increases at the time a post-synaptic spike fires, and it decreases when a pre-synaptic spike fires (Morrison et al. 2008). The amount of drift in the walk is determined by three factors: the learning rate, the update function, and most importantly, the timing relationships of the pre- and post- synaptic spikes. Essentially, given that the spiking processes are only statistically describable, the amount of drift in any particular case will be a random variable. Rubin et al (2000) discussed the solution of this random walk using the Fokker-Planck Equation (FPE). Cateau and Fukai et. al (2003) provided a more detailed investigation using FPE based on various simplifications. The first simplification was that a pre-synaptic spike is only paired with the preceding and the immediately following post-synaptic spike (Froemke and Dan, 2002). However, as has been shown, pre- and post-synaptic spikes can be paired in multiple ways and each pair can contribute to the drift of the synaptic weight. Hence, in general, more elaborated time relationships between spikes should be considered.

It is important to note that, to induce STDP, the relative timing of spikes needs to be evaluated at the post-synaptic dendrites (Bi and Poo 1998, Froemke and Dan 2002), usually via NMDA receptors (Morrison et al., 2008). Thus, in addition to knowing the time of spike-generation at the axon hillock one needs to consider the delays associated with spike propagation to the location at which the coincidence detection of pre- and post-synaptic events takes place. The magnitudes of axonal and dendritic propagation delays generally depend on the type of the neuronal fibers and their physical lengths. The sum of the two can range from a few milliseconds, for short-range axons, to several tens of milliseconds, for un-myelinated or particularly long fibers (Swadlow et al., 1980).

The relative timing of the spikes created by a given pair of interconnected neurons is not constant. The expected lags of spike firing between synchronized neurons can change not only magnitudes but also signs, i.e. directions, which are determined by the properties of the stimulus (König et al., 1995; Havenith et al., 2011). Thus, the relative timing of spike generation between cells is determined not only by their anatomical properties, but also by functional variables such as the position of the stimulus relative to the receptive fields of neurons. These studies suggest that the firing-time intervals between neuronal discharges: 1) contribute significantly to the STDP random walk, and 2) do so in a stimulus-dependent manner.

In the first, analytical, part of the present study we analyze the STDP random walk as a causal discrete process (Morrison, 2008). We emphasize the predicting role of cross-correlation on the spike-timing in the STDP random walk. To gain theoretical insight, we consider a simple model only of the homogeneous Poisson spiking process for which analytical computations are presented only for the first and second moments of the evolving synaptic weights. When possible, we generalize the model to special cases of inhomogeneous processes. In the second, computational part of the study, we apply a more complex, empirically established STDP rule (Froemke and Dan, 2002) to pairs of spike trains recorded in response to grating stimuli drifting in different directions. We describe how the putative synaptic changes between pairs of neurons depend on oscillatory and synchronous activity as well as on the optimality of the directions of grating stimuli.

Methods

Surgical procedures

In one male adult cat, anesthesia was induced with a mixture of ketamine (Ketanest; Parke-Davis; 10 mg/kg, i.m.) and xylazine (Rompun; Bayer; 2 mg/kg, i.m.). After tracheotomy, anesthesia was maintained with 70% N_2O and 30% O_2, supplemented with ~ 1.0% halothane. After craniotomy, the level of halothane was reduced to ~ 0.5%. When anesthesia was stable and sufficiently strong to prevent any vegetative reactions, the animal was paralyzed with pancuronium bromide applied intravenously (Pancuronium; Organon; 0.15 $mg \bullet kg^{-1} \bullet h^{-1}$). The respiration rate was adjusted manually to keep end-tidal CO2 at 3– 4%. Rectal temperature was kept at 37–38°C. Glucose and electrolytes were supplemented intravenously. All procedures complied with the German law for the protection of animals and were overseen by a veterinarian.

Data acquisition

Recordings were acquired from area 17 using silicon-based 16-site probes supplied by the Center for Neural Communication Technology at the University of Michigan as described previously in Biederlack et al. (2006). The electrode contacts (recording sites) had an impedance of 0.3– 0.5 MΩ at 1000 Hz and were organized in a 4 × 4 matrix on four shanks, with a distance of 0.2 mm between the neighboring contacts. Thus, the recording area of one probe spanned ~ 0.6 × 0.6 mm. The probes were carefully placed to enter the cortex at a 90° angle (i.e., perpendicularly to the surface of the cortex), and the uppermost row of electrode contacts was lowered 100 –200 µm below the cortex surface. Thus, the same probe recorded neurons from different layers and different orientation columns.

Signals were amplified 1000 ×, filtered at 500 Hz to 3.5 kHz, and sampled with a frequency of 32 kHz. Action potentials (spikes) were detected with a two-sided threshold discriminator adjusted manually to yield a signal-to-noise ratio of > 2:1. For each detected action potential,

the time of the event was recorded together with the spike waveform over a duration of 1.2 ms. Single-unit activity was then extracted off-line by spike sorting. The distance between neighboring electrode contacts was sufficient to prevent them from recording activity of the same neuron—in no case did cross-correlation histograms (CCHs) show the high, narrow peaks in the very center of the CCH characteristic of autocorrelations. Thus, spike sorting was applied to the signals from each recording site separately. Spike waveforms were sorted using Principle Component Analysis (PCA) according to the following two criteria: (1) waveform separation: the shape of the spike waveforms should be clearly defined and different from all other waveforms in the multiunit (MU), as indicated by the first three PCA components; (2) refractory period: not more than 0.5% of spikes should occur with an inter-spike-interval of < 1 ms.

Visual stimulation

Visual stimuli were presented on a 21-inch Hitachi CM813ETPlus monitor with a refresh rate of 100 Hz, positioned at a distance of 57 cm from the eyes. Stimuli were always presented binocularly, using the presentation software ActiveSTIM (www.ActiveSTIM.com). The pupils were dilated with atropine, the nictitating membrane retracted with neosynephrine and the cornea protected with contact lenses containing artificial pupils of 2 mm diameter. After refraction, the eyes were focused on the monitor with correcting lenses. The optical axes of the two eyes were aligned by mapping the receptive fields (RFs) for each eye separately and placing a prism in front of one eye to achieve binocular fusion of the RFs. All RFs were determined by manual mapping with high-contrast white bars on a black background. Because of the spatial proximity between electrode contacts, the RFs recorded from one probe always overlapped, producing clusters that spanned up to ~ 10° of visual angle. The stimuli were always positioned such that their centers matched the center of the RF cluster.

The visual stimuli consisted of high contrast (C = 0.94) sinusoidal gratings. The gratings moved orthogonally to their orientations in 12 different directions, equally dividing a 360° circle in 30° steps (0°, 30°, 60°, 90°, ... 330°). The spatial frequency, size and moving speed of the gratings were 2.4 °/cycle, 12° and 2 °/s, respectively. The receptive fields of the simultaneously recorded units always overlapped, producing clusters spanning up to ~10° of visual angle, over which the stimuli were centered. The gratings were presented for 4 s with an inter-stimulus interval of 1 s with their drift directions changing randomly. Gratings drifting in the same direction were shown 20 times. Thus, a recording block consisted of 240 stimulus presentations and lasted approximately 20 minutes. The recording blocks were repeated 4 times, within a time period spanning 21.6 hours.

Data analyses

Cross-correlograms

The cross-correlograms were calculated for the time period of 1.5 s to 4.5 s after the stimulus onset, with the lag ranging from -100 to 100 ms. To ease the later fitting procedures the raw cross-correlograms were smoothed by a moving average filter, described by:

$$\hat{y}_t = \frac{y_{t-1} + y_t + y_{t+1}}{3},$$

where y_t are the coincidence counts in the bins of the raw cross-correlogram, and $\hat{y}_t$ are those of the smoothed cross-correlogram. The smoothed cross-correlograms encompassed time lags ranging $-100 \leq t \leq 100$ ms, with 1 ms binning.

Gabor functions are fitted to the smoothed cross-correlograms for estimating the modulation amplitude (MA), relative firing time, and oscillation frequency. MA is defined as the length

of the central peak of the cross-correlogram divided by the sum of this length and the average magnitude of the baseline of the cross-correlogram (Biederlack et al., 2006). MA indicates how strongly the spike times of the neurons are synchronized. The relative firing time is estimated by measuring the time lag of the central peak for the cross-correlogram. The sign of the relative firing time reverses when a neuron assigned as pro-synaptic gets re-assigned as post-synaptic. A common oscillatory frequency of two units is captured by the periodicity exhibited by the cross-correlograms and is expressed in Hz.

Not all cross-correlograms had sufficient counts of coincident events to yield reliable estimates. The fit of a cross-correlogram was considered sufficiently good to warrant further analysis if the fit of Gabor function was sufficiently precise, that is if $r^2 \geq 0.8$.

Neurons in the visual cortex usually respond differently for the stimulus drifting in different directions. In order to quantify how optimal a particular stimulus was for evoking neuronal responses, we measured the difference in degrees between the orientation of the actual stimulus and the preferred orientation of that neuron. We define this difference as the Optimality Index (OI) for the stimuli.

Phenomenological model of STDP in cat visual cortex.

We used the suppression model of synaptic change established by Froemke and Dan (2002) to estimate the synaptic modification for the spikes recorded in anaesthetized cats. The spike data for the time period of 1.5 to 4.5s after the stimulus onset were used. To avoid making any assumptions about how the recorded neurons may be connected in reality, we marginalized over all possible connectivity patterns. Therefore, the estimated synaptic modification is a function of the spike times conditioned on an assigned pattern of connectivity. If not specified otherwise, each result is an average across 80 trials.

We analyzed the activity of 5 single-units in response to 12 stimulus conditions. Only the combinations of units for which the fitting of cross-correlogram was feasible were further analyzed. Overall, we analyzed 20 pairs of spike trains, which is a result of combing 5 single units recorded in 5 experimental conditions. Data from different experimental conditions are treated such that they are independent and comparable. For each pair of single units, there are two possible estimates of synaptic modifications, depending on which unit is assigned to be pre-synaptic and the other post-synaptic. This leads to a total of 40 estimations. From those 40 estimates, we randomly drew 20 and performed correlation analyses. Six variables were analyzed for the correlation, which are the putative synaptic modifications, the average firing rate, the relative firing time, the OI, the oscillation frequency and the MA. In total, 2^{20} numbers for correlations were calculated, covering each possible pattern of afferent-to-efferent connections.

Surrogates and numerical simulations of synaptic weights

Surrogate data to evaluate the statistical significance of cross-correlograms and effects of synchrony in the evolution of putative synaptic weights were produced by jittering the spike times. For each pair of pre- and post-synaptic spikes, the spike time of the post-synaptic neuron was shifted by an amount drawn randomly from a uniform distribution specified by the jitter interval (JI).

The inhomogeneous Poisson spikes used in the numerical simulations of the simplified STDP model are generated by a spike-thinning method (see Abort and Dayan 2001 for details). The same thinning method is applied for generating homogeneous Poisson spikes of reduced synchronicity. The difference in generating the inhomogeneous Poisson spikes and asynchronous homogeneous Poisson spikes is that for the latter, the intensity (i.e. the firing

rate) is time-invariant whereas for the former, the intensity is a function of time. The intensity of the inhomogeneous Poisson changes as a square-wave function, which alternates between values of intensity $r > 0$ and zero with a period of .05 seconds. For the numerical simulations, the firing rates of the neurons were set to 20 spikes per second. The range of the time kernel $K(s)$ for the STDP is set to [-50, 50] milliseconds. The learning rate, λ, is set to 0.01.

The suppression model and the saturation methods used for the evolution of the putative synapses between the measured units were implemented as described in the original papers (Froemke and Dan, 2002, 2006). The models were fed with the recorded spike trains in the total duration of 3 x 80 = 240 seconds per train, and an average of 64.8 ± 51.8 spikes per train (ranging between 1 and 377 spikes for a total of 20 trains, selected from 5 neurons x 12 stimuli = 60 trains with a criterion described earlier).

Results

Analytical predictions for a simplified STDP model

We implemented a model for the weight dynamics that simulates the classical STDP for the mono-synaptic connection between two excitatory neurons (Caporale and Dan, 2008). The model describes the updating of synaptic weights based on discrete pre-synaptic and post-synaptic events as follows:

$$w_{(t)} = \begin{cases} w_{(t-1)} - \lambda \alpha w_{(t-1)}^{\mu} F_d(t) & \text{when a pre-synaptic spike fires } (p_1) \\ w_{(t-1)} + \lambda \left(1 - w_{(t-1)}\right)^{\mu} F_p(t) & \text{when a post-synaptic spike fires } (p_2) \\ \text{sequential potentiation and depression} & \text{when post- and pre-synaptic spike fire simultaneously } (p_3) \\ w_{(t-1)} & \text{when no spike fires } (p_4) \end{cases} \quad (1)$$

where, $w_{(t)}$ is the synaptic weight, λ denotes the learning rate and α is the asymmetry factor. The exponent μ determines how the modification of plasticity depends on the weight. The update can either be additive or multiplicative, depending on whether μ is zero or one, respectively. μ can also range between zero and one to describe a mixed situation (Gültig et al., 2003). Importantly, the multiplicative updates fit better the weight-dependence of the STDP that has been observed experimentally (Morrison et al., 2006; Bi and Poo, 1998). Pure additive updates however cannot describe the effect of weights for drifts. The drift terms $F_p(t)$ and $F_d(t)$ denote the amount of raw potentiating and depressive modification respectively, and depend on the trains of pre- and post-synaptic spikes. $F_p(t)$ is calculated by summing the time kernels $K_p(s)$ evaluated at interval s_i over i and $F_p(t)$ is similarly defined, as follows:

$$F_p(t) = \sum_{s_i \in D_p(t)} K_p(s_i) \quad (1)$$

$$F_d(t) = \sum_{s_i \in D_d(t)} K_d(s_i) \quad (2)$$

$D_p(t)$ represents the set of interval(s) between a post-synaptic spike that fires at t and any pre-synaptic spike that interacts with the post-synaptic spike. $D_d(t)$ denotes similarly the set of intervals for a pre-synaptic spike at time t. Note that D_p and D_d can be empty sets. Besides, we assume that the overall plastic modification is simply the sum of modifications produced by individual pairs of pre- and post-synaptic spikes.

For the purpose of the present theoretical analysis, we choose a time kernel $K(s)$, which is representative for the STDP and yet easy to analyze. We require that $K(s)$ is linear and has a finite domain, which reflects the linear fit and the effective domain of the STDP. The range of $K(s)$ is set to (0, 1] as absolute values without losing generality. Thus, the kernel is described as:

$$K(s) = 1 - \frac{s}{b}, \quad (3)$$

where $b > 0$ is the slope parameter and $s \in (0, b]$. In practice, for the set of intervals $D(t)$ we only consider intervals that fall in the range $(0, b]$, since the intervals that are out of this range do not contribute to the results.

We characterize the random walk by considering a pair of synchronized Poisson arrival processes as pre- and post-synaptic spikes. One can solve a random walk defined in (1) for expected weight by conditioning on the number of intervals at a certain time in updates. We firstly consider the case where the update is multiplicative ($\mu = 0$) and the asymmetry factor is one ($\alpha = 1$). We then generalize the result to any α. The analysis of additive model ($\mu = 1$) is

less complicated than that of the multiplicative model and the results are qualitatively comparable across models in many aspects. Therefore, we report detailed discussion of the additive models in the Appendix. Fig. 1 shows a sample of such a random walk.

The updates of the random walk can be either homogenous or inhomogeneous. To determine homogeneity we define the transition probability, which is the probability that the synaptic weight will change in one step from one to another position in the state space. For the homogenous updates, the transition probability is time-invariant, whereas for the inhomogeneous updates this transition changes over time. We therefore study both cases and focus on the effects of synchronicity and relative firing times for the plastic modification of the synapses.

1. Homogenous processes

1.1 The mean synaptic weight

Based on the definition of the Eq. 1, one can estimate the expected value of the synaptic weight as a function of time. We show that the expected weight evolves as

$$E(w_t) = w_0 T_1^t + T_2 \left(\frac{1 - T_1^{t-1}}{1 - T_1} \right), \qquad (4)$$

where T_1 and T_2 are terms consisting of the expected amount of plastic modification and the probabilities of differentiated events (see Appendix for proofs). We considered the case in which the synchronicity between spike trains is perfect and the relative firing interval (or conduction delay) is such that the post-synaptic time stamps are a copy of pre-synaptic stamps shifted backwards or forward in time by a quantity t_0, ranging from 1 to b. Choosing t_0 such that post-synaptic spikes precedes pre-synaptic ones makes the modification of the synaptic

weights always depressive. We also refer to the quantity t_0 as relative firing time (RFT; Havenith et al., 2012). Finally, the factors T_1 and T_2 appearing in Eq. (5) read

$$T_1 = \left(1-\lambda E(F_d)\right) p_1 + \left(1-\lambda E(F_p)\right) p_2 + \left(\lambda E(F_p)\left(E(F_d)-1\right) - \lambda E(F_d) + 1\right) p_3 + p_4 , \quad (6)$$

$$T_2 = \left(p_2 + p_3\right) \lambda E(F_p) \ , \quad (7)$$

with

$$E(F_d) = \frac{t_0 (r-1)}{b} + \frac{r(B-3)}{2} + 1, \quad (8)$$

$$E(F_p) = \frac{r(b-1)}{2}. \quad (9)$$

Here, r is the intensity of the Poisson process from which we draw spikes. F_d and F_p represent the expected amount of depressive and potentiating modifications respectively. $E(F_d)$ and $E(F_p)$ can be calculated by plugging the stochastic inter-spike intervals into the time kernel (Eq. 4) and averaging. Note that when t_0 equals zero, $E(F_d)$ and $E(F_p)$ are identical, and thus indicating the expected result where neither potentiation nor depression occurs. In general, when the pre-and post- synaptic spikes are maximally synchronized, i.e, one set of spikes is a copy of the other but shifted in time, $E(F_d)$ will only depend on the time lag (RFT) and $E(F_p)$ will be a constant for a certain firing rate. This can also be observed by checking the cross-correlation for fully synchronized spikes.

The cross-correlation reflects the sample distribution of the inter-spike intervals for a pair of pre- and post-synaptic spikes (Kempter et al., 1999). For the cross-correlation of the fully synchronized spikes, the central peak is a delta function. It reflects the perfect correlation of a spike train with itself. As a result, the lag of the central peak reflects the amount of time by

which one spike train is shifted relative to the other. The flat flanks of the cross-correlation at either side the central peak are found when the inter-spike intervals are Poisson distributed. Thus, E(F_d) and $E(F_p)$ can be directly related to the cross-correlation (Fig. 3).

1.2 The mean synaptic weight at the equilibrium

In Eq. 6, the magnitude of p_4 (absence of pre- or post-synaptic firing), and not the rest of the terms, generally governs the range of T_1. This is because generally λ, p_1, p_2 and p_3 <<1. Therefore, at least for the typical parameters used presently, T_1 is positive and smaller than 1. This makes the sum of power series in Eq. 5 converge. The first term in Eq. 5 decays to zero as t increases, leaving the expected weight at equilibrium as the product of T_2. The estimates of the mean weight at equilibrium thus can be computed by truncating the sum of the power series at large t's. The estimates of expected weights around the equilibrium are shown in solid lines in Fig. 1.

1.3 The second moment of the synaptic weight

Analogous to the derivation of the mean synaptic weight, the second raw moment can be derived directly by considering the recursive updates of the weights. We found the second raw moments of the stochastic drift of weight as the following:

$$E(F_d^{\,2}) = \frac{1}{b^2}(r^2 - 3r + 1)t_0^{\,2} + (r^2 - \frac{3r^2 - 7r + 2}{b} - r)t_0 + \frac{1}{4}(b-3)^2 r^2 + \frac{1}{6}(8b + \frac{1}{b})r + 1 \quad (10)$$

$$E(F_p^{\,2}) = r^2 b^2 (1 + \frac{(1+b)^2}{4}) + r[\frac{(b+1)(2b+1)b}{6} - 1] \quad (11)$$

Next, to make the subsequent analyses more tractable, we approximate the iterations described in 1 by dropping the third case. This is justified because the probability of coincident pre-and post-synaptic spikes is very small when the firing rates are low.

Using the quantities listed above, the second raw moment of the evolving synaptic weight reads:

$$E(w_t^{\,2}) = p_2 r(2(E(F_p) - rE(F_p^{\,2}))\cdot\overrightarrow{Ew} + rE(F_p^{\,2})\cdot\vec{t})\cdot\vec{S}^{T} + S^{t}w_0^{\,2} \tag{12}$$

where $\overrightarrow{Ew}$ represents the expected weights in a vector form, $\vec{t}$ is a vector with *t* entries filled with the number 1, and $\vec{S}$ is a vector containing successive powers of a function which involve the first two raw moments of the stochastic drifts. Mathematically,

$$\overrightarrow{Ew} = [E(w_0) \quad E(w_1) \quad ... \quad E(w_{t-1})] \tag{13}$$

$$\vec{t} = [1 \quad 1 \quad ... \quad \text{t ones}] \tag{14}$$

$$S = p_1(\lambda^2 E(F_d^{\,2}) - 2\lambda E(F_d) + 1) + p_2(\lambda^2 E(F_p^{\,2}) - 2\lambda E(F_p) + 1) + p_3 \tag{15}$$

$$\vec{S} = [S^{t-1} \quad S^{t-2} \quad ... \quad S^{0}] \tag{16}$$

Having found the first two moments of the evolving synaptic weight, the variance can be easily specified. The variance of the evolving synaptic weight informs about the variability of the synaptic weight against different realizations of the pre- and post-synaptic spike trains. As we have seen, this can be predicted from the basic properties of the Poisson process and the weight drifts.

1.4 Partially synchronous pre-and post-synaptic spikes

To study the role that partial synchrony plays in the evolution of the weight we considered processes in which a given amount of jitter is added to an otherwise perfect (although possibly time lagged) synchronization of pre- and post-synaptic spike trains. The discrete uniform interval from which the amount of jittering is drawn is defined as [-*JI*, *JI*]. In a similar manner as in the analysis of the previous sections, we insert the expected sum of intervals of jittered spikes (22, 23) to the time kernel for estimating the stochastic drift of jittered spikes

$$E(F_d)=\begin{cases}\dfrac{JI+t_0}{2JI+1}[\dfrac{JI+t_0+1}{2b}-1](r-1)+\dfrac{r(b-1)}{2} & JI\geq t_0\\ \dfrac{t_0(r-1)}{b}+\dfrac{r(b-3)}{2}+1 & JI<t_0\end{cases} \tag{17}$$

$$E(F_p)=\begin{cases}\dfrac{JI-t_0}{2JI+1}[\dfrac{JI-t_0+1}{2b}-1](r-1)+\dfrac{r(b-1)}{2} & JI>t_0\\ \dfrac{r(b-1)}{2} & JI\leq t_0\end{cases} \tag{18}$$

For the partially synchronous case one can derive the expected weight at the equilibrium as well as the variance of the synaptic weight as a function of the jittering level. These computations are detailed in the accompanying Appendix. The cross-correlation function is particularly informative for analyzing the plastic modification induced by partially synchronous spike trains as mimicked by spike jittering. Such spike trains are often taken as surrogate data for evaluating the role of synchrony in various studies (Grün and Rotter, 2010).

The cross-correlogram for the jittered spikes has a box-shaped central peak, in contrast to the delta-shaped central peak for the cross-correlation of the fully synchronized spikes. The amount of jitter variance determines the width of the central peak. When the jitter variance is large enough, central peak becomes nearly as flat as the flanks adjacent to it. This corresponds

to the case in which the pre- and post-synaptic spikes are completely asynchronous. Therefore, in this case the inter-spike intervals are produced with an equated probability of being negative or positive. As a result, the plastic modification is weaker when such spikes are the inputs to the STDP. On the contrary, when the jitter variance is small, the inter-spike-intervals are biased towards being predominantly positive or negative. Given our assumptions, this makes the plastic modification produced by synchronized spikes more salient compared to the asynchronous spikes. The expected synaptic modifications and the corresponding cross-correlations for the jittered spikes are shown in Figs. 2 and 3, respectively.

Expected modification depends on the synchronicity and RFT of the spikes. Fig. 4 shows that if the synaptic weight takes an initial value of 0.5, the expected synaptic modification of synchronous spikes increase monotonically with RFT before it saturates. In contrast, the expected synaptic modification of asynchronous spikes reduces as the RFT increases until the RFT is as large as the JI. The more asynchronous the spikes are, the lesser the rate of reduction. When the RFT is zero, the expected synaptic value is the initial value of the synaptic weight.

For the STDP rule in which the potentiation and depression are weighted differently, there is also no change in the general dynamics of the expected weight at the equilibrium as a function of synchronicity and RFT. However, the expected weight does drift in positive or negative direction depending on whether α, the asymmetric factor, is smaller than one (positive drift) or larger than one (negative drift)(see Fig. 4). Besides, the equilibrium weight is closer to 0.5 when the firing rate is higher (Fig. 5). The effect of synchrony on the synaptic modulation is less pronounced for higher firing rates.

Apart from jittering the spikes, asynchronous spikes can be also produced by spike thinning (See Methods). In this case, the level of synchrony depends on how large the proportion of rejected spikes is relative to the number of original spikes, or equivalently, by which factor the firing rate is homogeneously reduced. Fig. 6 shows that although the spikes of varied firing rate converge to a common expected weight at the equilibrium, the speed of convergence varies with synchronicity. Spikes that are more synchronized converge faster.

2. Inhomogeneous Poisson processes

Analytically, we solved special cases for models in which the pre- and post-synaptic spike trains are inhomogeneous Poisson processes. Even in the case of spike trains that are sampled from homogeneous Poisson processes, an inhomogeneity effect arises due to the boundary created by the finite length of the time kernel of the STDP function. In general, it can be shown that the mean synaptic weight for inhomogeneous but synchronous processes is:

$$E(WI_t) = [w_0 \quad TI_2(1) \quad TI_2(2) \quad TI_2(3) \quad ... \quad TI_2(t)] \cdot [\prod_{i=1}^{t} 1 - TI_1(i) \quad \prod_{i=2}^{t} 1 - TI_1(i) \quad \prod_{i=3}^{t} 1 - TI_1(i) \quad ... \quad TI_1(t) \quad 1]^T \tag{19}$$

where

$$TI_1(t) = -\frac{r\lambda}{2b}(p_1 + p_2)t^2 + \lambda r(p_1 + p_2)(1 - \frac{1}{2b})t + \lambda p_1(1 - \frac{t_0}{b})(1 - r) \tag{20}$$

and

$$TI_2(t) = -\frac{r\lambda p_2}{2b}t^2 + \lambda p_2 r(1 - \frac{1}{2b})t \tag{21}$$

TI_1 and TI_2 are quadratic functions of t. Formally, we require that the $t > t_0$ for Eq. 20 but we still keep the succinct formulation used above and keep the weight as w0 during $t < t_0$, since t_0 is normally small.

Instead of working out increasingly tedious derivations, we can simulate the case in which the spikes drawn from inhomogeneous Poisson process are fed into the STDP random walk. For example, when the intensity (instantaneous rate) of the Poisson process oscillates as a square-wave function (see Methods), a result qualitatively comparable to that of the homogenous random walk can be observed (see Fig. 7). In this case the periodicity in the time of both the synchronous spikes and well as asynchronous spikes (i.e., jittered) can be seen in the cross-correlogram (Fig. 8).

Phenomenological model of STDP in cat visual cortex applied to experimental recordings

It is difficult to evaluate theoretically the plastic modification of the synapses in vivo. To our knowledge, the suppression model is the best phenomenological description of that process, as it has been successfully tested and used for the evaluation of the plastic modification of the spikes recorded in cat visual cortex (Froemke and Dan, 2002). In that study, simulation results of the suppression model were in close agreement with the results obtained in vitro, when identical inputs were applied.

We evaluated the synaptic modification in vivo by feeding the spikes recorded in cat primary visual cortex to the suppression model (see Methods). Fig. 9 shows the predicted plastic modification for an arbitrary arrangement of pre- and post-synaptic neurons. This result suggests that the synaptic gain co-varies with the level of synchronicity and the relative firing time.

Furthermore, we employed correlation and partial correlation analyses to depict the linear relationships between the parameters of the cross-correlation and the synaptic modification, as shown in Tables 1 and 2. For both pair-wise correlations and partial correlations, the modulation amplitude and the average firing rate were negatively correlated. This result is expected because the MA is a ratio of the counts of synchronous coincidences relative to the counts of spike coincidences due to chance (see Method), and those two counts strongly depend on the firing rates. Also, as expected, the relative firing time and the magnitude of synaptic modulation are positively correlated.

To further explore the linear correlations, we calculate the sample correlation coefficients for every possible arrangement of pre- and post-synaptic connections within the group of neurons we analyze. Fig. 10 shows the sample distribution of the correlation coefficients. If we assume that the connectivity pattern does not affect the correlations, we can estimate the correlation by analyzing samples of correlation coefficients conditioned on different connectivity patterns. The correlation between the relative firing time and the magnitude of plastic modification has a sample mean of -0.75 ($p < 0.05$). The level of synchrony and the relative firing time are uncorrelated judging from the sample distribution. This result holds even if we condition on either only positive or negative RFT. The sample correlation for the magnitude of plastic modification and the level of synchrony is low, with a sample mean of 0.07 ($p > 0.05$). Consistently with what we have shown in the theoretical part, the RFT and the synchronicity have salient effects on the synaptic modifications even when more elaborated suppression model is used and when applied to real data recorded from visual cortex. Thus, the preset results indicate that our theoretical results are generally applicable.

The modification of synaptic efficiency is eventually expected to saturate as the weights approach certain limits. This non-linear effect has been implemented by the normalization

method in the analyses of the random walk (1). In the suppression model, saturations are implemented by restricting the range of plastic modifications. Fig. 11 shows the effect of saturation on the magnitude of the plastic modification (the connectivity pattern of the neurons is the same as that used to calculate Fig. 9). This result suggests that the synaptic gains are saturated when the pre- and post-synaptic spikes are consistently synchronized.

Discussion

STDP can be understood as a mechanism that translates the spike-timing dynamics into the plastic modification of synapses. At least this is true at the level of the prediction by the phenomenological models. For the equilibrium weight under any conduction delays, the more uncertain the time relationship between the pre- and post-synaptic spikes is, the less the weight deviates from the initial value. When the inter-spike intervals between the pre- and post-synaptic spikes have an equal probability of being positive or negative, the drift of the STDP random walk becomes a chance event with equal probability of being negative or positive. In contrast, when the inter-spike intervals are predominantly positive or negative, the distribution of the drift moves away from initial values.

Since the STDP time kernel decays with time, the relative firing time affects the drift magnitude substantially. Eventually, this effect is manifested in the equilibrium weight of the STDP random walk. This is because relative firing time is actually the expected difference in the spike times between the pre- and post-synaptic neurons. The expected magnitude of the drift is essentially predicted by projecting the time difference onto the time kernel. Closely related to our results, Rubin et al. (2000) reported that the equilibrium weight of synapse changes as a function of the temporal shift of the Poisson pre- and the post-synaptic spikes. Morrison et al. (2008), further proposed that the conduction delays contribute significantly to the equilibrium weight when the pre- and post-synaptic spikes are correlated in time. Those studies are based on the estimation of mean drift of the synaptic modification proposed by Rubin et al and later by Gütig et al. (2003). Such estimation corresponds to the grand average of potentiation and depression over updates, which is conditioned on certain synaptic weights in terms of multiplicative models. More generally, the actual ratio of depressive and potentiating updates should not be neglected as shown in our results. Besides, we offered

solutions based on the analysis of random walk, rather than an approximation of Fokker Planck Equations. Our results expanded those of Rubin et al. and Morrison et al. in showing the effect of relative spiking time in the context of neural synchrony as typically observed in empirical studies,.

Using a modified version of the STDP model, the experimental results also show that the relative firing times exhibited in visual cortex correspond well to those needed for plastic modification of cortical synapses. This effect reflects the analytical prediction that shows a strong effect of the relative firing time on the synaptic modification. Moreover, this effect is not mediated by co-varying factors as verified by the result of partial correlation. The suppression effect embedded in the suppression STDP model serves as an additional modulator that is sensitive to the firing rate. When the firing rate is low, the suppressive effect is not strong enough to make the result fundamentally different from the theoretical ones.

Long-term synaptic plasticity is likely to be the basis for memory traces. Therefore, our result may have some implication for the studies of memory as well. For example, it has been shown that increased power of gamma or theta oscillation measured in EEG or MEG is a strong predicator of better performance in memory encoding and retrieval tasks (Fell et al., 2001; Sederberg et al., 2003). As a result, there must be some mechanisms via which the increased beta/gamma or theta oscillation makes the neurons more susceptible to synaptic plasticity (Wespatat et al., 2004). Our results indicate that gamma oscillation can modulate the modification of synapses via facilitating STDP.

We predicted that significant synaptic modification can occur only when the pre- and post synaptic activities are sufficiently synchronized in the regime of STDP. When the gamma oscillations get stronger, spike times of pre- and post-synaptic spikes tend to be more

synchronized. In turn, the chance of plastic change via STDP is also increased as compared to weak gamma oscillations. During the brain activities involved in memory, the effect of synchronized inputs on the efferent output probably also plays an important role, as synchronized inputs may provide a stronger drive of the downstream neurons than non-synchronized inputs (e.g., Biederlack et al., 2006). It has been shown theoretically that the synchronized pre-synaptic inputs produce stronger synaptic modifications via STDP than uncorrelated inputs (van Rossum et al., 2000). Thus, when the inputs are correlated, the temporal correlation between the inputs and outputs from a neuron becomes stronger as well.

Conclusion

We demonstrated that it is possible to investigate theoretically the time-resolved evolution of the STDP using the approach of random walks. Further, we probed the synaptic modification induced by the spikes that are recorded in vivo and that exhibit oscillatory patterning in gamma range. Both approaches lead to the conclusion that for the STDP model, which reflects the excitatory to excitatory synaptic connections (Caporale and Dan, 2008), the significant plastic modulation of synapse exists only when the pre- and post-synaptic spikes are sufficiently synchronized and when delays exist between spike trains. We conclude that one likely function of gamma oscillations is to facilitate plasticity in the cortex as it produces the temporal structures of spike trains ideal for effective induction of STDP.

Acknowledgement

This project is supported by a DFG grant number NI 708/2-1. In addition, support came from the Hertie Foundation, and the German Federal Ministry of Education and Research (BMBF) within the "Bernstein Focus: Neurotechnology" through research grant 01GQ0840.

References:

Fries P, Reynolds JH, Rorie AE, Desimone R. Modulation of oscillatory neuronal synchronization by selective visual attention. *Science* **291**, 1560-1563 (2001).

Womelsdorf T, Fries P. Neuronal coherence during selective attentional processing and sensory-motor integration. *J Physiol Paris.***100**, 182-193 (2006).

Fan J, Byrne J, Worden MS, Guise KG, McCandliss BD, Fossella J, Posner MI. The relation of brain oscillations to attentional networks. *J Neurosci.* **27**, 6197-6206 (2007)

Doesburg SM, Roggeveen AB, Kitajo K, Ward LM. Large-scale gamma-band phase synchronization and selective attention. *Cereb Cortex.* **18**, 386-396 (2008).

Castelo-Branco M, Goebel R, Neuenschwander S, Singer W. Neural synchrony correlates with surface segregation rules. *Nature*. **405**, 685-689 (2000).

Kreiter AK, Singer W. Stimulus-dependent synchronization of neuronal responses in the visual cortex of the awake macaque monkey. *J Neurosci.* **16**, 2381-2396 (1996).

Lakatos P, Chen CM, O'Connell MN, Mills A, Schroeder CE. Neuronal oscillations and multisensory interaction in primary auditory cortex. *Neuron*. **53**, 279-292 (2007).

Roelfsema PR, Engel AK, König P, Singer W. Visuomotor integration is associated with zero time-lag synchronization among cortical areas. *Nature.* **385**, 157-161 (1997).

Havenith MN, Yu S, Biederlack J, Chen NH, Singer W, Nikolić D. Synchrony makes neurons fire in sequence, and stimulus properties determine who is ahead. *J Neurosci.* **8**, 8570-8584 (2011).

Nikolić D. Non-parametric detection of temporal order across pairwise measurements of time delays. *J Comput Neurosci.* **22**, 5-19

Schneider, G. Nikolić D. Detection and assessment of near-zero delays in neuronal spiking activity. *J Neurosci Methods.***152**, 97-106 (2006).

Schneider, G., Havenith M , Nikolić D. Spatio-temporal structure in large neuronal networks detected from cross correlation. *Neural Comput.* **18**, 2387-2413 (2006).

König P, Engel AK, Roelfsema PR, Singer W. How precise is neuronal synchronization?

Neural Comput. **7**, 469-485 (1995).

Antonov I, Antonova I, Kandel ER, Hawkins RD. The contribution of activity-dependent synaptic plasticity to classical conditioning in Aplysia. *J Neurosci.* **21,** 6413-6422 (2001)

Tsanov M, Manahan-Vaughan D. Intrinsic, light-independent and visual activity-dependent mechanisms cooperate in the shaping of the field response in rat visual cortex. *J Neurosci.* **27**,8422-8429 (2007).

Zucker RS. Calcium- and activity-dependent synaptic plasticity. *Curr Opin Neurobiol.* **9**, 305-313 (1999).

Rebola N, Srikumar BN, Mulle C. Activity-dependent synaptic plasticity of NMDA receptors. *J Physiol.* **588**, 93-99 (2010).

Caporale N, Dan Y. Spike timing-dependent plasticity: a Hebbian learning rule. *Annu Rev Neurosci.* **31**, 25-46 (2008).

Citri A, Malenka RC. Synaptic plasticity: multiple forms, functions, and mechanisms. *Neuropsychopharmacology* **33**, 18-41 (2008).

Markram H, Lübke J, Frotscher M, Sakmann B. Regulation of synaptic efficacy by coincidence of postsynaptic APs and EPSPs. *Science* **275**, 213-215 (1997).

Bi GQ, Poo MM. Synaptic modifications in cultured hippocampal neurons: dependence on spike timing, synaptic strength, and postsynaptic cell type. *J Neurosci.* **18**, 10464-10472 (1998).

Jacob V, Brasier D, Erchova I, Feldman D, Shulz D. Spike Timing-Dependent Synaptic Depression in the In Vivo Barrel Cortex of the Rat. *J. Neurosci.* **27**, 1271–1284 (2007).

Wang P, Havenith M, Best M, Gruetzner C, Singer W, Uhlhaas P, Nikolić D. Time delays in the beta/gamma cycle operate on the level of individual neurons. *Neuroreport*. **21**, 746-750 (2010).

Froemke RC, Dan Y. Spike-timing-dependent synaptic modification induced by natural spike trains. *Nature* **416**, 433-438 (2002).

Kempter R, Gerstner W, van Hemmen J.L, Hebbian Learning and Spiking Neurons. *Phys. Rev. E* **59**, 4498-4514 (1999).

Williams A, Leen T, Roberts P, Random walks for spike-timing-dependent plasticity. *Phys. Rev. E* **70**, 021916 (2004).

Elliott T. Discrete states of synaptic strength in a stochastic model of spike-timing-dependent plasticity. *Neural Comput.* **22**, 244-272 (2010).

Morrison A, Diesmann M, Gerstner W. Phenomenological models of synaptic plasticity based on spike timing. *Biol Cybern.* **98**, 459-478 (2008).

Rubin J, Lee DD, Sompolinsky H. Equilibrium properties of temporally asymmetric Hebbian plasticity. *Phys Rev Lett.* **86**, 364-367 (2001).

Câteau H, Fukai T. A stochastic method to predict the consequence of arbitrary forms of spike-timing-dependent plasticity. *Neural Comput.* **15**, 597-620 (2003).

Leen TK, Friel R. Stochastic perturbation methods for spike-timing-dependent plasticity. *Neural Comput.* **24**, 1109-1146 (2012).

Swadlow HA, Kocsis JD, Waxman SG. Modulation of impulse conduction along the axonal tree. *Annu Rev Biophys Bioeng.* **9**,143-179 (1980).

Biederlack J, Castelo-Branco M, Neuenschwander S, Wheeler DW, Singer W, Nikolić D. Brightness induction: rate enhancement and neuronal synchronization as complementary codes. *Neuron* **52**, 1073-1083 (2006).

P. Dayan, L. Abbott, *Theoretical Neuroscience: Computational And Mathematical Modeling of Neural Systems.* (Mit Press, London, 2005)

S Grün, S Rotter, *Analysis of Parallel Spike Trains.* (Springer, New York, 2010)

Gütig R, Aharonov R, Rotter S, Sompolinsky H. Learning input correlations through nonlinear temporally asymmetric Hebbian plasticity. *J Neurosci.* **23**, 3697-3714 (2003).

Fell J, Klaver P, Lehnertz K, Grunwald T, Schaller C, Elger CE, Fernández G. Human memory formation is accompanied by rhinal-hippocampal coupling and decoupling. *Nat Neurosci.* **4**, 1259-64 (2001).

Sederberg PB, Kahana MJ, Howard MW, Donner EJ, Madsen JR. Theta and gamma oscillations during encoding predict subsequent recall. *J Neurosci.* **23**, 10809-10814 (2003).

Wespatat V, Tennigkeit F, Singer W. Phase sensitivity of synaptic modifications in oscillating cells of rat visual cortex. *J Neurosci.* **24**,9067-9075 (2004).

van Rossum MC, Bi GQ, Turrigiano GG. Stable Hebbian learning from spike timing-dependent plasticity. *J Neurosci.* **20**, 8812-8821 (2000).

Tallon-Baudry C, Bertrand O, Oscillatory gamma activity in humans and its role in object representation. *Trends in Cognitive Sciences.* **3**,151-162. (1999).

Sjöström PJ, Turrigiano GG, Nelson SB. Rate, timing, and cooperativity jointly determine cortical synaptic plasticity. *Neuron* **32**, 1149-1164 (2001).

Table legends

Table 1. Correlation matrix for the parameters of cross-correlation and the predicted synaptic modification. These correlation results are for the same connectivity pattern as the one use to compute the results shown in Fig. 7. The asterisks indicate significant correlations, $p < 0.05$.

Table 2. Partial-correlation matrix. These correlation results are for the same matrix as the one used to compute the results shown in Fig. 7. The asterisks indicate significant correlations, $p < 0.05$.

Table 1

	Optimality Index	Relative firing time	Average firing rate	Oscillation frequency	Modulation amplitude	Synaptic gain
Optimality Index	1					
Relative firing time	0.13	1				
Average firing rate	-0.17	-0.05	1			
Oscillation frequency	-0.15	-0.11	-0.10	1		
Modulation amplitude	0.21	-0.43	-0.49*	0.13	1	
Synaptic gain	0.01	-0.78*	0.18	-0.16	0.36	1

Table 2

	Optimality Index	Relative firing time	Average firing rate	Oscillation frequency	Modulation amplitude	Synaptic gain
Optimality Index	1					
Relative firing time	0.23	1				
Average firing rate	-0.04	-0.03	1			
Oscillation frequency	-0.12	-0.31	-0.06	1		
Modulation amplitude	0.22	-0.18	-0.57*	0.16	1	
Synaptic gain	0.11	-0.75*	0.31	-0.38	0.23	1

Figures legends

Figure 1. The evolution of the synaptic weight for fully synchronized homogeneous Poisson processes with different lags denoted by *t0*. The expected synaptic modification is shown by solid curve and the realizations are shown by dotted curves.

Figure 2. The evolution of the synaptic modification as a random walk. The solid curves are the expected modifications of the synapses over time. The dotted curves are single realizations. JI stands for jitter intervals. t_0 = 5 ms. b = 50 ms, r = 20 Hz.

Figure 3. The cross-correlations of a Poisson process with itself but shifted in time for 5 milliseconds. JI stands for jitter intervals.

Figure 4. Expected synaptic modifications at the equilibrium for the synchronous and asynchronous spikes. For α equals one at a certain RFT, the weight at the equilibrium is closer to the initial weight when the spikes times are less synchronous. For the synchronous spikes, the equilibrium weight increases monotonically with the RFT. In contrast, the equilibrium weight of asynchronous spikes drops with increasing RFT until the RFT is as large as JI. The equilibrium weight of asynchronous spike converges to that of the synchronous spike when the RFT is bigger than the jittering interval. When α is smaller than one, there is a positive drift of the expected weight at the equilibrium.

Figure 5. Expected synaptic modifications at the equilibrium for different firing rates. Sp/Sec: spikes per second.

Figure 6. The expected synaptic modifications for asynchronous spikes produced by spike thinning. Dashed curves: t_0 = 8 ms. Solid curves, t_0 = 2 ms. FR: the expected firing rate of the

pre-synaptic spike as a proportion to the firing rate of the post-synaptic spikes, *r*. In this case *r* = 20 spikes per second.

Figure 7. The evolution of the synaptic modification for an inhomogeneous Poisson process, with an oscillation period of 0.05 seconds. Single drifts and mean drifts of synaptic modifications are indicated by dotted and solid curves, respectively.

Figure 8. Cross-correlation for an inhomogeneous Poisson process with a copy of itself shifted in time (fully synchronous but lagged; 10-millisecond shift), and that of the surrogate processes (partially synchronous and jittered).

Figure 9. The Cross-correlograms between spike trains and the corresponding synaptic modifications. **A:** Cross-correlograms between spike trains for analyses reported in B. B: The grand average of synaptic modification as evaluated by the suppression model and predicted by the level of synchrony indicated by the modulation amplitude (MA), relative firing time (RFT), and the optimality of the stimuli. The color code represents the sign and magnitude of RFT. The size of the dots represents the optimality of the stimuli (larger dots-more optimal stimuli). The numbers associated with data points indicate the cross correlogram in A.

Figure 10. The sample distribution of the correlation coefficients calculated for every possible arrangement of synaptic connections for the neurons (the sample size is 2^{20}). SM: synaptic modification. MA: modulation amplitude. RFT: relative firing time.

Figure 11. Averaged synaptic modifications plotted against the average interval of pre- and post-synaptic spikes (RFT). The saturation of the synaptic modification was either set to infinity, -1.5 and 1.5, or -0.34 and 0.65 (according to Froemke et al., 2006).

Figure 1

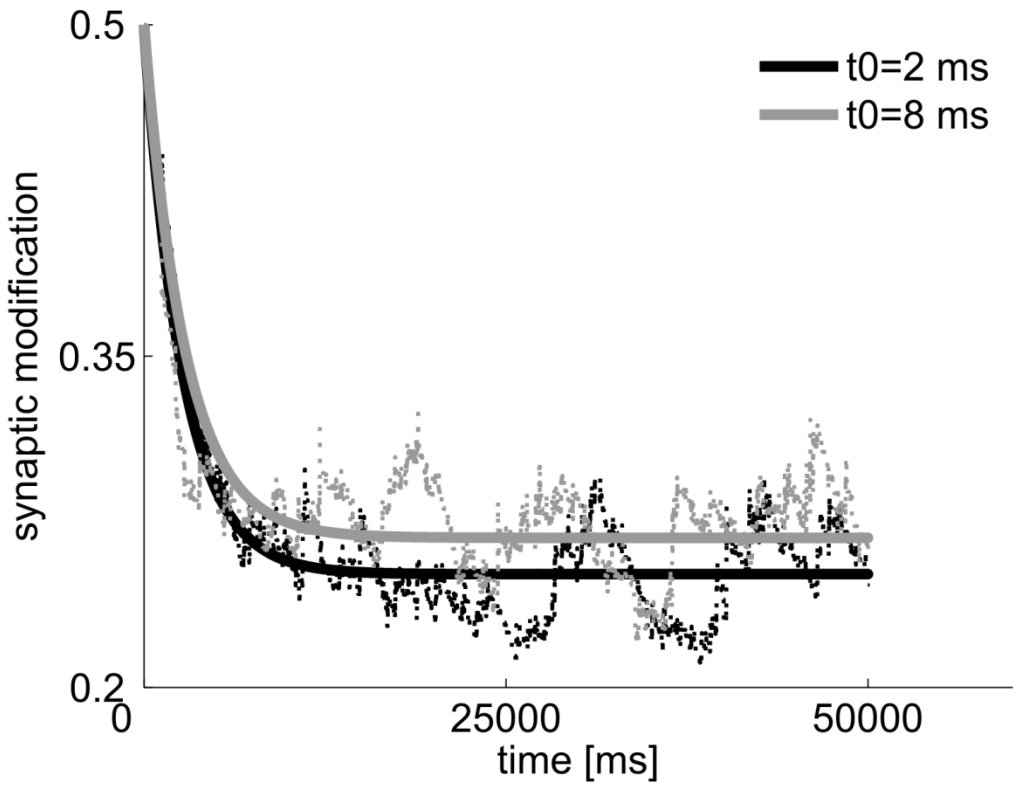
0.5
0.35
0.2
synaptic modification
0
25000
50000
time [ms]
t0=2 ms
t0=8 ms

Figure 2

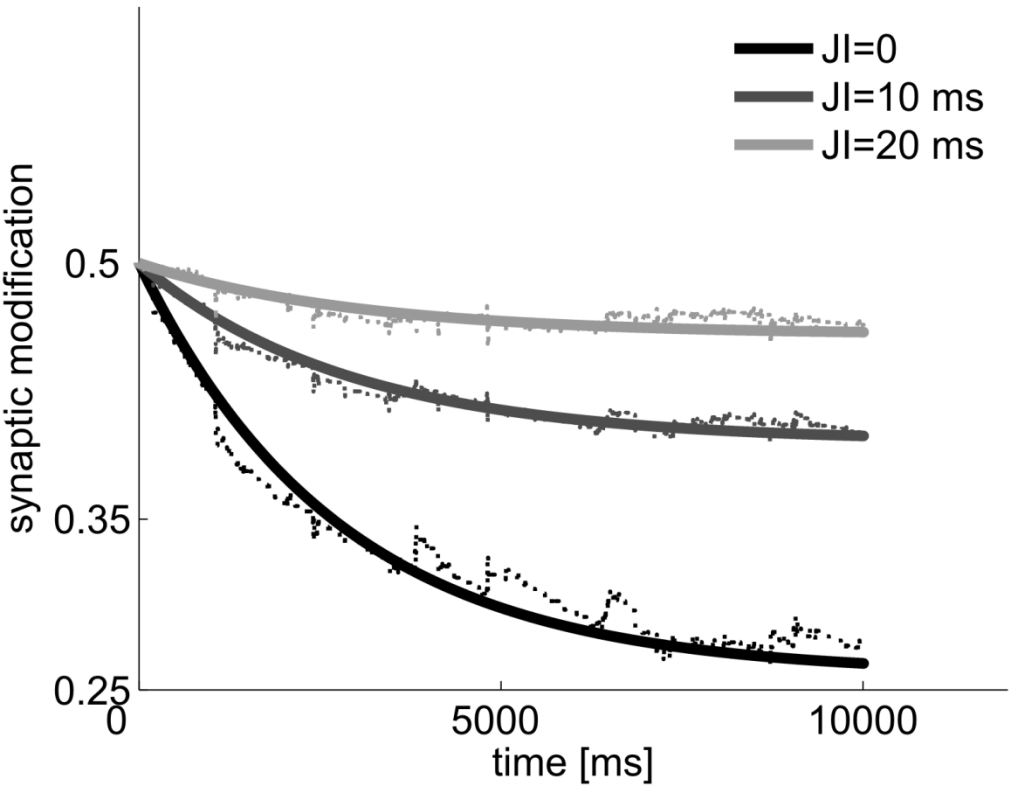
JI=0
JI=10 ms
JI=20 ms
synaptic modification
0.5
0.35
0.25
0
5000
10000
time [ms]

Figure 3

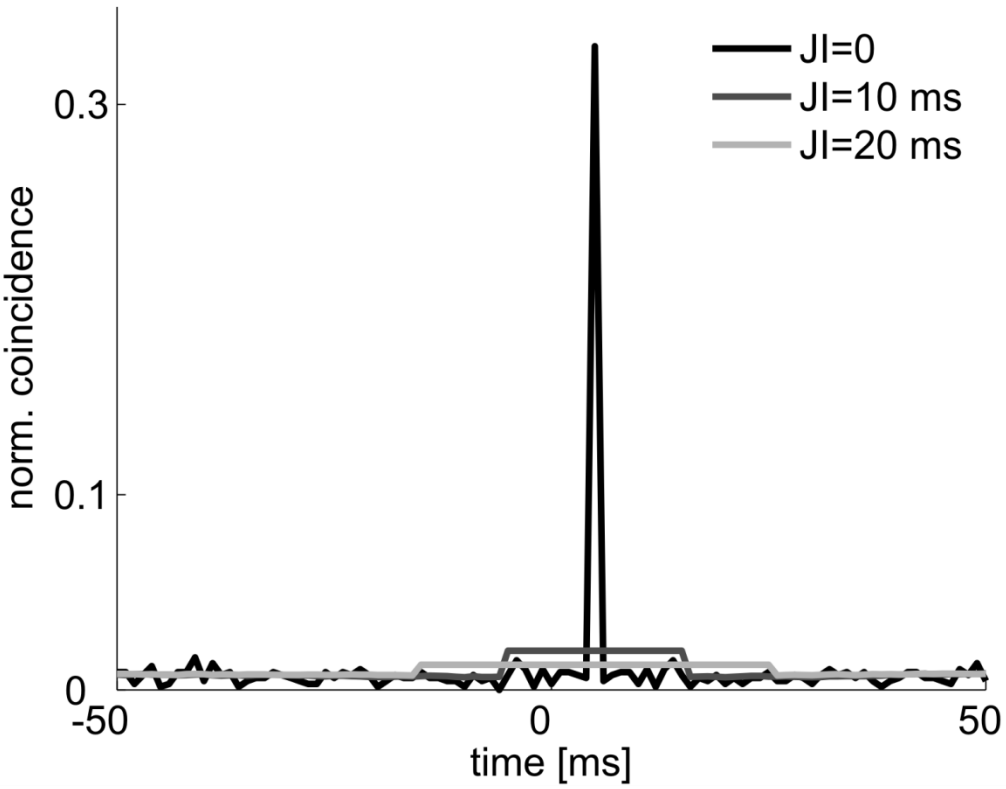

Figure 4

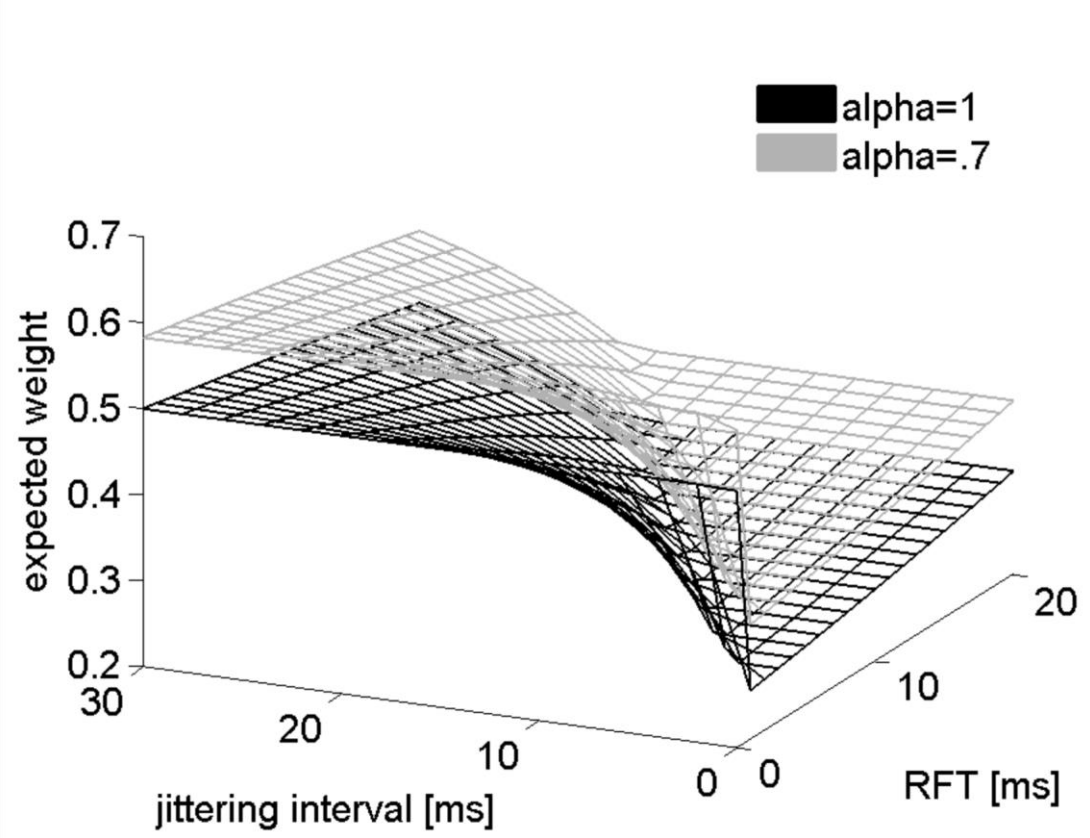
alpha=1
alpha=.7
0.7
0.6
0.5
0.4
0.3
0.2
expected weight
30
20
10
0
jittering interval [ms]
0
10
20
RFT [ms]

Figure 5

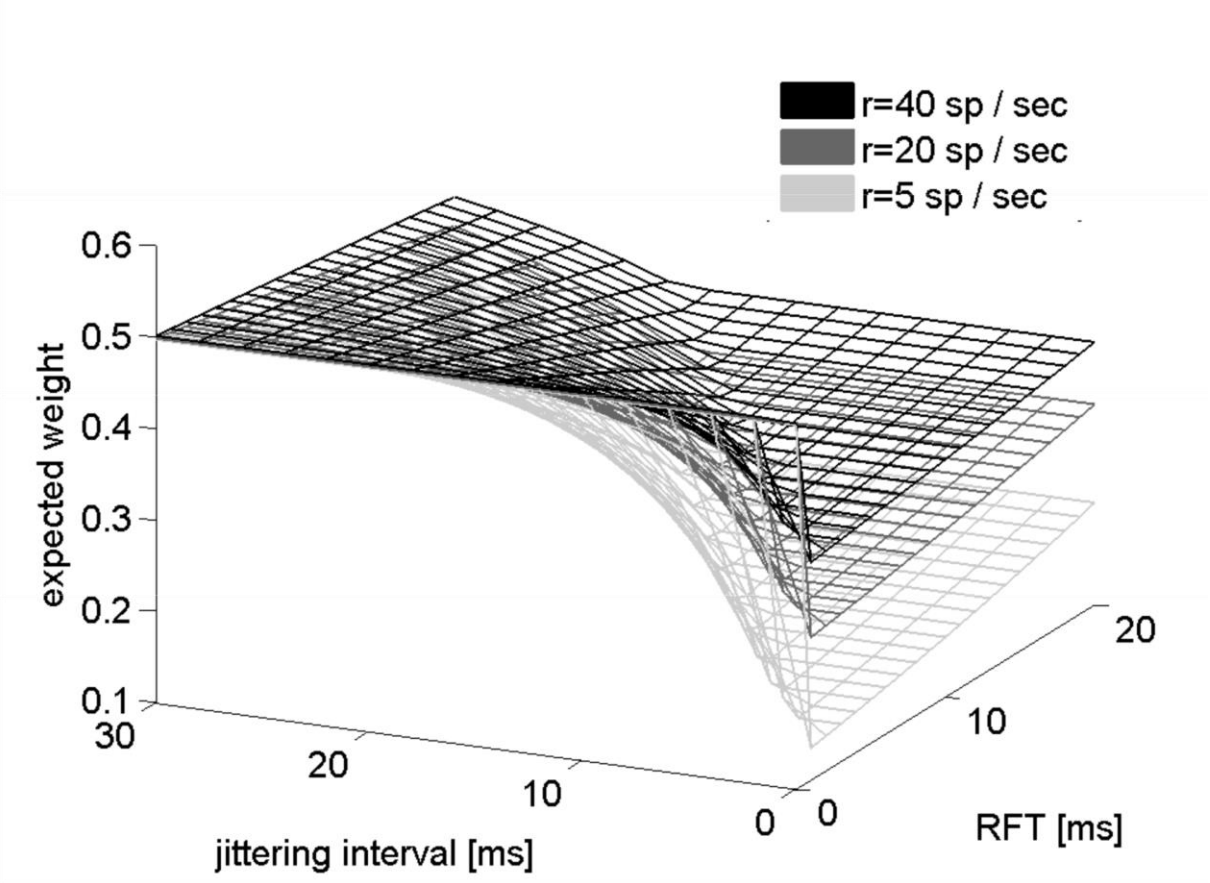
r=40 sp / sec
r=20 sp / sec
r=5 sp / sec
expected weight
0.6
0.5
0.4
0.3
0.2
0.1
30
20
10
0
jittering interval [ms]
0
10
20
RFT [ms]

Figure 6

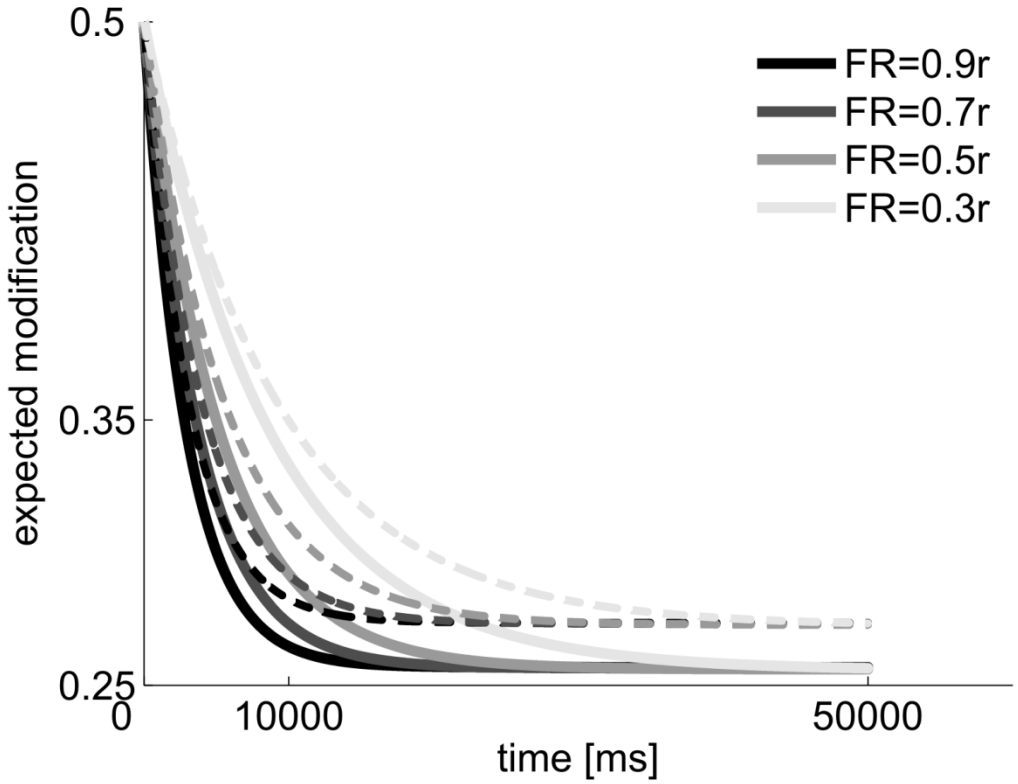
0.5
0.35
0.25
expected modification
0
10000
50000
time [ms]
FR=0.9r
FR=0.7r
FR=0.5r
FR=0.3r

Figure 7

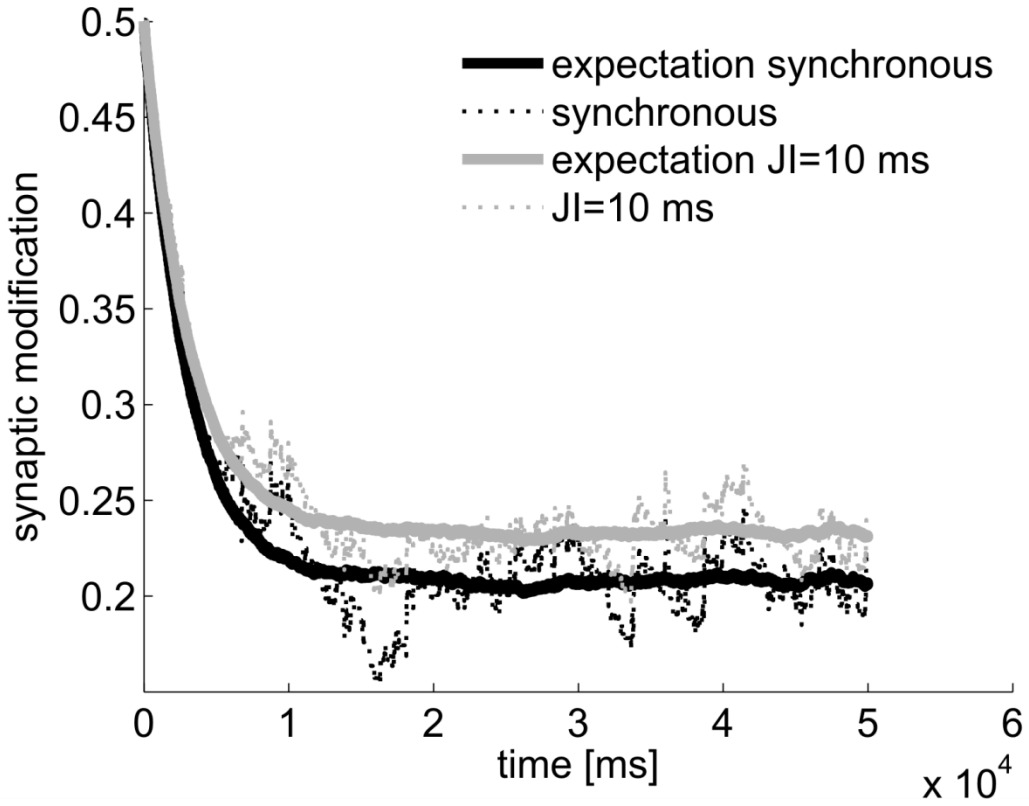
0.5
0.45
0.4
0.35
0.3
0.25
0.2
synaptic modification
0
1
2
3
4
5
6
time [ms]
x 10^4
expectation synchronous
synchronous
expectation JI=10 ms
JI=10 ms

Figure 8

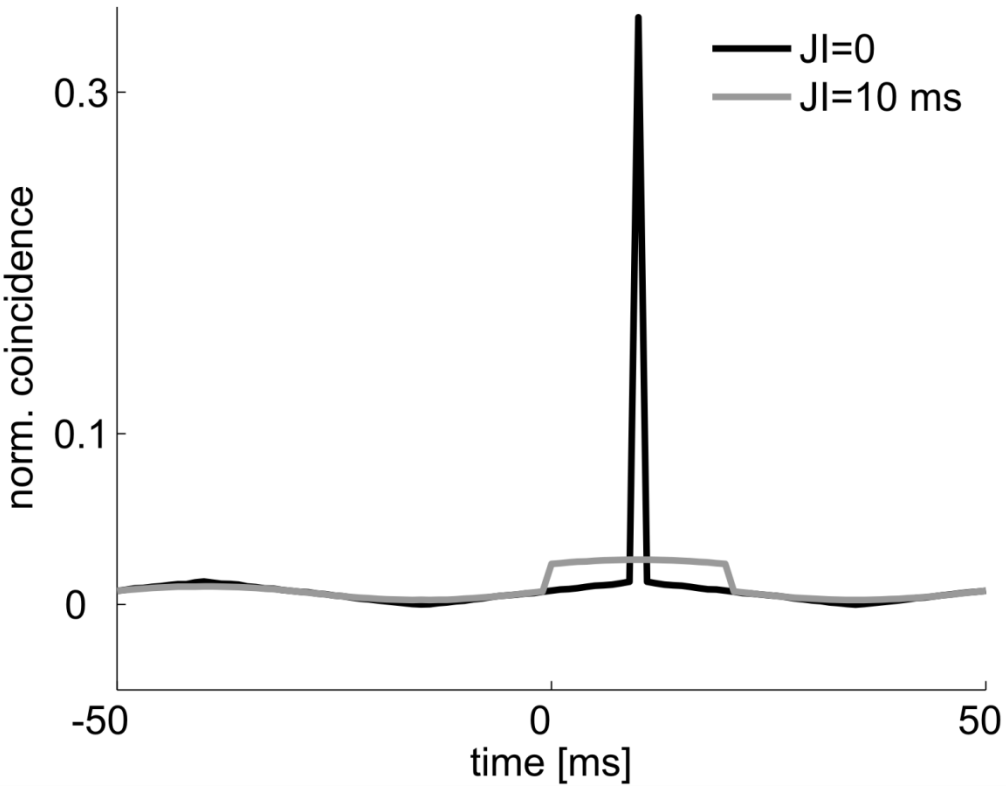

Figure 9

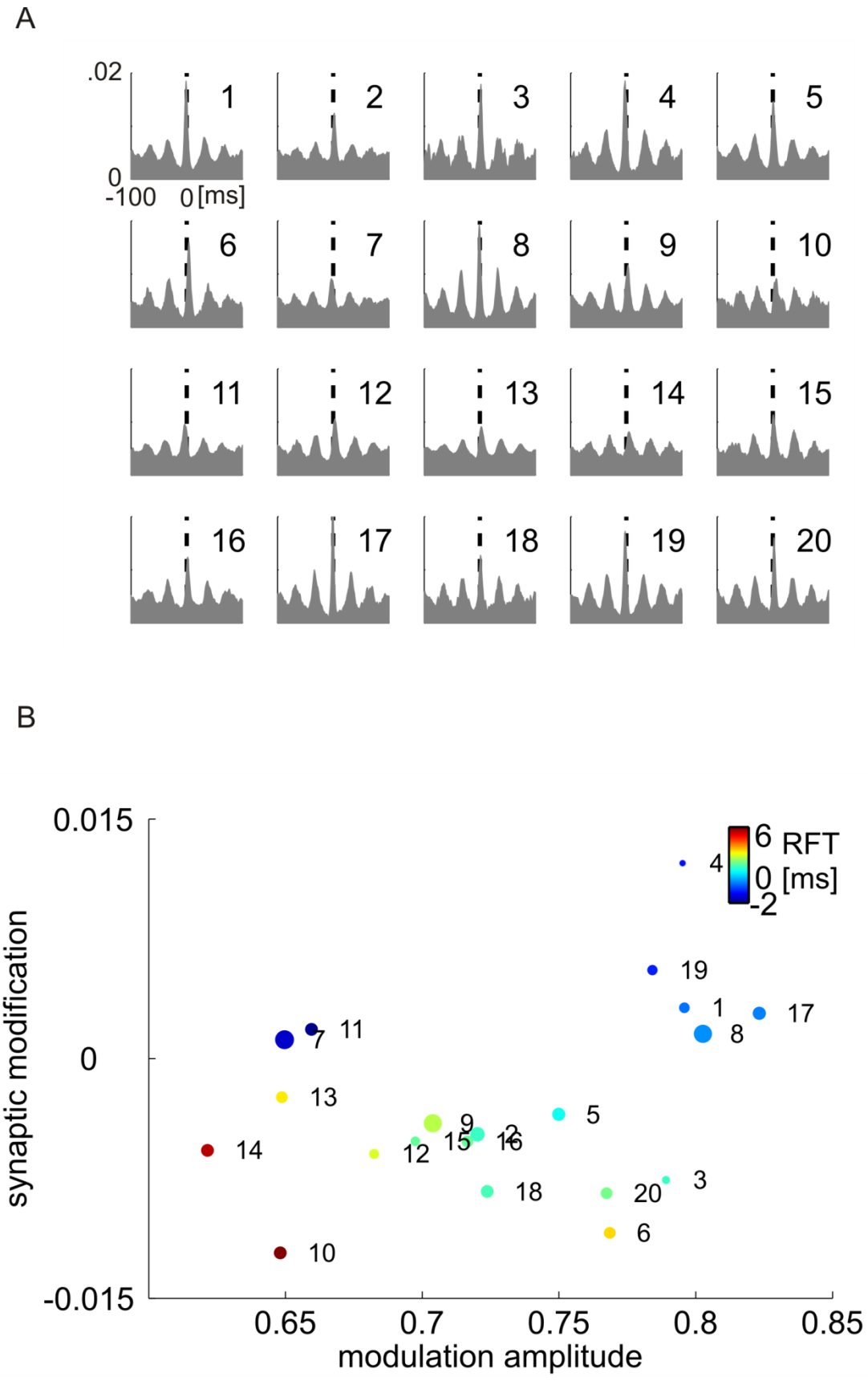
A
.02
0
-100
0 [ms]
1
2
3
4
5
6
7
8
9
10
11
12
13
14
15
16
17
18
19
20
B
0.015
0
-0.015
synaptic modification
0.65
0.7
0.75
0.8
0.85
modulation amplitude
6
RFT
0 [ms]
-2

Figure 10

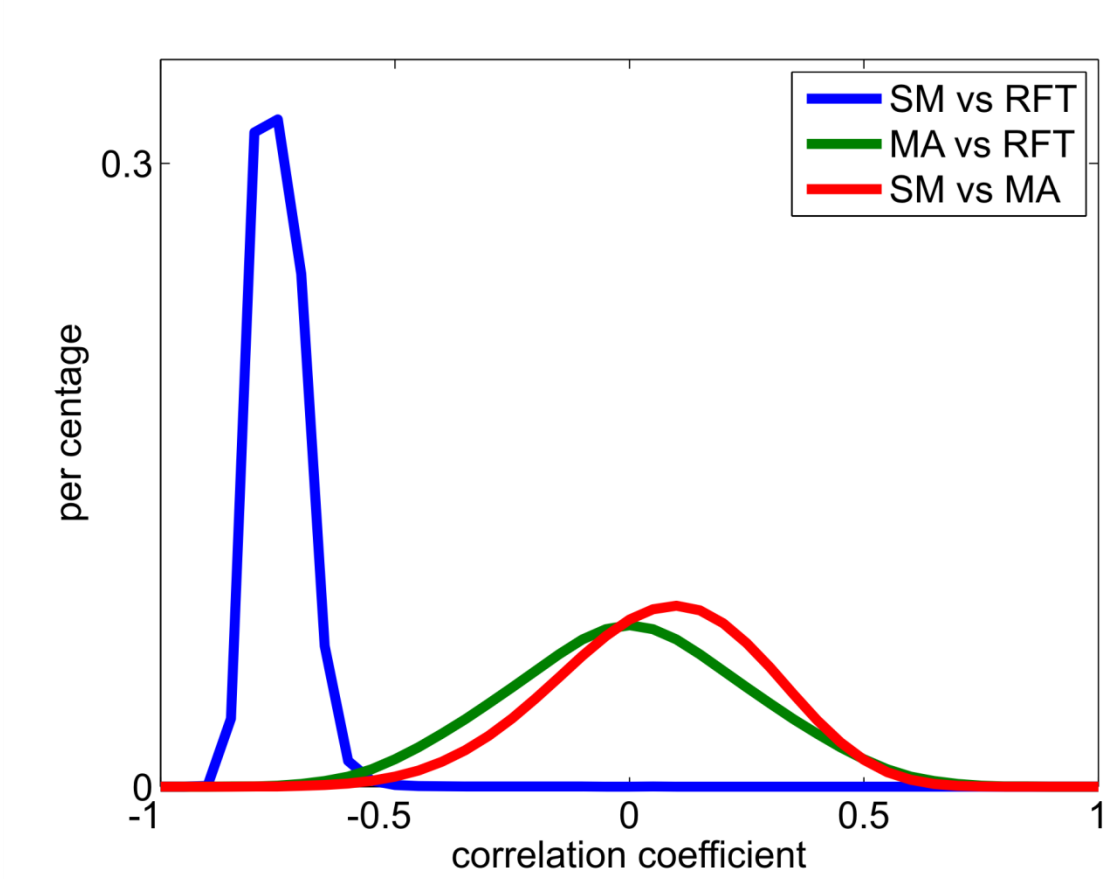
SM vs RFT
MA vs RFT
SM vs MA
0.3
0
per centage
-1
-0.5
0
0.5
1
correlation coefficient

Figure 11

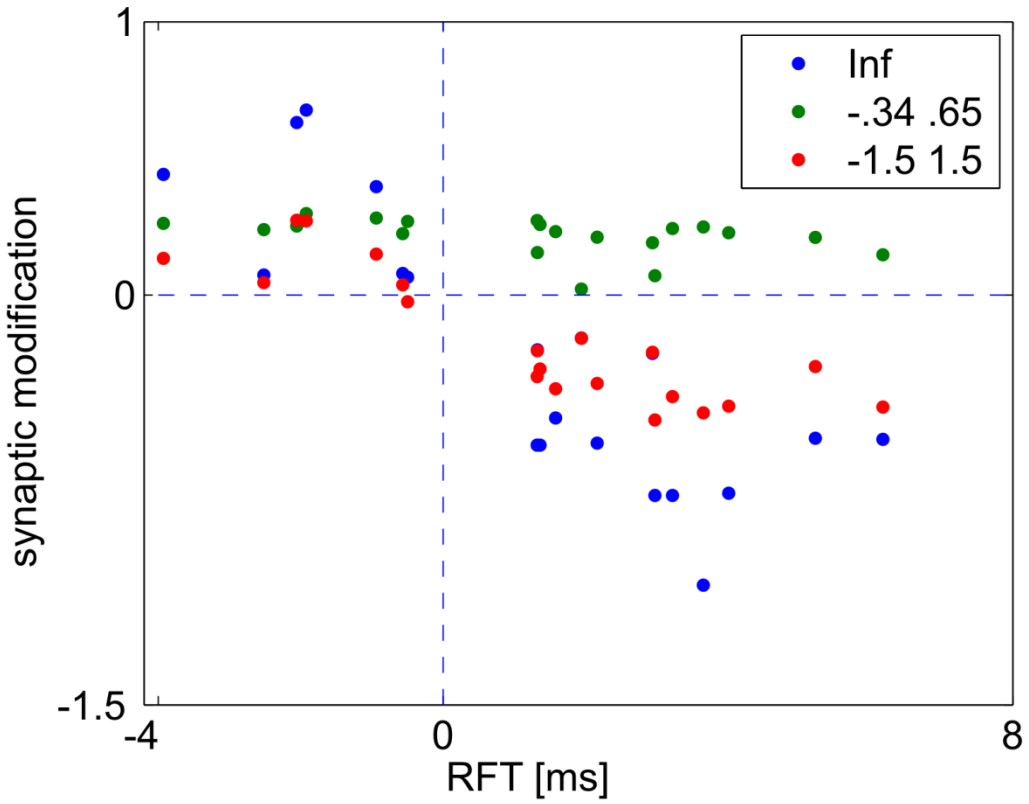

Appendix

1. Estimation of averaged synaptic modification (first raw moment)

We calculate the expected value of the synaptic weights according to the homogenous iterative relations defined in Eq. (1) in the main text:

$$E(w_t \mid F_d(t), F_p(t)) = E(w_t \mid F_d, F_p)$$
$$= p_1(E(w_{t-1} \mid F_d, F_p) - \lambda\alpha E(w_{t-1} \mid F_d, F_p)F_d) + p_2(E(w_{t-1} \mid F_d, F_p) + \lambda(1 - E(w_{t-1} \mid F_d, F_p))F_p) +$$
$$p_3[E(w_{t-1} \mid F_d, F_p) - \lambda\alpha E(w_{t-1} \mid F_d, F_p)F_d) + \lambda(1 - E(w_{t-1} \mid F_d, F_p) + \lambda\alpha E(w_{t-1} \mid F_d, F_p)F_d)F_p] + p_4 E(w_{t-1} \mid F_d, F_p)$$

Given that the potentiating increment, depressive increment and the weights are mutually independent, it follows:

$$E(w_t) = E_{F_d}(E_{F_p}(E(w_t \mid F_d, F_p))$$
$$= p_1(E(w_{t-1}) - \lambda\alpha E(w_{t-1})E(F_d)) + p_2(E(w_{t-1}) + \lambda(1 - E(w_{t-1}))E(F_p)) + p_3[E(w_{t-1}) - \lambda\alpha E(w_{t-1})E(F_d)) + \lambda(1 - E(w_{t-1}) + \lambda\alpha E(w_{t-1})E(F_d))E(F_p)] + p_4 E(w_{t-1})$$

which gives:

$$E(w_t) = [1 - \alpha\lambda(p_1 + p_3)E(F_d) - \lambda(p_2 + p_3)E(F_p) + \lambda^2\alpha E(F_d)E(F_p)]E(w_{t-1}) + \lambda(p_2 + p_3)E(F_p)$$

Alternatively, the equation above can be written as:

$$E(w_t) = T_1 E(w_{t-1}) + T_2,$$

where T_1 and T_2 are substitutes for the coefficients of $E(w_t\text{-}1)$ and the constants, respectively. We can then write:

$$E(w_1) = T_1 E(w_0) + T_2$$

$$E(w_2) = T_1(E(w_1)) + T_2$$
$$= T_1(T_1(E(w_0) + T_2)) + T_2$$

$$E(w_3) = T_1(E(w_2)) + T_2$$
$$= T_1(T_1(T_1(E(w_0) + T_2)) + T_2) + T_2$$
$$\vdots$$

which leads to Eq. (5) in the main text.

2. **Second raw moment of the STDP random walk for the jittered spikes**

First, we examine the distribution of jittered Poisson arrivals of spikes with the intensity λ and bin-size Δt. After jittering, the probability of observing a spike in the *d-th* bin can be noted as *p* (arrival at *d*), where the *d-th* bin is far from the boundaries of the observation (i.e., far from the beginning and the end of the spike train). Given that the magnitude of jitter is independent of the original spike time, the following holds when Δt is sufficiently small:

$$\begin{aligned} p(\text{arrival at } d) &= p(\text{originally at } d)\,p(\text{jittered by zero} \mid d) + p(\text{originally at } d-t_1)\,p(\text{jittered by } t_1 \mid d-t_1) + \\ &\quad p(\text{originally at } d-t_2)\,p(\text{jittered by } t_2 \mid d-t_2) + \dots \\ &= \lambda\Delta t\,(p(\text{jittered by zero}) + p(\text{jittered by } t_1) + p(\text{jittered by } t_2) + \cdots) = \lambda\Delta t \end{aligned}$$

This shows that a Poisson spike train that is jittered remains Poisson-distributed, provided that the boundary effect is negligible.

Next, we calculate the squared increment of potentiation (F_p^2) for the jittered spikes. In the most general case, the jitter interval *JI* is larger than the relative firing time t_0 (i.e., the time delay), the latter normally not exceeding 10-15 milliseconds. In such a general case, a post-synaptic spike can precede, coincide with, or follow its own copy in the pre-synaptic spike train. The first two possibilities (post-synaptic preceding pre-synaptic and coincidence) happen with probability 1-p_b and the third case happens with the probability p_b. The corresponding squared increments of potentiation are denoted as F_{p1}^2 and F_{p2}^2, respectively. We therefore write the squared potentiation as:

$$F_p^2 = \begin{cases} F_{p1}^2 = (n - \dfrac{\sum d_i}{b})^2 & 1-p_b \\ F_{p2}^2 = (1 - \dfrac{s}{b} + n - \dfrac{\sum d_i}{b})^2 & p_b \end{cases}$$

The conditional expectation of the $F_{p1}{}^2$ is:

$$E(F_{p1}^2 \mid n) = \frac{1}{b^2}[nE(d_i^2 \mid n) + n(n-1)E(d_i \mid n)^2] - \frac{2n^2}{b} \cdot \frac{1+b}{2} + n^2.$$

Therefore,

$$E(F_{p1}^2) = E(E(F_{p1}^2 \mid n)) = \frac{(b-1)^2}{4} r^2 - \frac{5b^2 + 24b + 7}{12b} r.$$

Likewise, the conditional expectation of $F_{p2}{}^2$ is:

$$E(F_{p2}{}^2 \mid n,s) = \frac{1}{b^2}[s^2 + 2snE(d_i \mid n,s) + E((\sum_n d_i)^2 \mid n,s)] - \frac{2}{b}(1+n)(s + nE(d_i \mid n,s)) + (1+n)^2$$

$$E(F_{p2}{}^2 \mid n) = \frac{1}{b^2(b-1)^2}[n^2 - (3b-2)n + (b-1)^2]E(s^2 \mid n) + \frac{1}{b(b-1)^2}[(3b-1)n^2 + (-b^2+4b-3)n - 2(b-1)^2]E(s \mid n) +$$
$$[-\frac{2}{b-1} - \frac{(b+1)^2}{4(b-1)^2}]n^2 + [1 + \frac{(2b+1)(b+1)}{6b(b-1)} - \frac{(b+1)^2}{4(b-1)^2}]n + 1$$

Therefore,

$$E(F_{p2}^2) = \frac{1}{b^2(b-1)^2}[E(n^2) - (3b-2)E(n) + (b-1)^2]E(s^2) + \frac{1}{b(b-1)^2}[(3b-1)E(n^2)$$
$$+(-b^2+4b-3)E(n) - 2(b-1)^2]E(s) + [-\frac{2}{b-1} - \frac{(b+1)^2}{4(b-1)^2}]E(n^2) + [1 + \frac{(2b+1)(b+1)}{6b(b-1)} - \frac{(b+1)^2}{4(b-1)^2}]E(n) + 1,$$

where the following quantities are substituted as follows:

$$E(n) = r(b-1),$$

$$E(n^2) = r(b-1)(1+rb-r),$$

$$E(s) = \frac{JI - t_0 + 1}{2},$$

and

$$E(s^2) = \frac{(JI - t_0 + 1)(2JI - 2t_0 + 1)}{6}.$$

We combine the results of $E(F_{p1}{}^2)$ and $E(F_{p2}{}^2)$ into:

$$E(F_p^2) = E(F_{p1}^2)(1 - p_b) + E(F_{p2}^2)p_b,$$

where p_b is:

$$p_b = \frac{JI - t_0}{2JI + 1}.$$

The second raw moment for the depressive increments can be found in a similar way. The second raw moment of the synaptic modification for the jittered spike trains can be calculated by plugging the first two raw moments of depression and potentiation into the Eq. (13) located in the main text.

3: Numerical approximation of the homogeneous transition probability for the multiplicative model

Given that the synaptic modification w ranges between zero and one, we can define the following state space: $w \in \{0, w_1, w_2, w_3, \cdots, 1\}$, for which $w_1 = \Delta w$, $w_2 = 2\Delta w$, $w_3 = 3\Delta w$, and so on, and Δw is the bin-size of the discrete variable w. If the synaptic weight at time t is denoted as w_i, the probability that the synaptic weight updates from w_i to w_j at time t+1 is denoted as $p_{w_i w_j}$. Given the assumptions of the homogenous random walk outlined in the main text, if follows that $p_{w_i w_j}$ is time-invariant. According to definition in Eq. (1) in the main text, $p_{w_i w_j}$ can be expressed as:

$$p_{w_i w_j} = \begin{cases} 1 - p_1 - p_2 + P\{0 \le f_d < \Delta_d)\}p_1 + P\{0 \le f_p < \Delta_p)\}p_2 & \text{when i=j} \\ p_1 P\{\frac{1}{\lambda}(1-\frac{w_j}{w_i}) - \Delta_d < f_d < \frac{1}{\lambda}(1-\frac{w_j}{w_i}) + \Delta_d\} & \text{when i>j} \\ p_2 P\{\frac{w_j - w_i}{\lambda(1-w_i)} - \Delta_p < f_p < \frac{w_j - w_i}{\lambda(1-w_i)} + \Delta_p\} & \text{when i<j} \end{cases}$$

where Δ_d and Δ_p are defined as $\Delta_d = \frac{5 \times 10^{-rd}}{\lambda w_i}$, $\Delta_p = \frac{5 \times 10^{-rd}}{\lambda(1-w_i)}$. Δ_d specifies the range of f_d that leads to a w_j rounded at the *rd*-th decimal. Δ_p is similarly defined for f_p.

The transition probability $p_{w_i w_j}$ determines how the distribution of *w*, $\vec{p}(w,t)$ evolves over time, for any given initial distribution $\vec{p}_0(w)$, given $\vec{p}(w,t) = \vec{p}_0(w) \cdot P^t$, where *P* is the matrix form of $p_{w_i w_j}$.

As an example, we demonstrate $\vec{p}(w,t)$ for uncorrelated Poisson spikes and for fully synchronous Poisson spikes with delays (Fig. S1). In both cases, $r = 20$, $\lambda = 0.01$. For the fully synchronous Poisson spikes, $t_0 = 3$ ms. One can see that starting with a peak around the initial synaptic weight, the distribution of synaptic modification grows monotonically broader with the progress of time. Moreover, the distribution of synaptic modifications for fully synchronous Poisson spikes with a delay (grey) starts deviating from that of the uncorrelated Poisson spikes (black) already after several hundred updates. This result is analogous to the dynamics of expected modifications described in Fig. 4 in the main text.

4. The effects of initial values of the weights on their equilibrium values

In the main text we showed the effect of RTF and synchronicity on the equilibrium weight. Those effects are qualitatively consistent within the parameter space. As already discussed in

the main text, quantitatively they are contingent with firing rate. The initial weight of the synapse also plays a role.

In principle the initial weight should be drawn from an interval of zero to one. However, for the time relationships of pre- and post-synaptic that leads to depressive modifications, an artifact can arise when the initial weight is smaller than 0.5. This is because the multiplicative rule generally pulls the weight towards the value of 0.5. This pulling effect is larger when the weight deviates further from 0.5. The weight at the equilibrium is a result of the balance of the pulling effect and the drifting effect determined by the spike timing. Therefore we discuss the case when the initial weight ranges between 0.5 and one, in order to avoid the artifact that could make the weight larger than the initial value for depression. For the initial value ranging between 0.5 and zero, we artificially set the upper bound of the weight to the initial value. In contrast, as we will discuss later, the additive model does not have such preferences of initial values. Fig. S2 shows that, the overall weight at the equilibrium changes positively with the initial weight for the multiplicative model. In this plot, we let r = 20 Hz, α = 1.

5. Additive model predictions for the homogenous random walk

We define the additive model as follows. As mentioned in the main text, the difference between the additive and multiplicative model is the value of μ. The μ equals zero when the model is additive. As a result, we require that the synaptic modification can only range between zero and one for the additive model. Such normalization is implicit in the multiplicative model whereas in additive model this has to be defined. Similarly as the analyzing the multiplicative models, the expected synaptic modification can be expressed as:

$$E(w_t) = t(p_2 E(F_p) - p_1 \alpha E(F_d)) + w_0 \quad (0<w_t<1) \quad \text{(S1)}$$

The second raw moment of synaptic modification is:

$$E(w_t^2) = 2\lambda(p_2 E(F_p) - p_1 \alpha E(F_d))(E(w_{t-1}) + E(w_t) + \ldots + E(w_0)) + t\lambda^2(p_2 E(F_p^2) + p_1 \alpha^2 E(F_d^2)) + w_0^2 \quad \text{(S2)}$$

The term that multiplies with *t* in (S1) determines the rate of saturation since the synaptic modification always saturates for the additive model. The effect of RFT and synchronicity on the saturation rate resembles that of the equilibrium weight in multiplicative models (Fig. S3).

For additive model the firing rate does not affect the effect of RFT and synchronicity as much as for the multiplicative model. The initial weight does not affect the saturation rate either. However, it does determine the time by which the expected weight reaches the saturation. Fig. S4 shows that the time of saturation as a function of the initial weights, RTF and synchronicity.

Figure Legends

Fig. S1. Distribution of synaptic modifications evolves over time. Grey grids show the distribution of synaptic modification of synchronous pre- and post-synaptic spikes with a relative firing time of 3 ms. Black grids show the distribution for the uncorrelated Poisson spike trains. The initial synaptic weight is 0.5 in both cases.

Fig. S2. Expected synaptic modifications at the equilibrium for different initial weights for the multiplicative model

Fig. S3. Saturation rate of the expected synaptic modifications changes a function of RTF and synchronicity for the additive model.

Fig. S4. The logarithmic value of the time (in milliseconds) it takes for the expected weight to saturate changes as a function of the initial weight, RFT and the synchronicity.

Figure S1

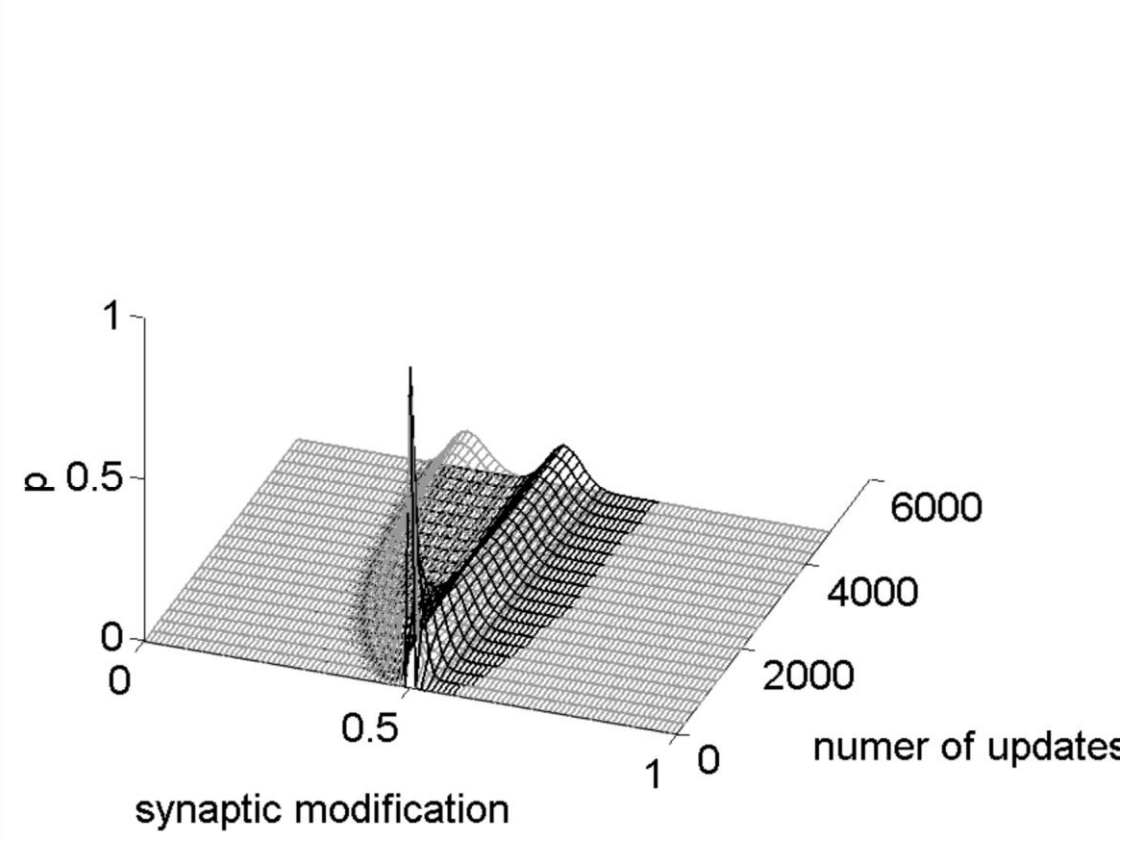
1
p 0.5
0
0
0.5
1
synaptic modification
6000
4000
2000
0
numer of updates

Figure S2

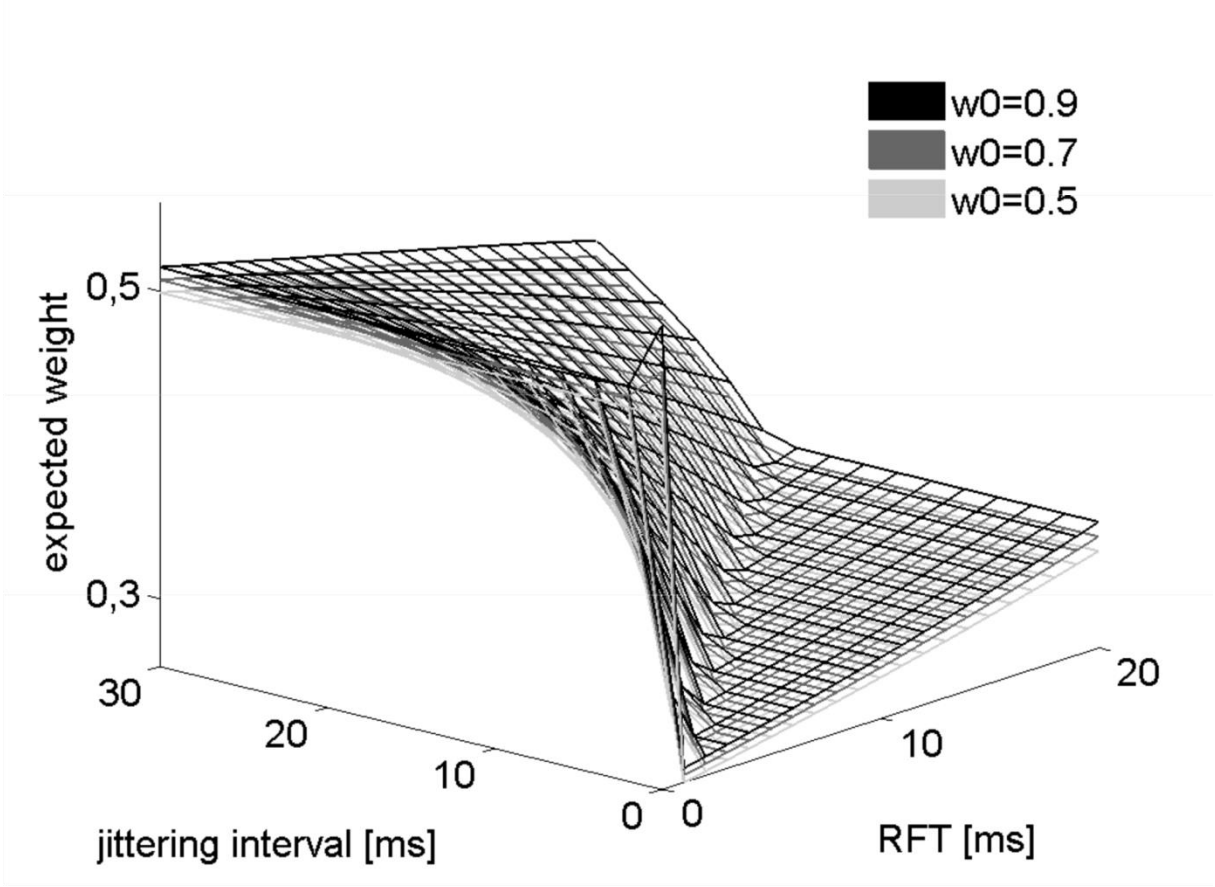
w0=0.9
w0=0.7
w0=0.5
expected weight
0,5
0,3
30
20
10
0
jittering interval [ms]
0
10
20
RFT [ms]

Figure S3

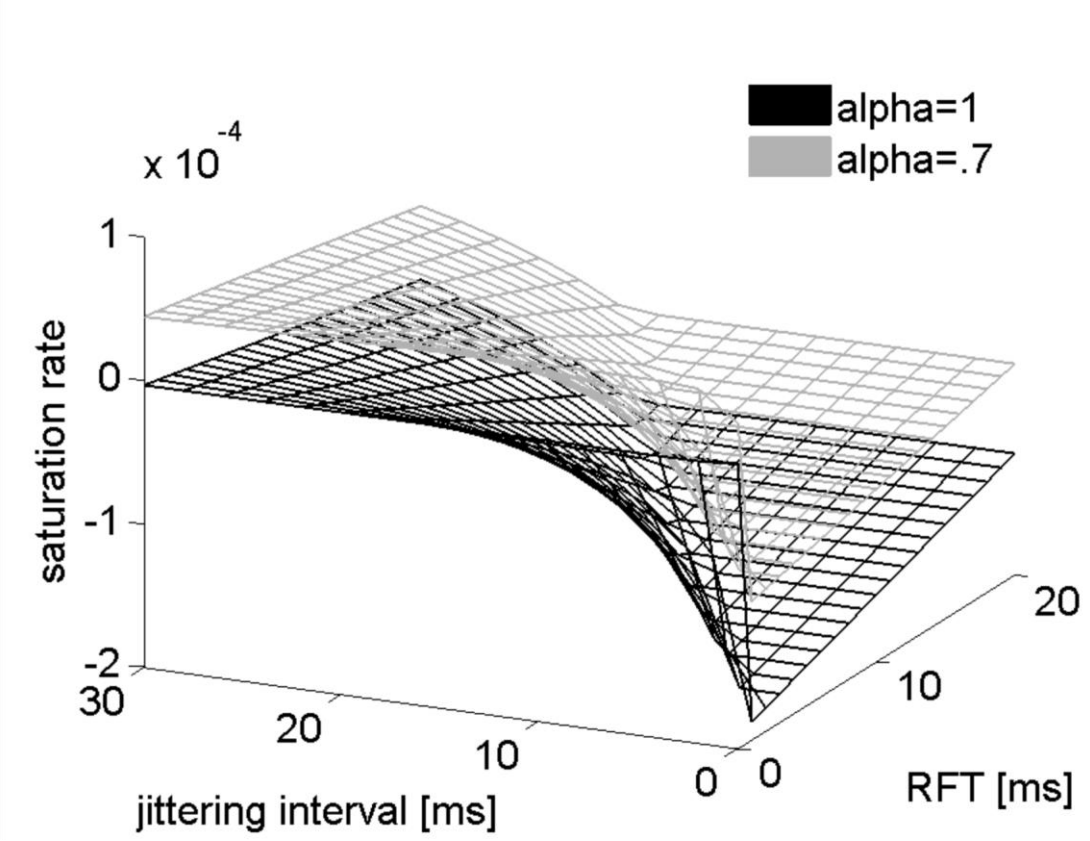
alpha=1
alpha=.7
x 10^-4
1
0
-1
-2
saturation rate
30
20
10
0
jittering interval [ms]
0
10
20
RFT [ms]

Figure S4

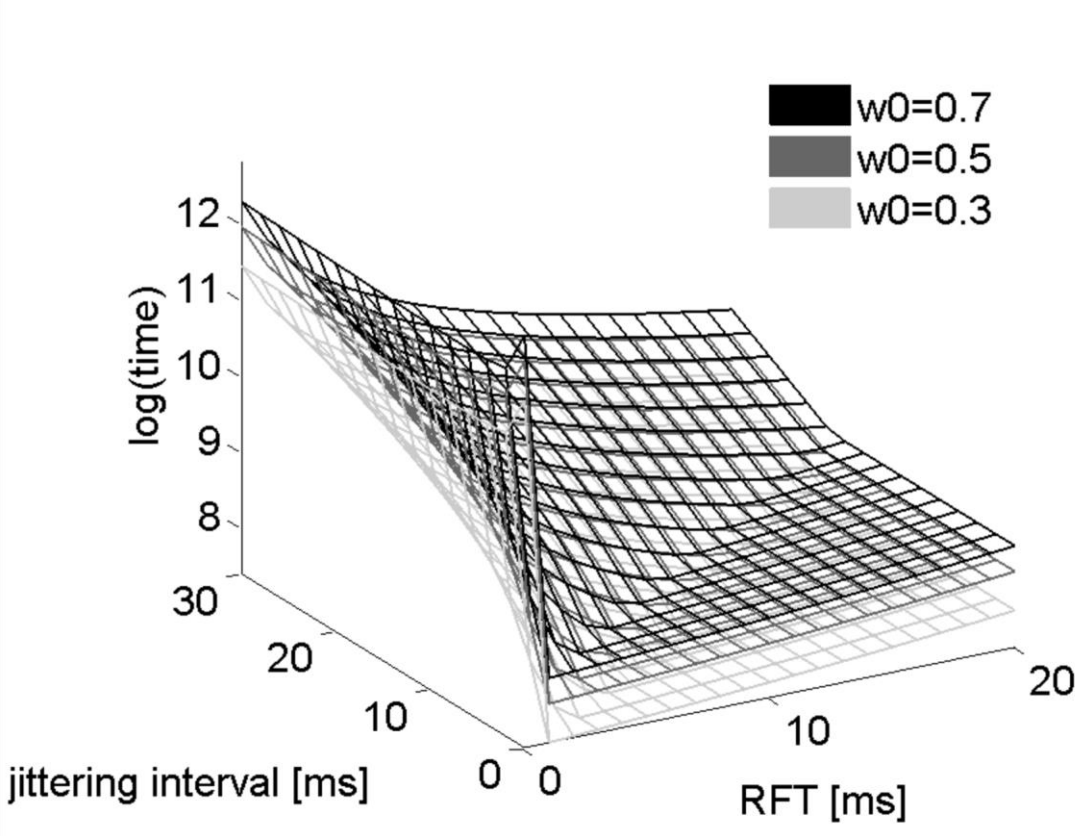
w0=0.7
w0=0.5
w0=0.3
log(time)
12
11
10
9
8
30
20
10
0
jittering interval [ms]
0
10
20
RFT [ms]

Chapter 5 – Discussion and Conclusion

5.1. Fine tunings of neuronal spikes by stimulus properties in beta/gamma frequencies

From a phenomenological point of view, neurons fire stochastically. Thus, in many cases the spiking activities recorded in the visual cortex can be well approximated by Poisson processes with refractory periods. Our results show that when neurons engage in oscillations, their spiking activities become not only non-stationary but also periodic. The periodicity of the firing rate exists at two scales. At the coarser scale, the firing rate is driven by the feed-forward inputs in a mechanical way. For example, simple cells respond with a periodicity corresponding to that of the changes in contrast of the stimulus (Anderson et al., 2000). In our experiment this leads to a periodicity of one to several cycles per second. At a finer scale, as our main results asserted, the firing rate is modulated by the stimuli at the beta/gamma range. This corresponds to the periodicity at 20 or more cycles per second.

Unlike the coarse oscillatory patterning of the firing rate, the finer patterning of the firing rate at the beta/gamma range could happen with or without an overall change of the firing rate at longer time scales. This bares some implication for the hypotheses of neuronal coding. Analogous to the idea of discretization, the hypothesis of coding by the firing rate actually converges to the hypothesis of coding by the spike times, provided that we reduce the scale of interests from several seconds to a millisecond or even less. In this sense, the finding of modulation at the finer scales supports the unity of the hypothesis of coding by firing rate and hypothesis of coding by spike timing.

Vinck et al (2010) reported results closely related to what we found regarding the modulation effect of stimulus property on the neuronal oscillations at the beta/gamma range. In both studies, authors related the modulation at beta/gamma frequencies to how well the stimuli drive the neurons, as indicated by an overall change of firing rate. However, meanwhile

neither study elucidated what this potential relationship might be. Apart from the existing discussions, other possibilities also exist. For example, it has been found that the oscillation frequency of neuronal responses is positively correlated to the velocity of the visual stimuli (Gray et al., 1997). This result was obtained by varying the velocity of the stimuli while keeping the orientation fixed. In contrast, in our experiment and in that of Vinck et al., the velocity of the stimuli was constant and the orientation of stimuli varied. In order to compare the results from different experimental setups, a common reference of either the orientation or velocity should be used. For our experimental setup, one can project the velocity vectors of stimulus to a common orientation of reference. In this case, the velocity component may at least explain some of the modulation effects.

It has been found that the counter-balance of feed-forward excitation and feed-back inhibition gives rise to the oscillation in the neuronal membrane potentials (Vives and McCormicks, 2000; Atallah and Scanziani, 2009). The dynamics of feed-forward and feed-back interactions is most likely a function of the feed-forward inputs. Therefore one can postulate that this function is behind the finding that the oscillation frequency of the V1 neurons varies as a function of the stimulus properties.

As mentioned in Chapter Two, the modulation of the neuronal oscillation leads to the effect of phase precession. Phase precession was originally discovered in the hippocampus of the rats (O'Keefe and Recce, 1993) and occurs when the oscillation of the neuronal membrane dissociates with the oscillation of the neuronal ensemble (Harvey et al, 2009). According to the results of Vinck et al. (2010), spikes modulated by the beta/gamma rhythm shift their preferred firing phase in a stimulus-dependent manner. In addition, this result is more pronounced for the spikes that are less phase-locked to the beta/gamma rhythm.

One can push this condition further. Suppose the oscillatory activity of the neuronal membrane does not lock to the phase of the neuronal ensemble and the frequency of the membrane potential and the ensemble field potential are similar. The averaged higher voltages of membrane can end up at different phases of neuronal ensemble when the frequencies of the oscillating membrane activities differ. Note that the smaller the difference in oscillation frequency is between the membrane activity and the ensemble activity, the more these activities seem to be phase-locked to each other. It is evident that the frequency at the membrane is close to the average frequency of the neurons when these neurons are strongly synchronized. For example, this is true in Kuramoto Model (Kuramoto, 1975). Therefore, the result of Chapter Two and what Vinck et al. (2010) reported all describe essentially the modulation of periodicities in membrane potentials.

We showed that the oscillation frequency of neurons changes slightly over time. This drift of frequency can be fully interpreted as a time-dependent variable despite that the noise does exist in the system as well. Therefore, we postulated that the brain state, which slowly drifts, is responsible for the overall time-dependent drift of oscillation frequencies. Alternatively, one may assume that the noise is solely responsible for the drift of the frequency. Since noise is defined as independent of stimulus or metabolic states, one should expect that the overall increase or decrease of oscillation frequency across all experimental conditions is rare over time. This is because the joint probability of noise terms being all positive or all negative is very small. Therefore, noise is not a good candidate explaining the time dependent drift of oscillation frequency. The brain state on the other hand has periodic nature. Thus, it is more likely that the transition of brain states gives rise to the drift of oscillation frequency.

5.2. Discussion on scaled correlation analysis

In Chapter Three, a method of isolating the effects of slow and fast neuronal activities in cross-correlation was proposed. This method, i.e. scaled correlation, essentially makes the mean amplitude of the neurophysiological signal more homogeneous by segmentation. It could be proven that the expected correlation of segmentation approximates the correlation of signals for which the slow trend is attenuated.

The sample size of individual analyses reduces inevitably when the signal is segmented. For the correlation analysis, this is unfavorable and comes as the main cost of SCA. The reason is that if one tests the null-hypothesis that the correlation coefficient is zero, the critical correlation coefficient grows larger as the sample size reduces. Alternatively, methods developed for meta-analyses can be applied for performing a hypothesis test for the complete signal, rather than the individual segments. Besides, it has been found empirically that the average sample correlation is larger when sample size grows. This result reflects the theoretical prediction of the expected sample correlations for bi-normal variables (Kenney and Keeping, 1939). In line with the empirical results, the expected sample correlation is larger when the sample size is larger. The sample correlation becomes the population correlation when the sample size approaches infinity.

A comparable method was proposal by Bruns (2004), namely envelope correlation (EC). EC is a correlation method applied in frequency domain rather than in time domain, as for the SCA. The basic idea of EC is exactly the same as SCA, which is to calculate the Pearson correlation coefficient for samples of homogenous nature at coarse time-scale and fine-grained structure at short time-scale. The way to accomplish this is also by segmentation of the signal. EC essentially measures coherence in terms of amplitude in frequency domain, as

compared to the coherence measure of phase in frequency domain. To estimate the EC across trials, one has to average the Fisher transformed correlation coefficients and reverse-transform the mean to give an unbiased estimate.

SCA is especially suitable for the analysis of spike time correlation. For the correlation of continuous signals, various de-trending methods have existed. For example, in EEG research, it is common to remove the slow varying linear component of signal before transforming the signal to frequency domain. However, it is difficult to control the effect of slow varying firing rate for the analysis of spike time. This is because one cannot easily regenerate the spike times in controlled manner as the filtering of continuous signals. The SCA method turns to be convenient in this case since no new spikes need to be generated by SCA.

There are some issues which remain to be solved in future studies for SCA. For example, one needs to consider the effect of power law in the estimation of cross-correlations. The power law for the neurophysiological signal is reflected in the fact that spectral power usually can be expressed as a power function of the frequency (Kitzblichler et al., 2009). Further, the Wiener-Khinchin Theorem specifies that the Fourier transform of the autocorrelation is the power spectrum for the signal for which the Fourier transform exists. This means that without any artificial manipulations, the autocorrelation generally exhibits the characteristics that essentially translate to power law distribution for the power spectrum. Controls of power law thus have to be included in the analyses. Another issue for the estimation of SCA is the way to segment the signal. Transfer functions of the implicit high-pass filtering effect of the SCA need to be specified as a function of segment size. It has been shown that the high pass filtering effect of the SCA approximates that of a moving average filter, of which the kernel is as long as the size of segments. However, the exact transfer function of the implicit high-pass filter is still not the same as that of the moving average filter.

The de-trended fluctuation analysis (DFA) and one of its variant de-trended cross-correlation fluctuation analysis (Podobnik and Stanley, 2008) are another approaches SCA can be compared with. In DFA, a transformed signal is separated into segments for which polynomial fits are applied. Oscillatory trend can be removed by fitting the segmented signal with higher-order polynomials and subsequently deleting the fitted polynomials. In this sense, the SCA of the continuous signal is equivalent to the de-trending method employed in DFA without applying the polynomial fitting.

5.3. Some theoretical considerations on synaptic plasticity and spike timing

For the spike timing dependent plasticity (STDP), a simple solution has been proposed by Gütig et al (2003) and further investigated by Morrison et al. (2006). The idea was to describe the expected change of synaptic modification as a function of the correlation of the pre- and post-synaptic spike times. To account for the fact that the synapses are modified much slower than the time scale of the STDP rules, the learning rate is set to be very small. Normalization of the synaptic modification is accomplished by rescaling the raw potentiating or depressive increments by a function of the time-dependent weight of the synapse.

By Gütig et al (2003), the estimated synaptic modification takes a form of summing the grand average of potentiation and depression. This sum is conditioned on an arbitrary weight of synapse. However, generally, the estimation of synaptic modification is a function of time and in most of cases does not equal to the sum of expected potentiation and expected depression averaged over updates. Therefore, one has to come up with a method that catches the essence of the STDP described by the phenomenological models.

In Chaper Four we defined a random walk showing how synaptic modification evolves according to phenomenological models of STDP. The basic idea of this random walk was from Morrison et al. (2008). However, Morrison et al. did not extend the study of STDP random walk and rather advanced the estimation of Gütig et al. (2003). Essentially, such a random walk of synaptic modification is a Markov process. For Poisson pre- and post-synaptic inputs, it has been found that the average modification of the synapse is a function of the cross-correlation of spike time. In particular, synchronicity and the relative firing time play an important role in predicting the magnitude of modification.

Researchers always associate the spike time to the phase of the local field potentials (Montemurro et al., 2008; Cassenaer and Laurent, 2007; Fries et al., 2001). The reason for this is that the local supra- and sub-threshold activities are surveyed by the LFPs. As a result, the LFP appears as if it regulates the spiking activities. The phase of the LFP is a product of local excitation and inhibition (Buzsáki et al., 2012), which are important for when neurons fire (Fries et al., 2007). If one refers the phase of the firing to the expected spike-time in the phase space of the local field potentials, a shift in firing phase will always correspond to a relative spike time and vice versa. This is true whenever the individual firing phase and the period of the LFP are independent.

The time of the spike thus does not necessarily rely on the phase space except for that of the membrane potential. Thus the results of the firing phase dynamics are essentially and inevitably those of the spike timing. For example, as discussed earlier Vinck et al. (2010) found that the phase in beta/gamma LFP, to which the spike times are locked, changes as a function of the stimulus. This result can be interpreted as the expected spike-time changes as a function of stimulus. In doing so, the results of Vinck et al. converge to the study of Havenith et al (2012), in which the relative firing time was defined and extensively analyzed.

Taken together, there is strong evidence that the relative firing time does exist besides the conduction delays, which are not variable. The prediction based on Chapter Four is that if the firing time varies with the stimulus, so does the synaptic modification. This means that if STDP captures the brain activities involved in memory, the time or phase shift of the spikes is what the feed-forward inputs is transformed to for the memory. Unlike the prediction of Lengyel et al. (2005), in which phase response curves was required, our results associate the feed-forward inputs directly to the weight of the synapses.

The result in Chapter Four shows also that in order to achieve substantial modification of synapses, the spike time of the pre- and post-synaptic spikes must be cross-correlated. This finding adds to the already multifaceted role of neuronal synchronization yet another one. The neuronal synchronization has been associated with the identification of the object, attention, preparation of the judgment, learning etc. (Singer 2004; Tallon-Baudry 2009). Our results show it is likely that the role in the STDP is one of the reasons why neuronal synchronization may be responsible for so many neural-cognitive processes.

The questions naturally follow whether the same conclusion holds when the pre- and post-synaptic spikes are non-Poission, and when the phenomenological models differ from what we used in the study. For the first question, interestingly the spikes recorded in vivo are generally Poisson (Gerstein and Mandelbrot, 1964; Maimon and Assad, 2002). In some case, an adjustment may need to be made when the refractory period of the neurons is not small enough to be negligible. Rather than being considerably non-Poisson in the distribution of inter-spike-intervals, the stationarity of the process is more likely to be the factor that manifests itself in the predictions.

As a common form of non-stationarity, the spike times can be oscillatory. As we show in Chapter Two, although the probabilities that decide the branching of the random walk become also oscillatory rather than constant, the evolution of the synaptic modification does not necessarily vary much in its nature compared to the homogenous Poisson. This is true at least when one can approximate the oscillatory spike times by alternating periods of silent and stationary Poisson processes. The process is stochastic with a homogenous transition probability in the non-silent period and constant at silent periods.

The question that remains is mostly related to the choice of the STDP model. Although we did try to make the STDP model as representative as possible, the form of the STDP model is by no means consistent for different types and different dendritic locations of the synapses (Froemke et al., 2005). For example, the suppression model (Froemke and Dan, 2002) has been implemented for estimation of the synaptic modification of the recorded spikes and it differs from the model we theoretically analyzed. Interactive effects between the spikes from either pre- or post-synaptic neurons are considered in the suppression model. The prediction of the suppression model converges to that of the model we theoretically analyzed only when firing rates of the spikes are low such that the interactive effects are negligible.

5.4. General discussions and concluding remarks

The work that has been covered in this thesis can be categorized into two approaches. The first approach is to probe the visual system with varying experimental conditions, as the study described in Chapter Two. The majority of the physiological studies adopts this approach. The goal of such an approach is to make inferences to an unknown system by observing the inputs and outputs. For example, one can vary the speed of the visual stimuli and record the mean firing rate of the neurons from the visual cortex. Apparently, easy to implement and straightforward to analyze, this approach is not always optimal for studying the brain. Suppose that correlations appear between the level of visual contrast and theta power of the scalp EEG. What one can infer from such results to how brain works is limited. The result itself opens a large variety of possibilities which are not always easily testable. For example, is it the contrast that the brain encodes or is it something else, or how does the theta rhythm recorded from scalp come about? In better conditions, when the terms of measurement is less obscure in the meaning, obscurity in inference may still arise. The reason for this difficulty is that the system we study is so complex that a method of regression based on estimates of complex biological processes may not be always useful. Nevertheless, such approach is successful either when the system is less complicated or affords simplification. As mentioned in the introduction, an example is a linear filter model as it can successfully describe the directional preferences of the neurons in visual cortex.

The second approach is more fundamental compared to the first, which is to work on the fundamental concepts that are well defined. For example, compared to what the experimentalists reported in their original studies of STDP, the phenomenological models of STDP are much clearer and completely free of noise. This is a result of drastic simplification. Having much well defined structure, the phenomenological models made further work

possible. This is evidenced by a vast number of theoretical studies in the field of Hebbian learning using the phenomenological models (Song et al., 2000; Kempter et al., 2001; Wörgötter and Porr, 2005; Morrison et al., 2008). In such studies, the biological processes that are the core of the studies are reduced to assumptions or conditions. Again, as the case of the first approach, to make things work, one has to disentangle the complicated system that exhibits certain behavior such as STDP. Only in doing so can one avoid oversimplifying the process that cannot afford any further simplification. However, in reality, the system like brain is so complicated that perhaps any working models can grasp only a small fraction of what the brain is capable of.

Ideally, these two approaches are combined. In this case one cannot only observe the behavior of the system and infer to its organizations, but may also be able to analyze and even build a system that can function analogously. Only in attempting to solve what the brain has to solve can we start to know how the brain works.

References:

Anderson, Jeffrey S., Matteo Carandini, and David Ferster. "Orientation Tuning of Input Conductance, Excitation, and Inhibition in Cat Primary Visual Cortex." *Journal of Neurophysiology* 84, no. 2 (2000): 909-926.

Atallah, Bassam V., and Massimo Scanziani. "Instantaneous Modulation of Gamma Oscillation Frequency by Balancing Excitation with Inhibition." *Neuron* 62, no. 4 (2009): 566-577.

Averbeck, Bruno B., Peter E. Latham, and Alexandre Pouget. "Neural Correlations, Population Coding and Computation." *Nat Rev Neurosci* 7, no. 5 (2006): 358-366.

Bair, Wyeth. "Spike Timing in the Mammalian Visual System." *Current Opinion in Neurobiology* 9, no. 4 (1999): 447-453.

Bair, Wyeth, and Christof Koch. "Temporal Precision of Spike Trains in Extrastriate Cortex of the Behaving Macaque Monkey." *Neural Computation* 8, no. 6 (1996): 1185-1202.

Bruns, Andreas. "Fourier-, Hilbert- and Wavelet-Based Signal Analysis: Are They Really Different Approaches?" *Journal of Neuroscience Methods* 137, no. 2 (2004): 321-332.

Buehlmann, Andres, and Gustavo Deco. "Optimal Information Transfer in the Cortex through Synchronization." *PLoS Comput Biol* 6, no. 9 (2010): e1000934.

Butts, Daniel A., Chong Weng, Jianzhong Jin, Chun- I. Yeh, Nicholas A. Lesica, Jose-Manuel Alonso, and Garrett B. Stanley. "Temporal Precision in the Neural Code and the Timescales of Natural Vision." *Nature* 449, no. 7158 (2007): 92-95.

Buzsáki, György, Costas A. Anastassiou, and Christof Koch. "The Origin of Extracellular Fields and Currents — Eeg, Ecog, Lfp and Spikes." *Nat Rev Neurosci* 13, no. 6 (2012): 407-420.

Caporale, Natalia, and Yang Dan. "Spike Timing–Dependent Plasticity: A Hebbian Learning Rule." *Annual Review of Neuroscience* 31, no. 1 (2008): 25-46.

Carandini, Matteo. "Amplification of Trial-to-Trial Response Variability by Neurons in Visual Cortex." *PLoS Biol* 2, no. 9 (2004): e264.

Carandini, M., F. Mechler, C. S. Leonard, and J. A. Movshon. "Spike Train Encoding by Regular-Spiking Cells of the Visual Cortex." *Journal of Neurophysiology* 76, no. 5 (1996): 3425-3441.

Cassenaer, Stijn, and Gilles Laurent. "Hebbian Stdp in Mushroom Bodies Facilitates the Synchronous Flow of Olfactory Information in Locusts." *Nature* 448, no. 7154 (2007): 709-713.

Castelo-Branco, Miguel, Rainer Goebel, Sergio Neuenschwander, and Wolf Singer. "Neural Synchrony Correlates with Surface Segregation Rules." *Nature* 405, no. 6787 (2000): 685-689.

Citri, Ami, and Robert C. Malenka. "Synaptic Plasticity: Multiple Forms, Functions, and Mechanisms." *Neuropsychopharmacology* 33, no. 1 (2007): 18-41.

Dan, Yang, and Mu-Ming Poo. "Spike Timing-Dependent Plasticity: From Synapse to Perception." *Physiological Reviews* 86, no. 3 (2006): 1033-1048.

Denker, Michael, Sébastien Roux, Henrik Lindén, Markus Diesmann, Alexa Riehle, and Sonja Grün. "The Local Field Potential Reflects Surplus Spike Synchrony." *Cerebral Cortex*, (2011).

Fries, Pascal, Danko Nikolić, and Wolf Singer. "The Gamma Cycle." *Trends in neurosciences* 30, no. 7 (2007): 309-316.

Fries, Pascal, John H. Reynolds, Alan E. Rorie, and Robert Desimone. "Modulation of Oscillatory Neuronal Synchronization by Selective Visual Attention." *Science* 291, no. 5508 (2001): 1560-1563.

Gerstein, George L., and Benoit Mandelbrot. "Random Walk Models for the Spike Activity of a Single Neuron." *Biophysical journal* 4, no. 1 (1964): 41-68.

Gerstner, Wulfram. "Coding Properties of Spiking Neurons: Reverse and Cross-Correlations." *Neural Networks* 14, no. 6–7 (2001): 599-610.

Gilson, Matthieu, Timothée Masquelier, and Etienne Hugues. "Stdp Allows Fast Rate-Modulated Coding with Poisson-Like Spike Trains." *PLoS Comput Biol* 7, no. 10 (2011): e1002231.

Golledge, H. D., S. Panzeri, F. Zheng, G. Pola, J. W. Scannell, D. V. Giannikopoulos, R. J. Mason, M. J. Tovee, and M. P. Young. "Correlations, Feature-Binding and Population Coding in Primary Visual Cortex." *Neuroreport* 14, no. 7 (2003): 1045-50.

Gray, Charles M. "The Temporal Correlation Hypothesis of Visual Feature Integration: Still Alive and Well." *Neuron* 24, no. 1 (1999): 31-47.

Gray, Charles M., Peter Konig, Andreas K. Engel, and Wolf Singer. "Oscillatory Responses in Cat Visual Cortex Exhibit Inter-Columnar Synchronization Which Reflects Global Stimulus Properties." *Nature* 338, no. 6213 (1989): 334-337.

Gray, Charles M., and Gonzalo Viana Di Prisco. "Stimulus-Dependent Neuronal Oscillations and Local Synchronization in Striate Cortex of the Alert Cat." *The Journal of Neuroscience* 17, no. 9 (1997): 3239-3253.

Gros, Claudius. *Complex and Adaptive Dynamical Systems*. Berlin: Springer-Verlag,

2008.

Grün, S, and S. Rotter. *Analysis of Parallel Spike Trains*. New York: Springer, 2010.

Gütig, R., R. Aharonov, S. Rotter, and Haim Sompolinsky. "Learning Input Correlations through Nonlinear Temporally Asymmetric Hebbian Plasticity." *The Journal of Neuroscience* 23, no. 9 (2003): 3697-3714.

Harvey, Christopher D., Forrest Collman, Daniel A. Dombeck, and David W. Tank. "Intracellular Dynamics of Hippocampal Place Cells During Virtual Navigation." *Nature* 461, no. 7266 (2009): 941-946.

Havenith, Martha N., Shan Yu, Julia Biederlack, Nan-Hui Chen, Wolf Singer, and Danko Nikolić. "Synchrony Makes Neurons Fire in Sequence, and Stimulus Properties Determine Who Is Ahead." *The Journal of Neuroscience* 31, no. 23 (2011): 8570-8584.

Hirsch, JA, and CD Gilbert. "Synaptic Physiology of Horizontal Connections in the Cat's Visual Cortex." *The Journal of Neuroscience* 11, no. 6 (1991): 1800-1809.

Jones, J. P., and L. A. Palmer. "The Two-Dimensional Spatial Structure of Simple Receptive Fields in Cat Striate Cortex." *Journal of Neurophysiology* 58, no. 6 (1987): 1187-1211.

Kara, Prakash, Pamela Reinagel, and R. Clay Reid. "Low Response Variability in Simultaneously Recorded Retinal, Thalamic, and Cortical Neurons." *Neuron* 27, no. 3 (2000): 635-646.

Kayser, Christoph, Marcelo A. Montemurro, Nikos K. Logothetis, and Stefano Panzeri. "Spike-Phase Coding Boosts and Stabilizes Information Carried by Spatial and Temporal Spike Patterns." *Neuron* 61, no. 4 (2009): 597-608.

Kempter, Richard, Wulfram Gerstner, and J. Leo van Hemmen. "Intrinsic Stabilization of Output Rates by Spike-Based Hebbian Learning." *Neural Computation* 13, no. 12 (2001): 2709-2741.

Kitzbichler, Manfred G., Marie L. Smith, Søren R. Christensen, and Ed Bullmore. "Broadband Criticality of Human Brain Network Synchronization." *PLoS Comput Biol* 5, no. 3 (2009): e1000314.

Konig, P. "A Method for the Quantification of Synchrony and Oscillatory Properties of Neuronal Activity." *J Neurosci Methods* 54, no. 1 (1994): 31-7.

König, Peter, Andreas K. Engel, Pieter R. Roelfsema, and Wolf Singer. "How Precise Is Neuronal Synchronization?" *Neural Computation* 7, no. 3 (1995): 469-485.

Kreiter, AK, and W Singer. "Stimulus-Dependent Synchronization of Neuronal Responses in the Visual Cortex of the Awake Macaque Monkey." *The Journal of Neuroscience* 16, no. 7 (1996): 2381-2396.

Kumbhani, Romesh D., Mark J. Nolt, and Larry A. Palmer. "Precision, Reliability, and Information-Theoretic Analysis of Visual Thalamocortical Neurons." *Journal of Neurophysiology* 98, no. 5 (2007): 2647-2663.

Kuramoto, Yoshiki. "Self-Entrainment of a Population of Coupled Non-Linear Oscillators." In *International Symposium on Mathematical Problems in Theoretical Physics*, edited by Huzihiro Araki, 39, 420-422: Springer Berlin Heidelberg, 1975.

Lee, Han, Gregory V. Simpson, Nikos K. Logothetis, and Gregor Rainer. "Phase Locking of Single Neuron Activity to Theta Oscillations During Working Memory in Monkey Extrastriate Visual Cortex." *Neuron* 45, no. 1 (2005): 147-156.

Lengyel, Mate, Jeehyun Kwag, Ole Paulsen, and Peter Dayan. "Matching Storage and Recall: Hippocampal Spike Timing-Dependent Plasticity and Phase Response Curves." *Nat Neurosci* 8, no. 12 (2005): 1677-1683.

Louis, Sebastien G R, george L Gerstein, sonja Gruen, and Markus Diesmann. "Surrogate Spike Train Generation through Dithering in Operational Time." *Frontiers in Computational Neuroscience* 4, (2010).

Macke, Jakob H., Philipp Berens, Alexander S. Ecker, Andreas S. Tolias, and Matthias Bethge. "Generating Spike Trains with Specified Correlation Coefficients." *Neural Computation* 21, no. 2 (2008): 397-423.

Mazzoni, Alberto, Nikos K. Logothetis, and Stefano Panzeri. "The Information Content of Local Field Potentials: Experiments and Models." In *Principles of Neural Coding*, edited by Rodrigo Quian Quiroga and Stefano Panzeri: CRC Press, 2012.

McAlonan, Kerry, James Cavanaugh, and Robert H. Wurtz. "Guarding the Gateway to Cortex with Attention in Visual Thalamus." *Nature* 456, no. 7220 (2008): 391-394.

Montemurro, Marcelo A., Malte J. Rasch, Yusuke Murayama, Nikos K. Logothetis, and Stefano Panzeri. "Phase-of-Firing Coding of Natural Visual Stimuli in Primary Visual Cortex." *Current biology : CB* 18, no. 5 (2008): 375-380.

Morrison, Abigail, Markus Diesmann, and Wulfram Gerstner. "Phenomenological Models of Synaptic Plasticity Based on Spike Timing." *Biological Cybernetics* 98, no. 6 (2008): 459-478.

Nikolić, Danko. "Non-Parametric Detection of Temporal Order across Pairwise Measurements of Time Delays." *Journal of Computational Neuroscience* 22, no. 1 (2007): 5-19.

Nirenberg, S., S. M. Carcieri, A. L. Jacobs, and P. E. Latham. "Retinal Ganglion Cells

Act Largely as Independent Encoders." *Nature* 411, no. 6838 (2001): 698-701.

Nirenberg, Sheila, and Peter E. Latham. "Decoding Neuronal Spike Trains: How Important Are Correlations?" *Proceedings of the National Academy of Sciences* 100, no. 12 (2003): 7348-7353.

O'Keefe, J., and J. Dostrovsky. "The Hippocampus as a Spatial Map. Preliminary Evidence from Unit Activity in the Freely-Moving Rat." *Brain Res* 34, no. 1 (1971): 171-5.

O'Keefe, J., and M. L. Recce. "Phase Relationship between Hippocampal Place Units and the Eeg Theta Rhythm." *Hippocampus* 3, no. 3 (1993): 317-30.

Orban, G. *Neuronal Operations in the Visual Cortex*. Berlin: Springer-Verlag, 1984.

Payne, B, and A Peters. *The Cat Primary Visual Cortex*. San Diego: Academic Press, 2002.

Petersen, Rasmus S., Stefano Panzeri, and Mathew E. Diamond. "Population Coding of Stimulus Location in Rat Somatosensory Cortex." *Neuron* 32, no. 3 (2001): 503-514.

Podobnik, Boris, and H. Eugene Stanley. "Detrended Cross-Correlation Analysis: A New Method for Analyzing Two Nonstationary Time Series." *Physical Review Letters* 100, no. 8 (2008): 084102.

Ringach, D. L., C. E. Bredfeldt, R. M. Shapley, and M. J. Hawken. "Suppression of Neural Responses to Nonoptimal Stimuli Correlates with Tuning Selectivity in Macaque V1." *Journal of Neurophysiology* 87, no. 2 (2002): 1018-1027.

Roudi, Yasser, Sheila Nirenberg, and Peter E. Latham. "Pairwise Maximum Entropy Models for Studying Large Biological Systems: When They Can Work and When They Can't." *PLoS Comput Biol* 5, no. 5 (2009): e1000380.

Rubin, Jonathan, Daniel Lee, and H. Sompolinsky. "Equilibrium Properties of Temporally Asymmetric Hebbian Plasticity." *Physical Review Letters* 86, no. 2 (2001): 364.

Sanchez-Vives, Maria V., and David A. McCormick. "Cellular and Network Mechanisms of Rhythmic Recurrent Activity in Neocortex." *Nat Neurosci* 3, no. 10 (2000): 1027-1034.

Schneidman, Elad, Michael J. Berry, Ronen Segev, and William Bialek. "Weak Pairwise Correlations Imply Strongly Correlated Network States in a Neural Population." *Nature* 440, no. 7087 (2006): 1007-1012.

Schroeder, C E, A D Mehta, and S J Givre. "A Spatiotemporal Profile of Visual System Activation Revealed by Current Source Density Analysis in the Awake Macaque." *Cerebral Cortex* 8, no. 7 (1998): 575-592.

Shinomoto, Shigeru, Hideaki Kim, Takeaki Shimokawa, Nanae Matsuno, Shintaro Funahashi, Keisetsu Shima, Ichiro Fujita, Hiroshi Tamura, Taijiro Doi, Kenji Kawano, Naoko Inaba, Kikuro Fukushima, Sergei Kurkin, Kiyoshi Kurata, Masato Taira, Ken-Ichiro Tsutsui, Hidehiko Komatsu, Tadashi Ogawa, Kowa Koida, Jun Tanji, and Keisuke Toyama. "Relating Neuronal Firing Patterns to Functional Differentiation of Cerebral Cortex." *PLoS Comput Biol* 5, no. 7 (2009): e1000433.

Singer, Wolf. "Neuronal Synchrony: A Versatile Code for the Definition of Relations?" *Neuron* 24, no. 1 (1999): 49-65.

Singer, Wolf. "Synchrony, Oscillations, and Relational Codes." In *The Visual Neurosciences* edited by L. M. Chalupa and J. S. Werner. Cambridge, Massachusetts: The MIT Press, 2004.

Sjöström, Per Jesper, Gina G. Turrigiano, and Sacha B. Nelson. "Rate, Timing, and Cooperativity Jointly Determine Cortical Synaptic Plasticity." *Neuron* 32, no. 6 (2001): 1149-1164.

Song, Sen, Kenneth D. Miller, and L. F. Abbott. "Competitive Hebbian Learning through Spike-Timing-Dependent Synaptic Plasticity." *Nat Neurosci* 3, no. 9 (2000): 919-926.

Tallon-Baudry, C. "The Roles of Gamma-Band Oscillatory Synchrony in Human Visual Cognition." *Front Biosci* 14, (2009): 321-32.

Terman, D., and D. Wang. "Global Competition and Local Cooperation in a Network of Neural Oscillators." *Physica D: Nonlinear Phenomena* 81, no. 1-2 (1995): 148-176.

Tiesinga, Paul, Jean-Marc Fellous, and Terrence J. Sejnowski. "Regulation of Spike Timing in Visual Cortical Circuits." *Nat Rev Neurosci* 9, no. 2 (2008): 97-107.

Tiesinga, PaulH E., and J. Vincent Toups. "The Possible Role of Spike Patterns in Cortical Information Processing." *Journal of Computational Neuroscience* 18, no. 3 (2005): 275-286.

Vinck, Martin, Bruss Lima, Thilo Womelsdorf, Robert Oostenveld, Wolf Singer, Sergio Neuenschwander, and Pascal Fries. "Gamma-Phase Shifting in Awake Monkey Visual Cortex." *The Journal of Neuroscience* 30, no. 4 (2010): 1250-1257.

von der Malsburg, Christoph. "The Correlation Theory of Brain Function." 1981.

Walker, Kerry M. M., Bashir Ahmed, and Jan W. H. Schnupp. "Linking Cortical Spike Pattern Codes to Auditory Perception." *J. Cognitive Neuroscience* 20, no. 1 (2008): 135-152.

Wang, DeLiang , and D. Terman. "Locally Excitatory Globally Inhibitory Oscillator Networks." *Neural Networks, IEEE Transactions on* 6, no. 1 (1995): 283-286.

Wang, DeLiang, and David Terman. "Image Segmentation Based on Oscillatory Correlation." *Neural Computation* 9, no. 4 (1997): 805-836.

Waxman, S. *Clinical Neuroanatomy* 26 ed. New York: The McGraw-Hill Companies, 2010.

Williams, Alan, Todd K. Leen, and Patrick D. Roberts. "Random Walks for Spike-Timing-Dependent Plasticity." *Physical Review E* 70, no. 2 (2004): 021916.

Wilson, Hugh R., and Jack D. Cowan. "Excitatory and Inhibitory Interactions in Localized Populations of Model Neurons." *Biophysical journal* 12, no. 1 (1972): 1-24.

Womelsdorf, Thilo, Jan-Mathijs Schoffelen, Robert Oostenveld, Wolf Singer, Robert Desimone, Andreas K. Engel, and Pascal Fries. "Modulation of Neuronal Interactions through Neuronal Synchronization." *Science* 316, no. 5831 (2007): 1609-1612.

Wörgötter, Florentin, and Bernd Porr. "Temporal Sequence Learning, Prediction, and Control: A Review of Different Models and Their Relation to Biological Mechanisms." *Neural Computation* 17, no. 2 (2005): 245-319.

Yu, Shan, Hongdian Yang, Hiroyuki Nakahara, Gustavo S. Santos, Danko Nikolić, and Dietmar Plenz. "Higher-Order Interactions Characterized in Cortical Activity." *The Journal of Neuroscience* 31, no. 48 (2011): 17514-17526.

Curriculum Vitae

Weijia Feng

Date of Birth: Feb 27, 1980
Place of Birth: Yangquan, China

Max Planck Institute for Brain Research
Deutschordenstraße 46
D-60528 Frankfurt/Main

Tel.: +49(0)6996769-277
Mobile Phone: +49 17673014721
Email: weijia.feng@brain.mpg.de

EDUCATION

• PhD Neuroscience, **Technische Universität Darmstadt**, Germany, expected May 2013.

• MS Neuroscience, **Capital Medical University**, Beijing, China. June 2008.

• BS Clinical medicine (5-year program), **Jining Medical College**, China. July 2005.

RESEARCH EXPERIENCE AND CLINICAL INTERNSHIPS

• Doctoral research
Electrophysiology in cat visual cortex, computational neuroscience, Max Planck Institute for Brain Research, Frankfurt am Main, Germany, since Sept 2008.

• Research experience, as a master student
Cognitive and affective neuroscience, EEG/ERP research, Capital Medical University, China Dec 2005-June 2008.

Cellular signal transduction in central neural system, basic training for molecular biology, Sept 2005-Nov 2005.

• Clinical Internships, as a medical student
Shandong Ankang (Psychiatry) hospital, China, July 2005-July 2005.
People's hospital of Rizhao, China, July 2003-July 2004.

PUBLICATIONS

Feng W, Havenith MN, Wang P, Singer W, Nikolić D. (2010) Frequencies of gamma/beta oscillations are stably tuned to stimulus properties. Neuroreport 14, 680-684.

Nikolić D, Mureşan R, **Feng W**, Singer W. (2012) Scaled correlation analysis: A better way to compute a cross-correlogram. Eur J Neurosci 35, 742-62.

Chen A, **Feng W,** Zhao H, Yin Y, Wang P. (2008) EEG default mode network in the human brain: spectral regional field powers. NeuroImage 41, 561-574.

PROFESSIONAL TRAININGS

Summer course in analysis and models in neurophysiology Freiburg, Germany 2009

Winter course in neural data analysis Munich, Germany 2010

Dean of the Faculty of Biology
Technische Universität Darmstadt
Schnittspahnstr. 10
64287 Darmstadt

Declaration of contributions to each thesis chapter (publication)

I have had larger contribution than any other co-author in carrying out the work of the following papers:

Chapter 2: ‘Frequencies of gamma/beta oscillations are stably tuned to stimulus properties’ and Chapter 4: ‘Gamma-band synchrony may be responsible for plasticity in visual cortex’. In these papers I conceptualized the study, executed experiments and data analyses, interpreted the results and co-wrote the paper.

For Chapter 3 entitled ‘Scaled correlation analysis, a better way to compute a cross-correlogram’, my contribution was relatively smaller. While other authors designed the study and conducted the analyses, I provided a key analytical proof for the functioning of the method, which is detailed in Appendix D, and which shows the implicit relationship between scaled correlation method and moving average filtering.

Sincerely

(signature)

Ehrenwörtliche Erklärung:

Ich erkläre hiermit ehrenwörtlich, dass ich die vorliegende Arbeit entsprechend den Regeln guter wissenschaftlicher Praxis selbstständig und ohne unzulässige Hilfe Dritter angefertigt habe.

Sämtliche aus fremden Quellen direkt oder indirekt übernommenen Gedanken sowie sämtliche von Anderen direkt oder indirekt übernommenen Daten, Techniken und Materialien sind als solche kenntlich gemacht. Die Arbeit wurde bisher bei keiner anderen Hochschule zu Prüfungszwecken eingereicht.

Darmstadt, den .....

.....